



Near-junction thermal managements of electronics

Yu-Chao Hua^{a,b}, Yang Shen^a, Zheng-Lai Tang^a, Dao-Sheng Tang^a,
Xin Ran^a, and Bing-Yang Cao^a

^aKey Laboratory of Thermal Science and Power Engineering of Education of Ministry, Department of Engineering Mechanics, Tsinghua University, Beijing, China

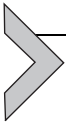
^bLaboratoire de thermique et énergie de Nantes, LTeN, Nantes Université, CNRS, UMR6607, Nantes, France

Contents

1. Background	356
2. Ballistic heat conduction in nanostructures	359
2.1 Diffusive vs. ballistic	359
2.2 Boundary temperature jump (BTJ)	361
2.3 Boundary heat flux slip (BHFS)	368
3. Effective thermal conductivity of nanostructures	374
3.1 Effects of size and geometry	375
3.2 Effect of heating conditions	380
3.3 Interfacial effect	383
3.4 Effects of external fields	392
4. Thermal spreading resistance in ballistic-diffusive regime	398
4.1 Thermal spreading resistance	398
4.2 Influence of phonon ballistic transport	399
4.3 Influence of phonon dispersion	403
4.4 Influence of bias-dependent heat generation	407
4.5 Influence of full-band phonon properties	412
5. Self-heating effect	415
5.1 Self-heating effects in electronic devices	415
5.2 Impact of self-heating effects on electronic devices	416
5.3 Simulating and modeling self-heating effects	417
5.4 Typical devices and self-heating effects	421
5.5 Measurement methods for self-heating effect	424
5.6 Management methods for self-heating effect	425
6. Conclusion	425
Acknowledgments	427
References	427

Abstract

Near-junction thermal management of electronics has received a lot of attention in the past decades but there are still many challenges in this area. This chapter provides a comprehensive review of recent developments in this field. The reduction of scale of devices will result in the crossover of heat transport from the diffusive regime to the ballistic regime. Thus, boundary temperature jumps and boundary heat flux slips emerge. A set of predictive models are developed and verified through comparisons with Monte Carlo method, which will be discussed in detail in this chapter. The thermal conductivity of nanostructures will also deviate from their bulk counterparts. Conductivity is found to depend significantly on multiple factors, including characteristic size and geometry, heating conditions, interfacial effects, stress, and electric fields. Various cases are considering for thermal spreading resistance in electronic devices, with particular emphasis on GaN HEMTs in a ballistic-diffusive regime from multiple perspectives. These cases contain the impacts of phonon ballistic effect, phonon dispersion, bias-dependent heat generation, and first-principle-calculated phonon properties on thermal spreading resistance. Finally, the self-heating effect caused by the scattering between the hot carrier and the lattice is analyzed. Research methods for the self-heating effect are introduced, including some theoretical models and electro-thermal simulations. And the methods for controlling the self-heating effect to improve device performance, reliability, and lifespan are given as well. The present chapter mainly presents some of the most recent progresses for near-junction thermal management of electronics.



1. Background

Wide bandgap (WBG) semiconductors have garnered considerable attention in the development of high-power and high-frequency devices, owing to their exceptional material properties resulting from a large bandgap [1–4]. Among WBG devices, gallium nitride (GaN) high-electron-mobility-transistors (HEMTs) are considered highly promising, capable of sustaining high voltage and current densities due to GaN's wide bandgap and the two-dimensional electron gas formed at the AlGaN–GaN heterojunction [5]. GaN HEMTs have emerged as strong contenders for high-frequency power switching applications and for high-efficiency power amplifiers (PAs) employed in 5G base stations [6].

However, the continuous enhancement in power density and miniaturization of devices has intensified heat dissipation challenges, impeding the realization of their theoretically superior electrical performance [7]. Most commercial GaN HEMTs are limited to 2–4 W/mm output power, in stark contrast to the demonstrated 40 W/mm power output for power amplifiers [8]. Furthermore, inadequate heat dissipation can lead to substantial overheating, raising the junction temperature and compromising the device's

electrical performance, as well as diminishing its operational lifespan [9]. Impacted by a reduction in electron mobility, self-heating induced drain current degradation can amount to nearly 47% [10]. Additionally, research has indicated that a 1 °C temperature increase can result in a 5% decline in device reliability [11], with overheating contributing to over 50% of electronic device failures [12]. As a result, devising effective thermal management strategies to facilitate heat removal from the device and lower the junction temperature is of paramount importance in maintaining optimal performance and reliability [13].

Over the past decades, various external thermal management strategies, including air cooling, heat pipes, microchannel cooling, and jet impingement cooling, have been developed [12,14–17]. These techniques can be viewed as heat sinks installed externally to the package of devices that have already been designed and manufactured. Significant strides have been made in the development of these technologies, e.g., the heat transfer coefficient (HTC) of single-phase cooling methods can range from 1×10^3 to $4 \times 10^4 \text{ W/m}^2 \text{ K}$, and that of double-phase cooling methods can reach approximately $1 \times 10^5 \text{ W/m}^2 \text{ K}$ [18]. As external thermal management technology has matured, the primary challenge in electronic device heat removal has shifted toward addressing internal thermal resistance, specifically heat conduction from the transistor junction into the substrate [19], as shown in Fig. 1. In this context, enhancing the HTC of external cooling strategies will no longer effectively improve heat removal capabilities. Instead, reducing internal thermal resistance through near-junction thermal management and die-level electro-thermal co-design for power and information electronics has become a crucial aspect of thermal management in advancing technology [21–23].

To successfully implement near-junction thermal management in device designs, understanding the heat transport mechanism within the device and accurately predicting near-junction thermal resistance under various design parameters and operating conditions is essential [20,24]. For instance, Fig. 1B–D shows the schematic of the GaN HEMT, which is a multilayer film structure that comprises a substrate layer, GaN buffer layer, and AlGaIn barrier layer [20]. Additional thin layers of GaN or AlN may be inserted at the AlGaIn/GaN interface for electrical purposes, while transition layers, such as AlN, may be grown on substrates to reduce lattice mismatch. The characteristic size of these layers is comparable to the mean free paths (MFP) of phonons, which are the primary heat carriers in semiconductors [25]. Consequently, heat conduction is no longer purely

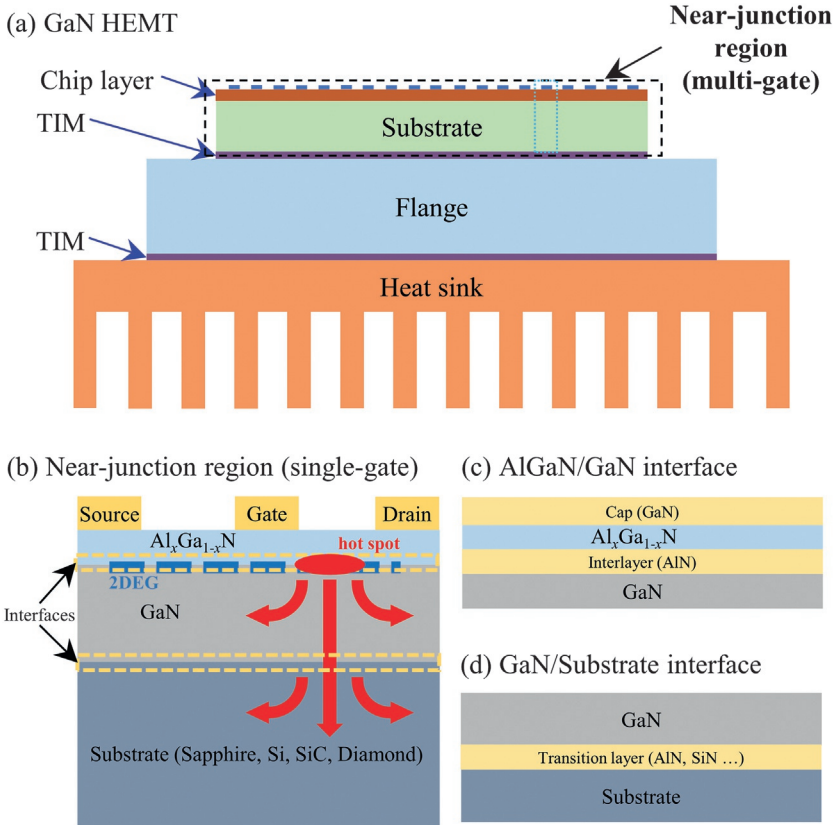


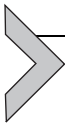
Fig. 1 Schematic illustration of the GaN HEMT device and its near-junction region [20]: (A) The overall architecture of the HEMT; (B) near-junction region of the HEMT (a single finger); (C) in-depth representation of the AlGaN/GaN heterojunction; and (D) GaN/substrate interfacial structure. The blue dashed line signifies the two-dimensional electron gas (2DEG), the red ellipse demarcates the heat source, and the red arrows exemplify the heat flux trajectory.

diffusive, giving rise to ballistic-diffusive heat conduction [26]. In this regime, temperature and heat flux distributions deviate significantly from Fourier's law predictions, with temperature jumps and heat flux slips occurring at boundaries [27]. The boundary and interface scattering of phonons can substantially reduce the thermal conductivity of nanostructures, making the size effect crucial in device designs for improved thermal performance [28,29].

Additionally, the heat generation and phonon thermal transport processes in electronic devices exhibit unique properties, in addition to the classical size effects in general nanostructures that are extensively studied [30].

In GaN HEMTs, heat is primarily generated through electron-phonon interactions in the two-dimensional electron gas (2DEG) region, which spans a width of several hundred nanometers to a few micrometers, depending on the bias voltage and source-to-drain region length [31–33]. The heat source area is considerably smaller than the total device length and thickness, resulting in a significant thermal spreading resistance that dominates the heat transport process in the HEMT [34–36]. Furthermore, since the heat source size is comparable to the MFP of phonons, a non-Fourier thermal spreading process occurs [30]. The interplay between heat generation and conduction, phonon ballistic-diffusive transport, and thermal spreading can substantially impact the near-junction heat transfer process [37–39]. Accurate prediction of device thermal resistance under various conditions necessitates a comprehensive examination of these processes.

This chapter reviews the relevant thermal properties and thermal transport physics in the near-junction thermal management of electronic devices. [Section 2](#) investigates boundary temperature jumps and boundary heat flow slips in ballistic-diffusive heat conduction in nanostructures, employing phonon Monte Carlo (MC) simulation and the phonon Boltzmann transport equation (BTE). The influence of interface phonon property mismatch is explored, and associated prediction models are derived. [Section 3](#) presents theoretical studies on the effective thermal conductivity of typical nanostructures, examining the effects of multiple constraints, heating methods, and boundary roughness on effective thermal conductivity and deriving corresponding prediction models. [Section 4](#) investigates the thermal spreading resistance in the ballistic-diffusive regime for GaN HEMTs, discussing the influence of phonon ballistic effects, phonon dispersion, bias-dependent heat generation, and full-band phonon properties predicted by first principles. [Section 5](#) discusses the self-heating effect of electronic devices, i.e., the temperature-induced electrical performance degradation. This chapter aims to provide a review of the near-junction thermal management of electronics, with a particular focus on elucidating the underlying phonon thermal transport mechanisms and their implications on device thermal performance.



2. Ballistic heat conduction in nanostructures

2.1 Diffusive vs. ballistic

Thermal transport in dielectric and semiconductor materials is dominated by phonons, which are converted from the lattice vibrations through secondary quantization [40].

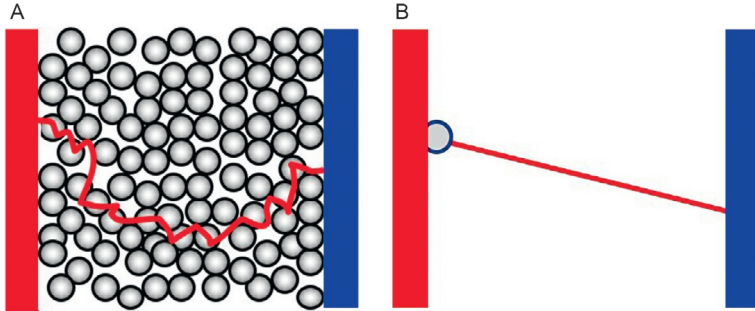


Fig. 2 (A) Diffusive transport and (B) ballistic transport.

Generally, Fourier's law is employed to characterize the heat conduction at macroscale, which is given by,

$$q = -\kappa_0 \nabla T, \quad (1)$$

where q is heat flux, T is temperature, and κ_0 is intrinsic thermal conductivity that is a physical property independent on the size or geometry of structures [41]. It should be noted that the underlying mechanism of Fourier's law is the diffusive transport of heat carriers, where the phonons from heat source will undergo tremendous scattering events during the traveling process, as shown in Fig. 2A. However, this could become invalid as the mean free paths (MFPs) of phonons are comparable to the characteristic lengths of the system, like in the nanostructures. In this case, as shown in Fig. 2B, the phonons will travel directly from one boundary to another without undergoing internal scatterings, which is known as ballistic transport [28,42,43].

Ballistic effect can lead to three major non-Fourier heat conduction phenomena:

- (a) **Boundary temperature jump (BTJ)**: due to the ballistic effect, the assumption of local thermal equilibrium no longer applies, and the phonons and heat sink cannot reach temperature equilibrium, leading to temperature jump at the boundary [28,44,45].
- (b) **Boundary heat flux slip (BHFS)**: the boundary/interface density will greatly increase in nanostructures, which makes the phonon-boundary scattering much more significant, and the phonon scattering at boundaries can alter the traveling directions of phonons and thus reduce the heat flux near the boundaries or interfaces [27,46].
- (c) **Size effect of effective thermal conductivity**: for a nanostructure, its effective thermal conductivity can also be calculated in terms of Fourier's law; however, due to the violation of diffusive transport,

the effective thermal conductivity will have strong size effect, that is, it becomes on dependent on the size, geometry, and even heating conditions of the nanostructures [29,47], which is much different with the bulk case.

The ballistic heat conduction in nanostructures can be described though the Boltzmann transport equation (BTE) [25]. It is based on particle dynamics and neglect the wave effect of heat carriers, and capable of simulating the systems from nanometers to hundred microns, and thus serves as a feasible solution to characterize the non-Fourier thermal transport in practical electronics [30,38,48–50]. BTE describes the evolution of heat carrier distribution $f(x, \omega, t)$, which refers to the fraction of heat carriers of position x and angular frequency ω at time t . The general form of phonon BTE is given by [25],

$$\frac{\partial f}{\partial t} + \mathbf{v} \cdot \nabla f = \left(\frac{\partial f}{\partial t} \right)_s + \dot{s}_f \quad (2)$$

where \mathbf{v} denotes the group velocity of phonons, $\left(\frac{\partial f}{\partial t} \right)_s$ is the scattering term, and \dot{s}_f is the source term. In general, the scattering term can be simplified using the relaxation time approximation [41],

$$\left(\frac{\partial f}{\partial t} \right)_s = \frac{f_0 - f}{\tau}, \quad (3)$$

in which f_0 is the equilibrium distribution, τ is the relaxation time. Moreover, the Knudsen number (Kn), defined as the ratio between the MFP and the characteristic length, is usually used to label the intensity of ballistic effect. Higher Kn value indicates the stronger ballistic effect in the system.

Particularly in this section, we will focus on the Boundary temperature jump and Boundary heat flux slip of ballistic heat conduction based on the BTE; the detailed discussions on the effective thermal conductivity will be given in Section 3.

2.2 Boundary temperature jump (BTJ)

Fig. 3 illustrates the schematic for three different temperature distributions of 1D cross-plane heat conduction in varied regimes. In the case of purely-diffusive regime ($Kn = 0$, and the Kn number here is the ratio between MFP and x -directional thickness), where Fourier's law is valid, the structure holds the same temperature as the contacted heat sink at the boundary. By contrast, in the limiting case of fully-ballistic transport ($Kn \rightarrow \infty$), no temperature gradient can be established inside the nanostructure due to the lack

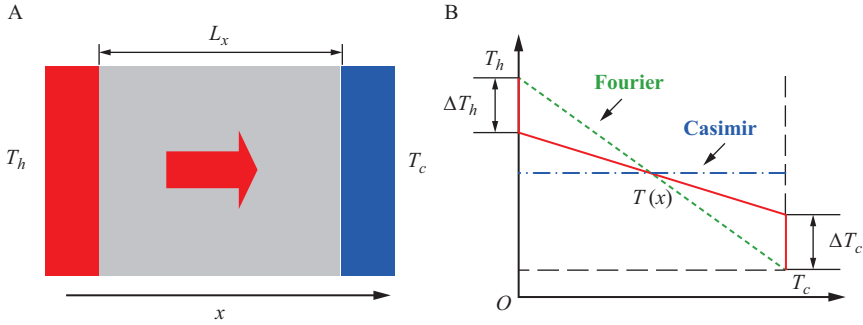


Fig. 3 (A) Cross-plane heat conduction in nanofilm and (B) schematic of boundary temperature jump.

of internal scattering events, and temperature jumps will occur at the boundaries, which is called Casimir limit [51]. In practice, the heat conduction in nanostructures is frequently between these two limiting cases, $0 \leq Kn < \infty$, where both internal temperature gradient and BTJ exist. Early in 1960s, Rieder et al. [52] derived the temperature distribution in Casimir limit for a 1D harmonic atomic chain. Alvarez and Jou [53] introduced a boundary thermal resistance (BTR) to describe the BTJ. Maassen and Lundstrom [42] obtained a BTJ model using the McKelvey-Shockley flow method, and provided a preliminary analysis of the effect of phonon dispersions. In addition of Kn number that reflects the both the scale of nanostructures and the phonon transport properties, the boundary conditions can have significant influence on the BTJ [27]. In the view of phonon transport, we generally have two types of boundary conditions [27]: (a) phononic black-body boundary, which is an ideal case and analogue to the photonic black-body boundary, where all the phonons reaching the boundary in contact with the heat sink will be absorbed; (b) reflective boundary condition considering interfacial effect resulted from the phonon property mismatch at boundary, where some portion of phonons will be reflected at the boundary, and the corresponding reflectance can be determined by the interfacial effect. Hua and Cao [27] discussed the BTJs in these two boundary conditions on the basis of phonon BTE.

The features of BTJs at these two boundary conditions will be discussed in the following subsections based on the phonon BTE.

2.2.1 Black-body boundary

In the case of 1D cross-plane ballistic heat conduction with black-body boundaries, the corresponding governing equation and boundary conditions are given by,

$$\mu\nu \frac{\partial f}{\partial x} = \frac{f_0 - f}{\tau}, \quad (4)$$

$$\begin{aligned} f^+(\mu \geq 0, x = 0) &= f_0(T_h), \\ f^-(\mu \leq 0, x = L_x) &= f_0(T_c), \end{aligned} \quad (5)$$

in which $\mu = \cos(\theta)$ with θ the angle between the phonon traveling direction and the x -axis, L_x is the x -directional length of structure, T_h is the temperature of hot heat sink, and T_c is the temperature of cold heat sink. Based on the heat flux continuity condition at the boundaries and the diffusion approximation for solving the BTE, Eq. (4), the expressions of BTJs can be derived [27],

$$\begin{aligned} T_h - T|_0 &= -\frac{2l_{\text{MFP}}}{3} \frac{\partial T}{\partial x} \Big|_0 = \frac{2}{C_V \nu} q_x \Big|_0, \\ T|_{L_x} - T_c &= -\frac{2l_{\text{MFP}}}{3} \frac{\partial T}{\partial x} \Big|_{L_x} = \frac{2}{C_V \nu} q_x \Big|_{L_x}, \end{aligned} \quad (6)$$

where $l_{\text{MFP}} = \nu\tau$ is the MFP, C_v is the heat capacity, and q_x is the x -directional heat flux. Referring to Eq. (6), the BTJs increase with the increasing heat flux across the boundaries. Although the derivation process above is for 1D system, based on the methodology, the BTJ model for curved boundaries and 3D cases can also be obtained.

Combining the boundary conditions of BTJ above with the energy conservation equation and the diffusion approximation of BTE [27], the temperature distribution can be obtained,

$$T(x) = \frac{\left[T_h + (T_c - T_h) \frac{x}{L_x} \right] + \frac{2}{3} Kn (T_c + T_h)}{1 + \frac{4}{3} Kn}, \quad (7)$$

with $Kn = l_{\text{MFP}}/L_x$. As $Kn \rightarrow 0$, the expression above is reduced to the fully-diffusive solution,

$$T(x) = T_h + (T_c - T_h) \frac{x}{L_x}. \quad (8)$$

On the contrary, with $Kn \rightarrow \infty$, we have the solution at the Casimir limit,

$$T(x) = \frac{T_c + T_h}{2}. \quad (9)$$

Fig. 4A shows the temperature distributions predicted by the model and the phonon Monte Carlo (MC) simulation [54] that directly solves the phonon BTE, respectively. When the ballistic effect can be ignored, the result of Fourier's law is basically consistent with that from the MC simulation.

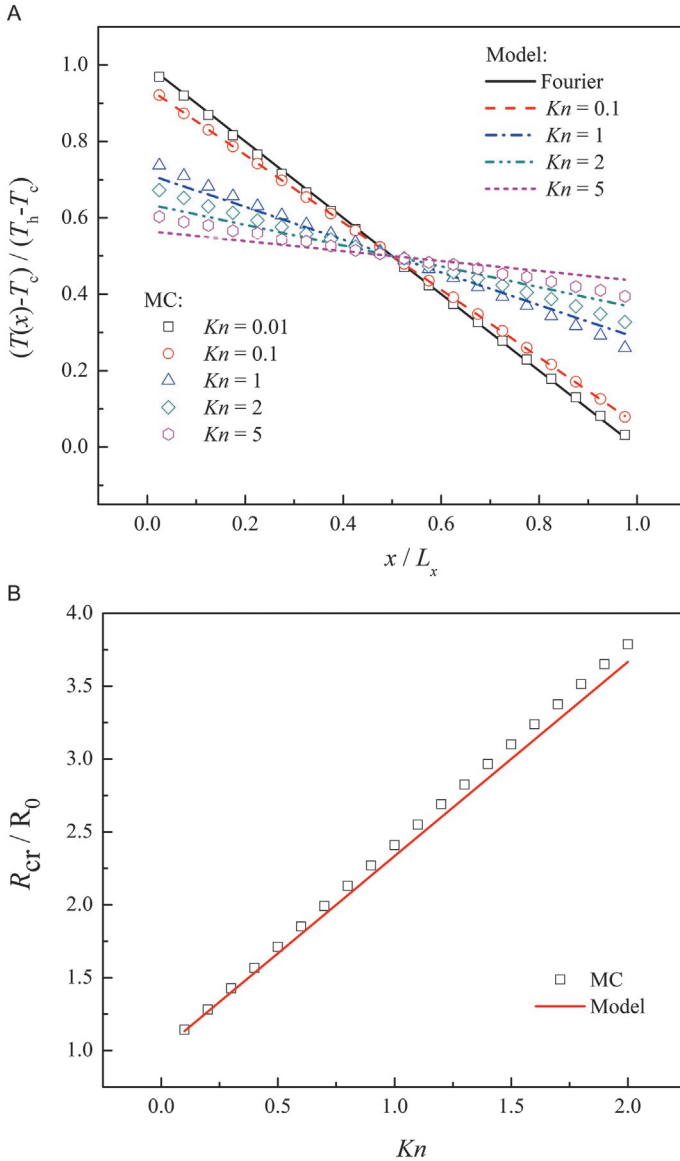


Fig. 4 (A) Temperature distributions within nanofilm of phononic black-body boundaries and (B) cross-plane thermal resistance of nanofilm of phononic black-body boundaries.

As the Kn number increases, the BTJs become larger and larger, causing the temperature distribution to deviate from the prediction of Fourier's law. The temperature distribution model, Eq. (7), can well predict the results of the phonon MC simulation.

Furthermore, the total thermal resistance of this cross-plane heat conduction nanofilm can be derived based on the model above [27], which is given by,

$$\frac{R_{\text{cr}}}{R_0} = 1 + \frac{4}{3}Kn = 1 + \frac{R_{\text{ba}}}{R_0}, \quad (10)$$

where $R_0 = L_x/\kappa_0$ is the intrinsic thermal resistance, and R_{ba} can be called the ballistic thermal resistance,

$$R_{\text{ba}} = \frac{4}{3}Kn \frac{L_x}{\kappa_0} = \frac{4}{3}KnR_0, \quad (11)$$

which will be enhanced with the increasing Kn number.

Fig. 4B shows the cross-plane thermal resistance ratio as a function of the Kn number, obtained from Eq. (10) and phonon MC simulations. The ratio between the total thermal resistance and the intrinsic one linearly increases with the increasing Kn number, which underscores of ballistic effect at nanoscale. It should be emphasized that ballistic thermal resistance is not a phenomenon limited to the boundary, but is related to the characteristic length of the entire system. As the characteristic length increases (Kn number decreases), the ballistic effect gradually weakens, with the ballistic thermal resistance decreasing. Eq. (10) can predict the cross-plane thermal resistance of nanofilm with phononic blackbody boundaries very well, with a maximum deviation from the MC prediction of less than 5%.

2.2.2 Reflective boundary condition with interfacial effect

In practical applications, the boundary in contact with the heat sink generally has phonon properties mismatch (i.e., the heat sink and the nanostructure are different materials). In this case, the reflective boundary condition should be adopted [27] to consider the transmission and reflection of phonons at the boundary,

$$\begin{aligned} f^+(\mu \geq 0, x = 0) &= t_{\text{hf}}f_0(T_h) - r_{\text{fh}}f^-(\mu \leq 0, x = 0), \\ f^-(\mu \leq 0, x = L_x) &= t_{\text{hf}}f_0(T_c) - r_{\text{fh}}f^+(\mu \geq 0, x = L_x). \end{aligned} \quad (12)$$

in which t_{hf} is the transmittance from heat sink to nanofilm, and r_{fh} is the reflectance in the nanofilm. At the room or higher temperature, the phonon transmittance and reflectance can be estimated using the diffusion mismatch model (DMM) [55],

$$\begin{aligned}
 t_{\text{hf}} &= \frac{C_V \nu}{C_{Vh} \nu_h + C_V \nu}, \\
 r_{\text{fh}} &= \frac{C_V \nu}{C_{Vh} \nu_h + C_V \nu}.
 \end{aligned}
 \tag{13}$$

Following the identical methodology for the phononic black-body boundary case, the BTJs in this case is derived as [27],

$$\begin{aligned}
 T_h - T|_0 &= -\frac{2}{3} l_{\text{MFP}} \left(\frac{1 + r_{\text{fh}}}{1 - r_{\text{fh}}} \right) \frac{\partial T}{\partial x} \Big|_0, \\
 T|_{L_x} - T_c &= -\frac{2}{3} l_{\text{MFP}} \left(\frac{1 + r_{\text{fh}}}{1 - r_{\text{fh}}} \right) \frac{\partial T}{\partial x} \Big|_{L_x}.
 \end{aligned}
 \tag{14}$$

Then, the temperature distribution can be obtained as follows,

$$T(x) = \frac{\left[T_h + (T_c - T_h) \frac{x}{L_x} \right] + \frac{2}{3} \left(\frac{1 + r_{\text{fh}}}{1 - r_{\text{fh}}} \right) Kn (T_c + T_h)}{1 + \frac{4}{3} Kn \left(\frac{1 + r_{\text{fh}}}{1 - r_{\text{fh}}} \right)}.
 \tag{15}$$

Similarly, as $Kn \rightarrow 0$, Eq. (15) will be reduced to the Fourier's law-based solution, i.e., Eq. (8), and as $Kn \rightarrow \infty$, Eq. (15) becomes the solution of Casimir limit.

Fig. 5A presents the temperature distributions inside the nanofilms with reflective boundary conditions. Here, it is assumed that the material of the heat sink is germanium (Ge) and the film material is silicon (Si). According to Chen's article [55], the phonon properties of Ge and Si are as follows: $C_{V_Si} = 0.93 \times 10^6 \text{ J/m}^3 \text{ K}$, $\rho_{Si} = 2330 \text{ kg/m}^3$, $\nu_{Si} = 1804 \text{ m/s}$, $\text{MFP}_{Si} = 260.4 \text{ nm}$, $C_{V_Ge} = 0.87 \times 10^6 \text{ J/m}^3 \text{ K}$, $\rho_{Ge} = 5500 \text{ kg/m}^3$, $\nu_{Ge} = 1042 \text{ m/s}$, and $\text{MFP}_{Ge} = 198.6 \text{ nm}$. Thus, the phonon transmittance and reflectance are calculated using the DMM. The ballistic effect and the phonon property mismatch are coupled and cause the BTJs.

Furthermore, the total thermal resistance in this case is given by [27],

$$R_{\text{cr_interface}} = \frac{L_x}{\kappa_0} \left[1 + \frac{4}{3} Kn \left(\frac{1 + r_{\text{fh}}}{1 - r_{\text{fh}}} \right) \right] = R_0 + R_{\text{coup}},
 \tag{16}$$

in which R_{coup} is the thermal resistance resulted from the coupling of ballistic effect and interfacial effect. Fig. 5B shows the total thermal resistance calculated by the model Eq. (16) and the MC simulation, respectively. As indicated by both the model and simulation, due to the effect of interface phonon property mismatch, the thermal resistance significantly increases compared to the case of phononic blackbody boundary.

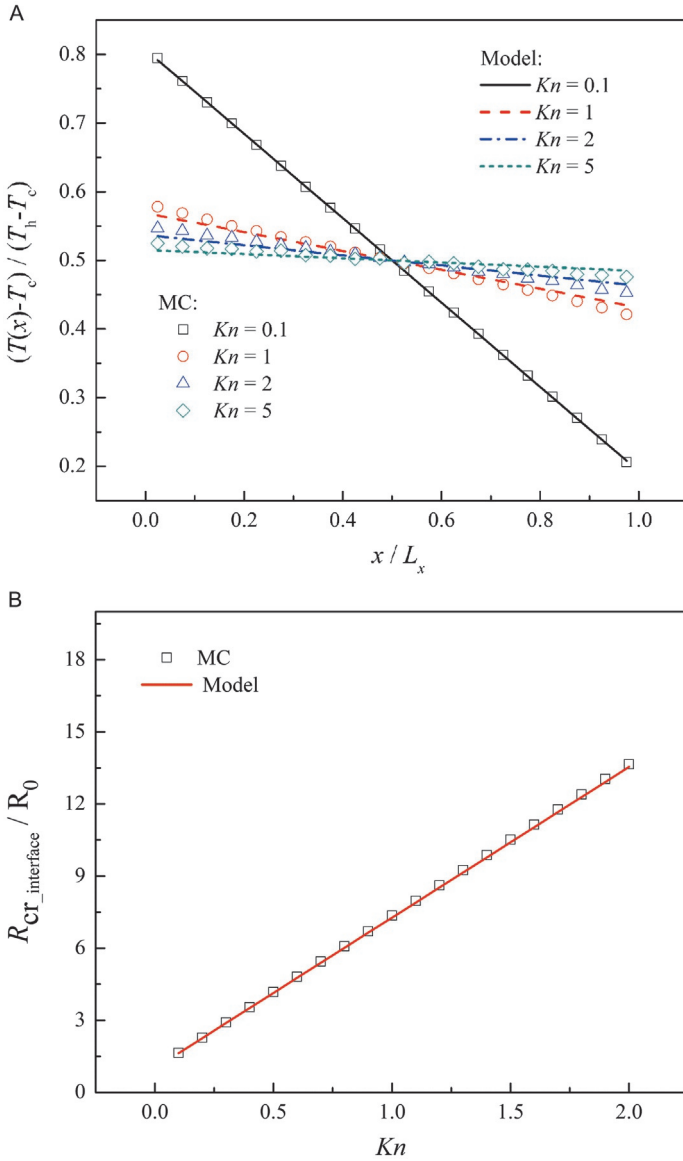


Fig. 5 (A) Temperature distributions within nanofilm of reflective boundaries and (B) cross-plane thermal resistance of nanofilm of reflective boundaries.

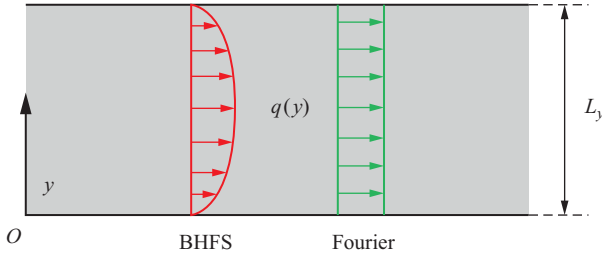


Fig. 6 Schematic of the heat flux distributions for in-plane heat conduction in nanofilm.

2.3 Boundary heat flux slip (BHFS)

Phonon scattering at the rough boundaries is the leading factor that causes the BHFS [27,46]. Fig. 6 shows the schematic that compares the heat flux distributions in different regimes for the in-plane heat conduction within a suspended film. In the case of diffusive heat conduction, the heat flux is uniform along the y direction. By contrast, with the y -directional thickness decreasing, i.e., the Kn number increasing, the phonon-boundary scattering will reduce the heat flux near the boundaries. For such suspended case, Ziman [40] derived a prediction model for the heat flux distributions based on BTE. Additionally, the heat flux distributions for suspended nanostructures were described using the phenomenological models based on the phonon hydrodynamics by analogy with the velocity slip condition in fluid mechanics [56]. Nevertheless, it should be noted that most of the nanostructures in practice are not suspended, especially in the case of electronic devices where the basic structure is generally nanofilm on substrate. In this sense, the interfacial effect can significantly alter the heat flux distributions [27,57,58]. Hua and Cao [27] studied this effect in the nanofilm on a substrate based on the BTE.

This subsection will discuss the features of BHFS in the suspended and supported nanofilms respectively on the basis of phonon BTE.

2.3.1 Suspended case

For a suspended nanofilm illustrated in Fig. 6, the temperature difference is imposed in the x -direction, and the BTE is simplified to consider only the effect of boundary scattering in the y -direction [27],

$$v_y \tau \frac{\partial \Delta f}{\partial y} + \Delta f = -v_x \tau \frac{\partial f_0}{\partial T} \frac{dT}{dx} \quad (17)$$

with $\Delta f = f - f_0$ and the boundary conditions as,

$$\begin{aligned}\Delta f(0, v_y > 0) &= P_r \Delta f(0, v_y < 0), \\ \Delta f(L_y, v_y < 0) &= P_r \Delta f(L_y, v_y > 0).\end{aligned}\quad (18)$$

in which P_r is the specular reflection coefficient of phonons. We can have the heat flux distribution [27],

$$\frac{q_x(y)}{q_0} = 1 - \frac{3}{4} \int_0^1 \frac{1 - P_r}{1 - P_r \exp\left(-\frac{1}{\mu Kn}\right)} \left[\begin{array}{c} \exp\left(-\frac{y/L_y}{\mu Kn}\right) + \\ \exp\left(-\frac{1 - y/L_y}{\mu Kn}\right) \end{array} \right] (1 - \mu^2) d\mu, \quad (19)$$

where $q_0 = -\kappa_0 dT/dx$ is the heat flux calculated using Fourier's law with the intrinsic thermal conductivity, and the Kn number here is defined as $Kn = l_{MFP}/L_y$.

Fig. 7A gives the heat flux distributions in the suspended nanofilms. The model above can well predict the results obtained by the MC simulations. Due to the diffusive phonon boundary scattering, the heat flux decreases near the boundaries. When phonons undergo fully specular reflection at the boundary with $P_r = 1$, the BHFS disappears. In addition, as the Kn number increases, the effect of boundary scattering becomes more profound, and the heat flux near the boundaries will further decrease.

Furthermore, the in-plane thermal resistance can be given by,

$$\frac{R_{in}}{R_0} = \left[1 - \frac{3Kn(1 - P_r)}{2} \int_0^1 \frac{1 - \exp\left(-\frac{1}{\mu Kn}\right)}{1 - P \exp\left(-\frac{1}{\mu Kn}\right)} (1 - \mu^2) \mu d\mu \right]^{-1} \quad (20)$$

in which $R_0 = L_x/\kappa_0 L_y$ is the intrinsic thermal resistance in this case. As shown in Fig. 7B, Eq. (20) agrees well with the results obtained from phonon MC simulations. Increasing the Kn number or decreasing the specular reflection coefficient both result in an increase in the in-plane thermal resistance of the nanofilm. As $P_r = 1$, the completely-specular reflection on the boundaries will not cause the heat flux slips, so the in-plane thermal resistance of the nanofilm will not increase as the thickness decreases.

2.3.2 Nanofilm on substrate

For the electronic devices, the nanofilms are always placed on a substrate, as shown in Fig. 8, and the interface between the nanofilm and the

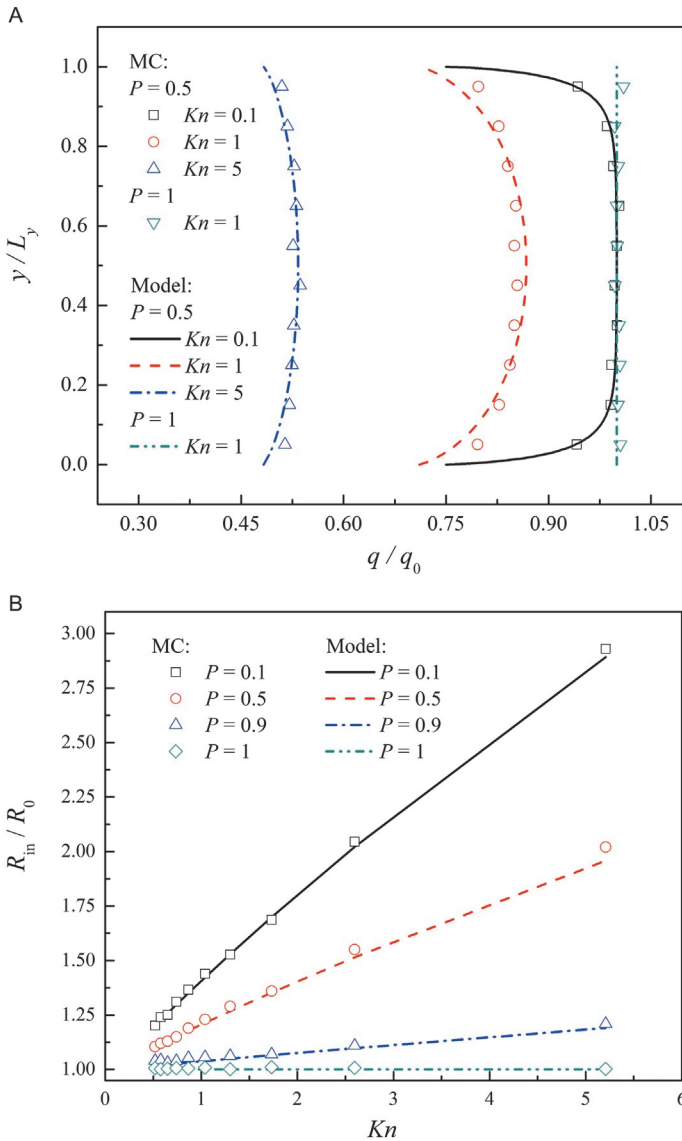


Fig. 7 (A) Heat flux distributions within suspended nanofilm and (B) in-plane thermal resistance of suspended nanofilm.

substrate will also have a significant impact on the heat flux distribution within the nanofilm. The phonons can scatter at the interface; they can also penetrate the interface and enter the substrate, while the phonons in the substrate can enter the nanofilm. At this point, there are two main

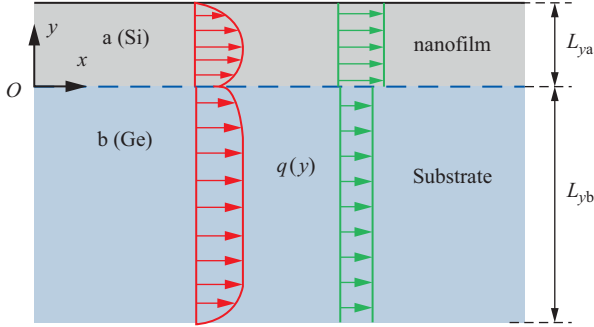


Fig. 8 Schematic of the heat flux distribution within the nanofilm on a substrate.

factors affecting the heat flux distributions inside the nanofilm: the phonon scattering at the interface and the phonon property mismatch between the nanofilm and the substrate [27].

Here, the corresponding BTE and boundary conditions become [27],

$$\nu_{ya}\tau_a \frac{\partial \Delta f_a}{\partial y} + \Delta f_a = -\nu_{xa}\tau_a \frac{\partial f_{0a}}{\partial T} \frac{dT}{dx}, \quad (21a)$$

$$\nu_{yb}\tau_b \frac{\partial \Delta f_b}{\partial y} + \Delta f_b = -\nu_{xb}\tau_b \frac{\partial f_{0b}}{\partial T} \frac{dT}{dx}, \quad (21b)$$

with

$$\begin{aligned} \Delta f_a(L_{ya}, \nu_{ya} < 0) &= P_a \Delta f_a(L_{ya}, \nu_{ya} > 0), \\ \Delta f_a(0, \nu_{ya} > 0) &= P_{ab} [r_{aa} \Delta f_a(0, \nu_{ya} < 0) + t_{ba} \Delta f_b(0, \nu_{yb} > 0)], \\ \Delta f_b(0, \nu_{yb} < 0) &= P_{ab} [r_{bb} \Delta f_b(0, \nu_{yb} > 0) + t_{ab} \Delta f_a(0, \nu_{ya} < 0)], \\ \Delta f_b(-L_{yb}, \nu_{yb} > 0) &= 0, \end{aligned} \quad (22)$$

in which the subscript “a” marks quantities related to phonons inside the thin film, while the subscript “b” for those inside the substrate, r_{aa} and r_{bb} are the interfacial phonon reflectance for the film and substrate, respectively, t_{ab} and t_{ba} are the interfacial phonon transmittance for the film and substrate, respectively, P_a and P_{ab} are the specular reflection (transmission) coefficients.

Generally, the substrate is much thicker than the nanofilm, so the interface/boundary effect does not significantly affect the thermal transport in the substrate. Therefore, it is necessary to focus on the heat flux distributions inside the nanofilm. To simplify the model, it can be assumed that the

lower boundary of the substrate is completely diffuse. Then, the heat flux distribution within the nanofilm with considering the substrate is expressed as ($0 \leq \gamma < L_{\gamma a}$) [27],

$$\frac{q_a(\gamma)}{q_{0a}} = 1 - \frac{3}{4} \int_0^1 \left(G_a^+ \exp\left(-\frac{\gamma/L_{\gamma a}}{\mu Kn_a}\right) + G_a^- \exp\left(\frac{\gamma/L_{\gamma a}}{\mu Kn_a}\right) \right) (1 - \mu^2) d\mu, \tag{23}$$

with

$$G_a^+ = \frac{1 + P_{ab} \left[\left(\exp\left(-\frac{L_{\gamma a}}{l_{MFPa}\mu}\right) (1 - P_a) - 1 \right) r_{aa} + \left(\exp\left(-\frac{L_{\gamma b}}{l_{MFPb}\mu}\right) - 1 \right) \gamma t_{ba} \right]}{1 - P_a P_{ab} r_{aa} \exp\left(-2\frac{L_{\gamma a}}{l_{MFPa}\mu}\right)},$$

$$G_a^- = \exp\left(-\frac{L_{\gamma a}}{l_{MFPa}\mu}\right) \frac{1 - P_a + P_a \exp\left(-\frac{L_{\gamma a}}{l_{MFPa}\mu}\right) \left[\begin{matrix} 1 - P_{ab}(r_{aa} + \gamma t_{ba}) \\ + \exp\left(-\frac{L_{\gamma b}}{l_{MFPb}\mu}\right) \gamma P_{ab} t_{ba} \end{matrix} \right]}{1 - P_a P_{ab} r_{aa} \exp\left(-2\frac{L_{\gamma a}}{l_{MFPa}\mu}\right)},$$

in which $\gamma = l_{MFPb}/l_{MFPa}$ is MFP ratio and $Kn_a = l_{MFPa}/L_{\gamma a}$.

Fig. 9A shows the heat flux distributions inside the nanofilms on a substrate. Assuming that the materials of the nanofilm and the substrate are Si and Ge, respectively, the mean free path ratio, r_{aa} , r_{bb} , t_{ab} , and t_{ba} can also be calculated based on the average phonon properties of Si and Ge as described earlier. The specular reflectance and transmittance of phonons at the interface can be calculated using the acoustic mismatch model (AMM) [59]. In fact, the phonon reflection and transmission at interface is a complex process, and the factors such as phonon mode conversion and interfacial bonding strength [60] may take effect. Following the method proposed by Prasher [60], the mean values of these quantities are given by,

$$\bar{t}_{Si_Ge (Ge_Si)} = 2 \int_0^{\theta_c} t_{Si_Ge (Ge_Si)} \cos(\theta) d \cos(\theta) \tag{24}$$

$$\bar{r}_{Si_Ge (Ge_Si)} = 1 - \bar{t}_{Si_Ge (Ge_Si)}$$

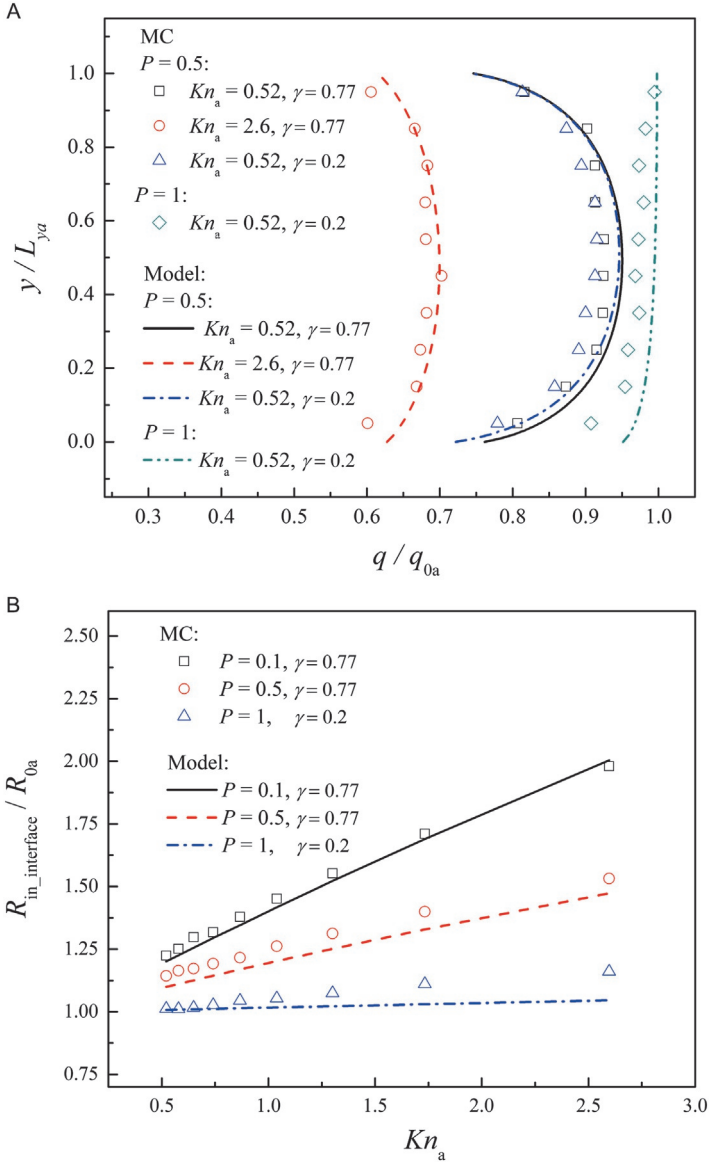


Fig. 9 (A) Heat flux distributions within the nanofilm on a substrate and (B) in-plane thermal resistance of the nanofilm on a substrate.

with

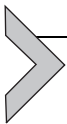
$$\begin{aligned}
 t_{\text{Si}_{-}\text{Ge}}(\text{Ge}_{-}\text{Si}) &= \frac{4z_{\text{Si}}z_{\text{Ge}}\cos(\theta_{\text{Si}})\cos(\theta_{\text{Ge}})}{[z_{\text{Si}}\cos(\theta_{\text{Si}}) + z_{\text{Ge}}\cos(\theta_{\text{Ge}})]^2} \\
 z_{\text{Si}} &= \rho_{\text{Si}}v_{\text{g}_{-}\text{Si}} \\
 z_{\text{Ge}} &= \rho_{\text{Ge}}v_{\text{g}_{-}\text{Ge}} \\
 \sin(\theta_{\text{Si}})/v_{\text{g}_{-}\text{Si}} &= \sin(\theta_{\text{Ge}})/v_{\text{g}_{-}\text{Ge}}.
 \end{aligned} \tag{25}$$

In addition, according to Chen's article [55], when using the AMM, a correction must be made to ensure energy balance across the interface, that is, $\bar{t}'_{\text{Si}_{-}\text{Ge}} = \bar{t}_{\text{Ge}_{-}\text{Si}}(v_{\text{g}_{-}\text{Ge}}C_{V_{-}\text{Ge}}/v_{\text{g}_{-}\text{Si}}C_{V_{-}\text{Si}})$, $\bar{r}'_{\text{Si}_{-}\text{Ge}} = 1 - \bar{r}'_{\text{Si}_{-}\text{Ge}}$.

The heat flux decreases near the boundary and the interface in contact with the substrate, and this slip phenomenon intensifies with increasing Kn number. However, due to the influence of the mismatched phonon properties at the interface, the heat flux distribution becomes asymmetrical. As the MFP ratio is decreased from 0.77 to 0.2, the heat flux near the interface will be further reduced. In a suspended nanofilm, when the specular reflection coefficient is 1, the BHFS will disappear. By contrast, for a nanofilm on a substrate, the phonon property mismatch at the interface alone can lead to the changes in the heat flux distribution. In this case, the in-plane thermal resistance of the nanofilm becomes [27],

$$R_{\text{in_interface}} = R_{0a} \left\{ 1 - \frac{3Kn_a}{4} \int_0^1 (G_a^+ + G_a^-) \left(1 - \exp\left(-\frac{1}{\mu Kn_a}\right) \right) (1 - \mu^2) \mu d\mu \right\}^{-1}. \tag{26}$$

As shown in Fig. 9B, an increase in the Kn number, a decrease in the specular reflectance coefficient, or a decrease in the MFP ratio can lead to an increase in the in-plane thermal resistance of a nanofilm on a substrate. Importantly, even when $P_r = 1$, the in-plane thermal resistance can also increase due to the phonon property mismatch.



3. Effective thermal conductivity of nanostructures

As stated in Section 2, an “effective” or “apparent” thermal conductivity can be defined using the conventional Fourier's law for a specific nanostructure, which holds very different features compared to the intrinsic one of bulk materials. It is a direct experimental evidence of ballistic heat

conduction, and can reflect the thermal transport ability of the structure. Li et al. [61] measured the effective thermal conductivity of silicon nanowires and found that it increases with increasing diameter, and the thermal conductivity of 50 nm-diameter nanowire is only one-fifth of the bulk value of silicon. The subsequent experiments have shown that the effective thermal conductivity can be further reduced to one-hundredth of the bulk value by surface roughening [62]. Liu and Asheghi [63] used Joule heating-based technique to measure the in-plane effective thermal conductivity of nanofilms and found that it increases with increasing thickness. Chen et al. [64] probed the effective thermal conductivity of silicon nanowires varying with temperature and diameter. Hsiao et al. [65] found that the effective thermal conductivity of silicon-germanium nanowires significantly depends on length rather than diameter due to the ballistic transport of long-wavelength phonons. Johnson et al. [66] measured the effective thermal conductivity of a suspended nanofilm and found that even for the thicknesses in the micrometer range, there is still a significant size effect on the effective thermal conductivity.

In particular, the combination of Fourier's law-based model and the proper effective thermal conductivity expressions can realize the efficient thermal modeling of electronic devices with considering the non-Fourier effect [30,38,50]. Therefore, the study of effective thermal conductivity of nanostructures has both theoretical and practical importance.

This section will discuss the factors that can significantly influence the effective thermal conductivities of nanostructures, including: (a) characteristic size and geometry; (b) heating condition; (c) interfacial effect; (d) stress; (e) electric field.

3.1 Effects of size and geometry

There have been many models to predict effective thermal conductivity dependent on the characteristic length for various nanostructures, including nanofilms, nanowires of different cross sections. Majumdar [51] derived a model for the normal thermal conductivity of nanofilms based on the phonon radiation transfer equation. Alvarez and Jou [53] obtained a model for the surface thermal conductivity of thin films from the perspective of extended non-equilibrium thermodynamics. In addition, Lü et al. [67] derived a thermal conductivity model for infinitely long rectangular nanowires based on the phonon radiation transfer equation. Dong et al. [68] derived thermal conductivity models for nanofilms and nanowires based on thermal-mechanical

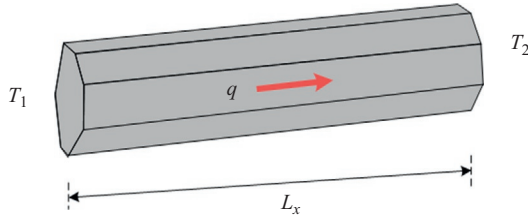


Fig. 10 Schematic for typical suspended multi-constrained nanostructure.

theory, considering the rheological phenomenon of thermal-mechanical fluid properties near the boundary.

Note that most of those models only consider one single characteristic length; however, for the practical nanostructures, phonon transport is always affected by multiple geometric constraints, and thus the effective thermal conductivity can depend on multiple dimensions simultaneously [47].

Fig. 10 shows a typical suspended multi-constrained nanostructure, where the temperature difference is imposed in the x direction (its two ends are respectively in contact with two heat sinks) and phonons scatter at the side boundaries. The length L_x in the axial direction and the characteristic size of cross section are both comparable to the phonon MFPs, so the effective thermal conductivity of this structure can depend on multiple characteristic lengths in this case. It could be difficult to derive an analytical model by directly solving the BTE. Here, we present an effective means to model such multi-constrained effective thermal conductivity through summation and decomposition of thermal resistance, following the work by Hua and Cao [47].

The total thermal resistance of the nanostructure illustrated in Fig. 10 is given by,

$$R_t = \frac{L_x}{S\kappa_{\text{eff}}} = R_0 + R_x + R_l, \quad (27)$$

in which S is the cross-sectional area, R_0 is the intrinsic thermal resistance, R_x represents the thermal resistance caused by x -directional constraint, and R_l refers to that caused by the lateral constraints. R_0 is calculated using the intrinsic thermal conductivity of bulk material, while R_x and R_l can be derived through thermal resistance decomposition as follows.

Firstly, considering only the effect of x -directional constraint, the thermal resistance of the nanostructure is equal to the sum of the intrinsic thermal resistance and that caused by x -directional constraint,

$$R_{cr} = R_0 + R_x = R_0 + \frac{4}{3} \frac{L_x}{S\kappa_0} Kn_x, \quad (28)$$

in which the x -directional Kn number is defined as $Kn_x = l_{MFP}/L_x$. Thus, the thermal resistance caused by x -directional constraint is derived as,

$$R_x = \frac{4}{3} \frac{L_x}{S\kappa_0} Kn_x. \quad (29)$$

Similarly, considering only the effect of lateral constraint, the thermal resistance becomes the sum of the intrinsic thermal resistance and that from the lateral constraint, that is,

$$R_{in} = \frac{L_x}{S\kappa_{in}} = R_0 + R_l, \quad (30)$$

with

$$R_l = R_0(G - 1), \quad (31)$$

in which for an arbitrary cross-section shape, G is given by,

$$G^{-1} = 1 - \frac{3}{2\pi S} \int_S dS \int_0^{2\pi} \int_{\pi/2}^0 \left[\frac{(1 - P) \exp\left(-\frac{|\mathbf{r} - \mathbf{r}_B|}{v_g \tau \sqrt{1 - \mu^2}}\right)}{1 - P \exp\left(-\frac{|\mathbf{r} - \mathbf{r}_B|}{v_g \tau \sqrt{1 - \mu^2}}\right)} \right] \mu^2 d\mu d\varphi \quad (32)$$

Then, according to Eq. (27), the total thermal resistance as well as the multi-constrained effective thermal conductivity are derived,

$$R_t = \frac{L_x}{S\kappa_{eff}} = R_0 + \frac{4}{3} Kn_x R_0 + R_0(G - 1) = R_0 \left(\frac{4}{3} Kn_x + G \right), \quad (33)$$

$$\frac{\kappa_{eff}}{\kappa_0} = \frac{1}{\frac{4}{3} Kn_x + G}. \quad (34)$$

Although the derivation of the above model is based on the gray-body approximation of phonons, it can also be applied to cases considering the dispersion relations, which is given by,

$$\kappa_{eff} = \frac{1}{3} \sum_j \int_0^{\omega_{mj}} \hbar \omega \frac{\partial f_{BE}}{\partial T} v_{g\omega j} l_{bj}(\omega) \text{DOS}_j(\omega) d\omega, \quad (35)$$

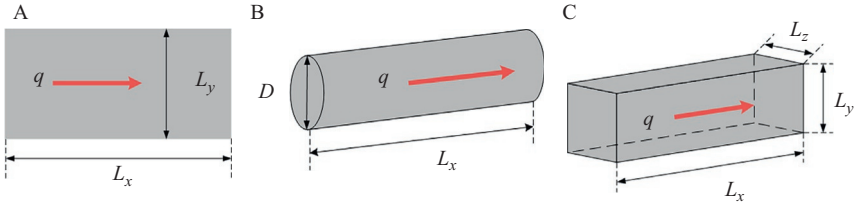


Fig. 11 (A) Nanofilm of finite thickness and length, (B) finite-length cylindrical nanowire, and (C) finite-length rectangular nanowire.

with

$$l_{bj} = \frac{l_{intj}}{\frac{4l_{intj}}{3L_x} + G(l_{intj})}, \quad (36)$$

in which l_{intj} refers to the intrinsic MFP of j phonon branch.

The model above is employed to calculate the effective thermal conductivities of three representative nanostructures: nanofilm of finite thickness and length, finite-length cylindrical nanowire, and finite-length rectangular nanowire, as shown in Fig. 11. The G function for each geometry is given as follows:

$$G_{\text{film}}^{-1} = 1 - \frac{3}{2}Kn_y \int_0^1 \left[1 - \exp\left(-\frac{1}{Kn_y\sqrt{1-\mu^2}}\right) \right] \mu^3 d\mu, \quad (37)$$

$$G_{\text{cir}}^{-1} = 1 - \frac{12}{\pi} \int_0^{1/2} r dr \int_0^{2\pi} d\varphi \int_0^1 \mu^2 d\mu \exp\left\{-\frac{\sin(\varphi - \arcsin[2r\sin(\varphi)])}{2\sin(\varphi)Kn_D}\right\} \quad (38)$$

$$G_{\text{sq}}^{-1} = 1 - \frac{3}{\pi} \int_0^1 dy \int_0^1 dz \int_0^1 \mu^2 d\mu \left\{ \int_{\varphi_1}^{\varphi_2} \exp\left(-\frac{1-y}{[Kn_L\sin(\varphi)\sqrt{1-\mu^2}]}\right) d\varphi + \int_{\varphi_2}^{\varphi_3} \exp\left(-\frac{z}{[Kn_L\cos(\varphi)\sqrt{1-\mu^2}]}\right) d\varphi \right\} \quad (39)$$

where $Kn_y = l_0/L_y$ is the Kn number defined using the film thickness L_y , $Kn_D = l_0/D$ is the Kn number by the diameter D of nanowire, and $Kn_L = l_0/L$ with the cross-section length L .

Fig. 12A shows the effective thermal conductivity of the multi-constrained nanofilm. When Kn_x is given, it decreases as Kn_y increases, and vice versa.

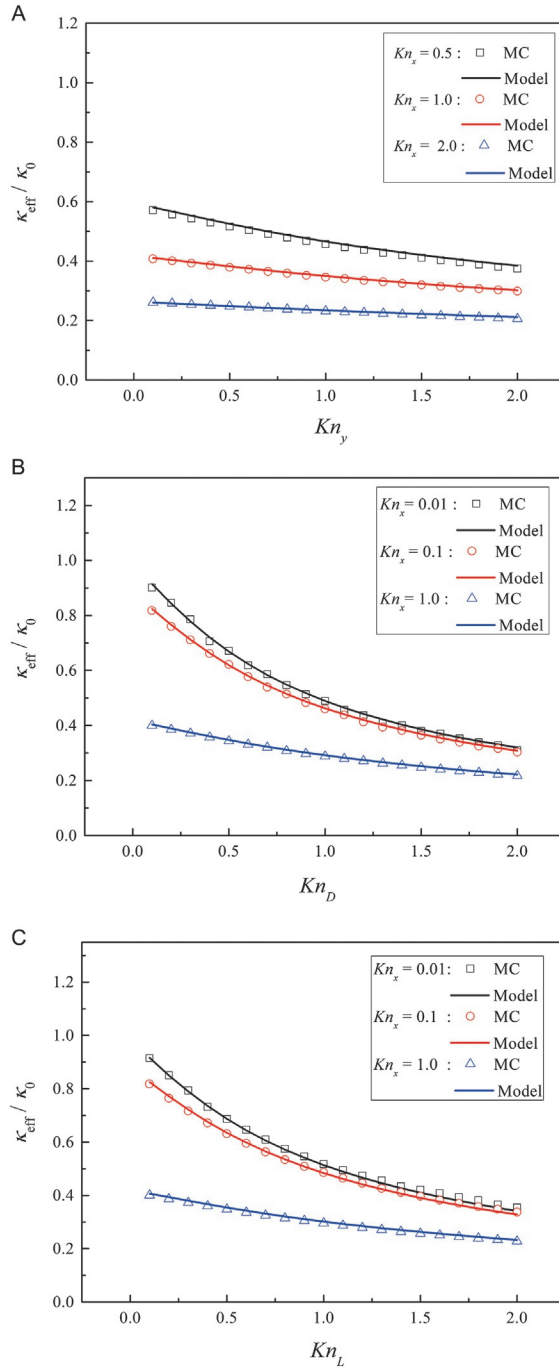


Fig. 12 Effective thermal conductivity of (A) multi-constrained nanofilm; (B) finite-length circular nanowire; and (C) finite-length rectangular nanowire.

The model here agrees well with the results of phonon MC simulations. Fig. 12B and C show the effective thermal conductivity of finite-length cylindrical and rectangular nanowires. The model predictions here also have good consistency with those from the phonon MC simulations.

3.2 Effect of heating conditions

Self-heating of electronic devices, where intensive internal heat source is present at the nanoscale, is a crucial topic for electronic thermal management. Additionally, in order to probe the effective thermal conductivity of a particular nanostructure, imposing temperature difference and internal heating are the two widely-used schemes in experiments or simulations [29]. As shown in Fig. 13A, when using the temperature-difference scheme, the effective thermal conductivity is calculated as the ratio of heat flux to temperature gradient,

$$\kappa_T = \frac{qL_x}{\Delta T}. \quad (40)$$

Fig. 13B illustrates the internal-heating scheme, where the effective thermal conductivity is usually derived from the average temperature rise,

$$\kappa_I = \frac{L_x^2 \dot{S}}{12\Delta \overline{T}}, \quad (41)$$

in which \dot{S} is the internal heat source and the average temperature rise is given by,

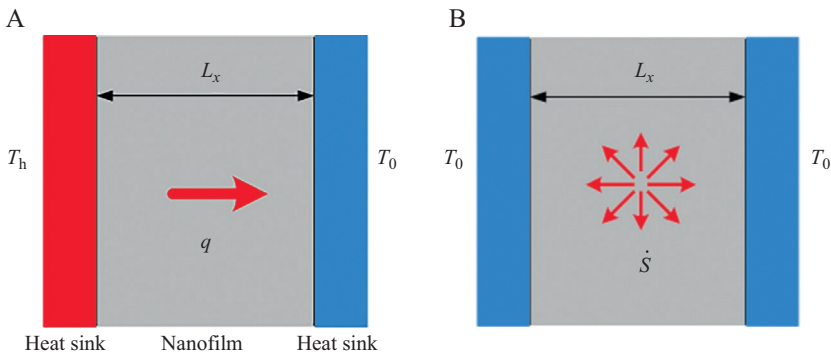


Fig. 13 Schematics for (A) temperature-difference scheme and (B) internal-heating scheme.

$$\Delta \bar{T} = \frac{1}{L_x} \int_{L_x} \Delta T dx. \quad (42)$$

For macroscale heat conduction where Fourier's law is valid, the thermal conductivity obtained by different heating schemes should be identical for one structure. However, for the effective thermal conductivities of nanostructures, this conclusion no longer holds due to ballistic effect. Here, the BTE corresponding to the nanofilm with internal heating, as shown in Fig. 13B, is given by [29],

$$v_g \mu \frac{\partial f}{\partial x} = \frac{f_0 - f}{\tau} + \dot{S}_\Omega \quad (43)$$

with the phonon source term \dot{S}_Ω . Then, the dimensionless temperature distribution is expressed as,

$$\begin{aligned} \Delta T_{Kn_x}^*(\eta) &= \frac{T - T_0}{(\dot{S}L_x^2/8\kappa_0)} = 4(1 - \eta)\eta + \frac{8}{3}Kn_x \\ &\quad - \frac{Kn_x^2}{3} \left[\exp\left(-2\frac{1 - \eta}{Kn_x}\right) + \exp\left(-2\frac{\eta}{Kn_x}\right) \right] \\ &\quad + \frac{Kn_x^2}{3} \left[1 + \exp\left(-\frac{2}{Kn_x}\right) \right] \end{aligned} \quad (44)$$

with $\eta = x/L_x$. As $Kn_x = 0$, Eq. (44) is reduced to the diffusive solution,

$$\Delta T_{Kn_x=0}^*(\eta) = 4(1 - \eta)\eta. \quad (45)$$

As shown in Fig. 14A, temperature jumps occur at the boundaries, which increase with increasing Kn number, meanwhile the average temperature rise inside the nanofilm also significantly increases. In the range of small Kn number, the model, Eq. (44), can well predict the results of phonon MC simulations. As the Kn number is very big, the model will underestimate the temperature rise.

Then, the effective thermal conductivity from the internal heating scheme following Eq. (41) is given by,

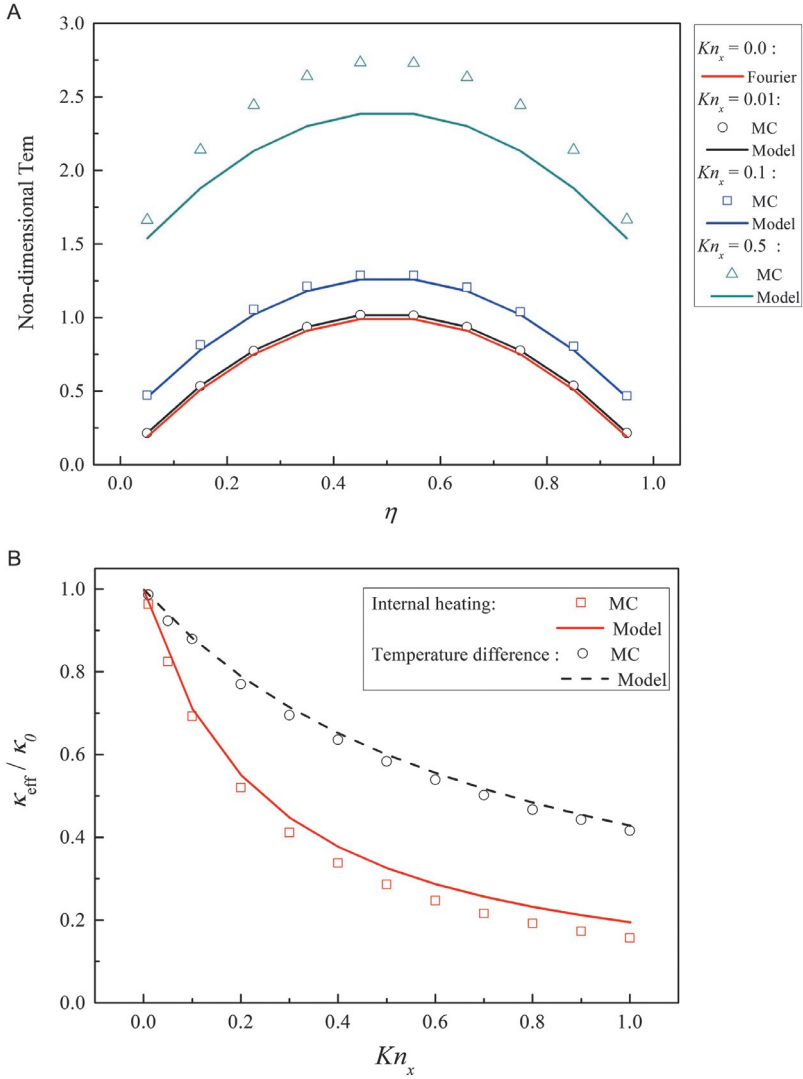


Fig. 14 (A) Temperature distributions in nanofilms of internal heating and (B) effective thermal conductivity under different heating conditions.

$$\frac{\kappa_1}{\kappa_0} = \frac{1}{1 + 4Kn_x + \frac{Kn_x^2}{2} \left[1 + \exp\left(-\frac{2}{Kn_x}\right) \right] + \frac{Kn_x^3}{2} \left[\exp\left(-\frac{2}{Kn_x}\right) - 1 \right]} \approx \frac{1}{1 + 4Kn_x} \tag{46}$$

According to Fig. 14B, the model, Eq. (46) can well predict the effective thermal conductivity obtained by phonon MC simulations for the internal heating scheme. It is found that in this case the effective thermal conductivity of nanofilm also decreases with the increase of Kn number. As a comparison, the effective thermal conductivity of the same nanofilm under the temperature-difference scheme is expressed as [51],

$$\frac{\kappa_T}{\kappa_0} = \frac{1}{1 + \frac{4}{3}Kn_x} \quad (47)$$

Comparing Eqs. (46) and (47), it can be found that due to ballistic effect, the effective thermal conductivity of one nanofilm obtained under different heating conditions becomes different. The simulations and model calculations in Fig. 14B both show that the effective thermal conductivity of nanostructures with internal heat sources becomes lower than that under the temperature-difference condition. This indicates that in the case of internal heating, the phonons emitted from inside the nanofilm are more easily affected by boundaries.

3.3 Interfacial effect

Generally, the presence of interfaces leads to an increase in thermal resistance. However, experiments by Yang et al. [69] have shown that van der Waals (vdW) interfaces between two identical materials in nanofilms can increase the effective thermal conductivity. Subsequently, some researchers have also found the same phenomenon through molecular dynamics simulations [57,70–72]. In fact, interfaces are usually present between two different materials, which means that the mismatch of phonon properties can also have a significant impact on heat transport. Based on molecular dynamics simulations, Zhang et al. [73] found that the thermal conductivity of graphene on the substrate can be enhanced or suppressed by changing the properties of the substrate. However, it is still an open question whether the mismatch of phonon properties at the interface can enhance the thermal conductivity. Moreover, due to the lack of a unified and rigorous analytical model, some controversies still exist even for the extensively studied heat transfer in graphene. For example, the MD simulation results by Ong and Pop [74] showed that the thermal conductivity of graphene gradually increases with increasing binding strength between graphene and the substrate; however, Qiu and Ruan [75] reached the opposite conclusion that stronger interface binding strength will further reduce

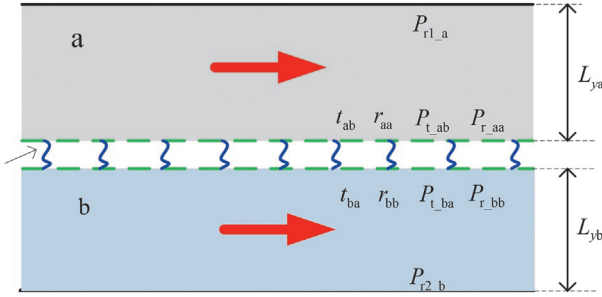


Fig. 15 In-plane heat conduction in a bilayer nanofilm.

the thermal conductivity of graphene. The impact of phonon property mismatch at interfaces on heat transport mainly involves three factors [76]: (a) interface adhesion energy, (b) interface roughness, and (c) phonon property mismatch near the interface.

Fig. 15 illustrates a bilayer nanofilm system that generally exists in electronic devices, like high electron mobility transistors [38]. The governing equations in this case are the same as those, Eqs. (21a) and (21b), presented in Section 2.

Particularly for this problem, a more detailed discussion of boundary and interface conditions is necessary [76]:

$$\begin{aligned}
 \Delta f_a(L_{ya}, \nu_{y_a} < 0) &= P_{r1,a} \Delta f_a(L_{ya}, \nu_{y_a} > 0) \\
 \Delta f_a(0, \nu_{y_a} > 0) &= P_{r,aa} r_{aa} \Delta f_a(0, \nu_{y_a} < 0) + P_{t,ba} t_{ba} \Delta f_b(0, \nu_{y_b} > 0) \\
 \Delta f_b(0, \nu_{y_b} < 0) &= P_{r,bb} r_{bb} \Delta f_b(0, \nu_{y_b} > 0) + P_{t,ab} t_{ab} \Delta f_a(0, \nu_{y_a} < 0) \\
 \Delta f_b(-L_{yb}, \nu_{y_b} > 0) &= P_{r2,b} \Delta f_b(L_{yb}, \nu_{y_b} < 0)
 \end{aligned} \quad (48)$$

in which $P_{r,aa}$ and $P_{r,bb}$ are the specular reflection coefficients at the interface in the nanofilms a and b respectively, $P_{t,ab}$ describes the transmission that phonons in nanofilm a penetrate into nanofilm b (ballistic penetration does not change the propagation direction, while diffusive penetration leads to random propagation direction), and $P_{t,ba}$ is for the mode in which phonons in nanofilm b penetrate into nanofilm a. Then, the effective thermal conductivity of nanofilm a can be derived from the phonon BTE [76],

$$\frac{\kappa_{\text{eff}_a}}{\kappa_{0_a}} = 1 - \frac{3}{4} \int_0^1 \int_0^1 \left(G_a^+ \exp\left(-\frac{\gamma}{\mu} \frac{1}{Kn_a}\right) + G_a^- \exp\left(\frac{\gamma}{\mu} \frac{1}{Kn_a}\right) \right) (1 - \mu^2) d\mu dy \quad (49)$$

with $Kn_a = l_{0a}/L_{ya}$, and

$$G_a^+ = \frac{\left\{ \begin{aligned} & (1 - P_{r1_a})P_{r_{aa}}r_{aa} \exp\left(-\frac{1}{Kn_a\mu}\right) + \exp\left(-\frac{1}{Kn_b\mu}\right)\gamma(1 - P_{r2_b})P_{t_{ba}}t_{ba} \\ & + (1 - P_{r_{aa}}r_{aa} - \gamma P_{t_{ba}}t_{ba}) - (1 - P_{r1_a}) \cdot \\ & P_{r2_b}(P_{r_{aa}}P_{r_{bb}}r_{aa}r_{bb} - P_{t_{ab}}P_{t_{ba}}t_{ab}t_{ba}) \exp\left(-2\frac{1}{Kn_b\mu} - \frac{1}{Kn_a\mu}\right) \\ & + \exp\left(-2\frac{1}{Kn_b\mu}\right) \cdot \\ & P_{r2_b}(\gamma P_{t_{ba}}t_{ba} - P_{r_{bb}}r_{bb} + P_{r_{aa}}P_{r_{bb}}r_{aa}r_{bb} - P_{t_{ab}}P_{t_{ba}}t_{ab}t_{ba}) \end{aligned} \right\}}{\left\{ \begin{aligned} & 1 - \exp\left(-\frac{2}{Kn_a\mu}\right)P_{r1_a}P_{r_{aa}}r_{aa} - \exp\left(-\frac{2}{Kn_b\mu}\right)P_{r2_b}P_{r_{bb}}r_{bb} \\ & + P_{r1_a}P_{r2_b}(P_{r_{aa}}P_{r_{bb}}r_{aa}r_{bb} - P_{t_{ab}}P_{t_{ba}}t_{ab}t_{ba}) \cdot \\ & \exp\left(-\frac{2}{Kn_a\mu} - \frac{2}{Kn_b\mu}\right) \end{aligned} \right\}}, \quad (50a)$$

$$G_a^- = \frac{\left\{ \begin{aligned} & \exp\left(-\frac{1}{Kn_a\mu}\right) \left\{ \begin{aligned} & (1 - P_{r1_a}) - \exp\left(-2\frac{1}{Kn_b\mu}\right)(1 - P_{r1_a})P_{r2_b}P_{r_{bb}}r_{bb} \\ & + \exp\left(-\frac{1}{Kn_a\mu} - \frac{1}{Kn_b\mu}\right)\gamma P_{r1_a}(1 - P_{r2_b})P_{t_{ba}}t_{ba} \\ & + \exp\left(-\frac{1}{Kn_a\mu} - 2\frac{1}{Kn_b\mu}\right) \cdot \\ & P_{r1_a}P_{r2_b} \left[\begin{aligned} & \gamma P_{t_{ba}}t_{ba} - P_{r_{bb}}r_{bb} + \\ & P_{r_{bb}}P_{r_{aa}}r_{aa}r_{bb} - P_{t_{ab}}P_{t_{ba}}t_{ab}t_{ba} \end{aligned} \right] \\ & + \exp\left(-\frac{1}{Kn_a\mu}\right)P_{r1_a}(1 - P_{r_{aa}}r_{aa} - \gamma P_{t_{ba}}t_{ba}) \end{aligned} \right\} \end{aligned} \right\}}{\left\{ \begin{aligned} & 1 - \exp\left(-\frac{2}{Kn_a\mu}\right)P_{r_{aa}}P_{r_{aa}}r_{aa} - \exp\left(-\frac{2}{Kn_b\mu}\right)P_{r2_b}P_{r_{bb}}r_{bb} \\ & + P_{r1_a}P_{r2_b}(P_{r_{aa}}P_{r_{bb}}r_{aa}r_{bb} - P_{t_{ab}}P_{t_{ba}}t_{ab}t_{ba}) \exp\left(-\frac{2}{Kn_a\mu} - \frac{2}{Kn_b\mu}\right) \end{aligned} \right\}} \quad (50b)$$

The interface parameters in the model depend on the interfacial roughness, adhesion energy, and the mismatch between the phonon properties at the interface. Generally, the specular reflection coefficient increases with decreasing interface roughness. According to Li and McGaughey's paper [77], the specular coefficient for the reflected phonons is usually smaller than that for the transmitted phonons. The phonon transmission coefficient is

determined by the adhesion energy and phonon property mismatch at the interface. Referring to the improved AMM proposed by Prasher [60], increasing the interface adhesion energy can enhance the phonon transmission coefficient, while the phonon property mismatch will impede phonon transmission.

3.3.1 The case of identical-material interface

Identical-material interface refers to the case where the materials on both sides of the interface are the same, which are generally caused by van der Waals contacts between the identical materials. In this case, phonon transmission is mainly determined by interfacial adhesion energy. Here, assuming that both layers a and b are single-crystal Si materials, the physical parameters given in Chen's article [55] are adopted. Considering the symmetry of the structure, we have: $P_{r1_a} = P_{r2_b}$, $P_{r_aa} = P_{r_bb}$, $P_{t_aa} = P_{t_bb}$, $t_{ab} = t_{ba}$, $r_{aa} = r_{bb}$, and $\kappa_{\text{eff}_a} = \kappa_{\text{eff}_b}$.

Fig. 16A compares the effective thermal conductivity of a bilayer nanofilm with completely smooth interface with that of a suspended nano single-layer film (thickness = L_y). Here, $L_{ya} = L_{yb} = L_y$ and the Kn number is defined as $Kn = l_0/L_y = l_0/L_{ya}$. A completely smooth interface means that the ballistic transmission coefficient and the specular reflection coefficient are both equal to 1. First, the simulation results are in good agreement with the model predictions, verifying the reliability of the model. Both the simulations and model indicate that the in-plane effective thermal conductivity of bilayer nanofilm with completely smooth interface is equal to that of suspended single-layer nanofilm, that is, the ballistic transmission and specular reflection of phonons on the identical-material interface will have no effect on the effective thermal conductivity. This conclusion was also reached by Chen et al. [70] in their MD simulations. In fact, as shown in Fig. 16B, even for non-completely smooth interfaces, as long as the specular reflection coefficient equals the ballistic transmission coefficient, the in-plane effective thermal conductivity of the bilayer nanofilm will not be affected.

Referring to Fig. 17, to observe the change in the effective thermal conductivity of a bilayer nanofilm, the ballistic transmission coefficient at the interface must be nonequal to the specular reflection coefficient. For instance, when the specular reflection coefficient at the interface is set to 0.2 and the ballistic transmission coefficient is 1 (phonons pass through the interface ballistically), both the simulations and model show that the interface can enhance the ability of heat conduction: the in-plane effective thermal conductivity of the bilayer nanofilm containing interface will be higher than that of the suspended nanofilm, and the enhancement effect

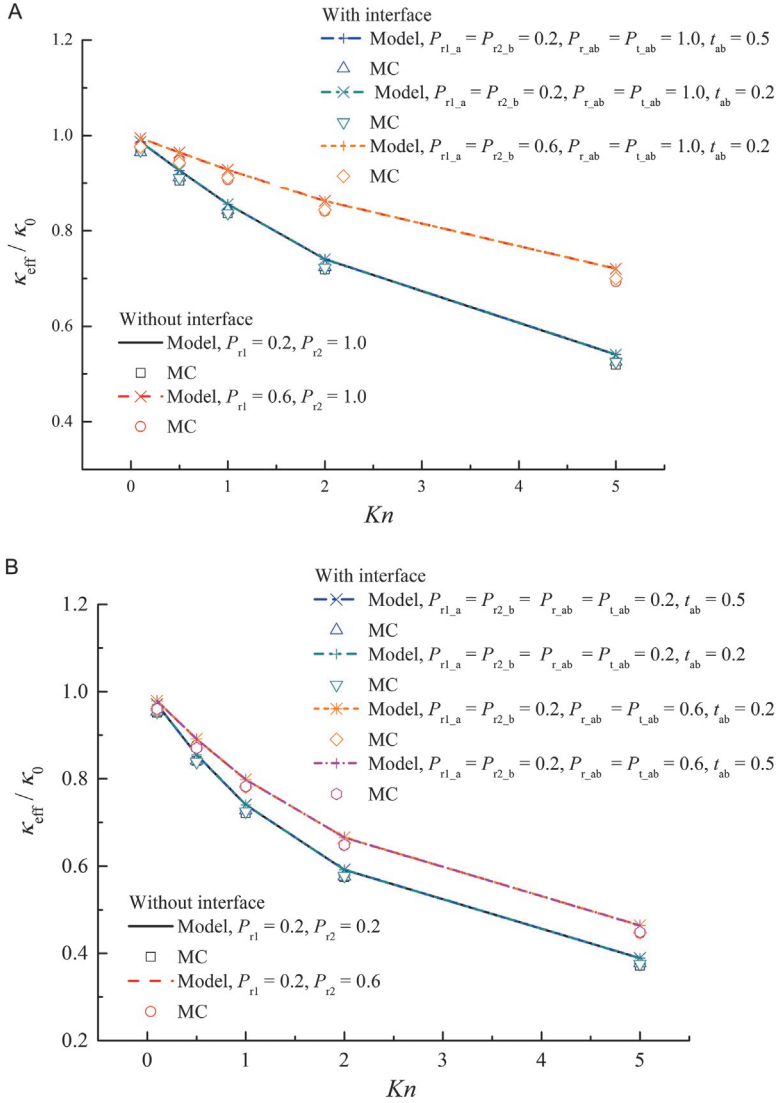


Fig. 16 (A) Comparison between the effective thermal conductivity of a bilayer nanofilm with a completely smooth interface and that of a suspended nanofilm and (B) effective thermal conductivity of a bilayer nanofilm with a rough interface, where the ballistic transmission coefficient is equal to the specular reflection coefficient.

of the effective thermal conductivity increases with the increase of phonon transmission coefficient.

Furthermore, the interface can provide coupling between the two layers. In the extreme case where the phonon transmission rate is equal to 1,

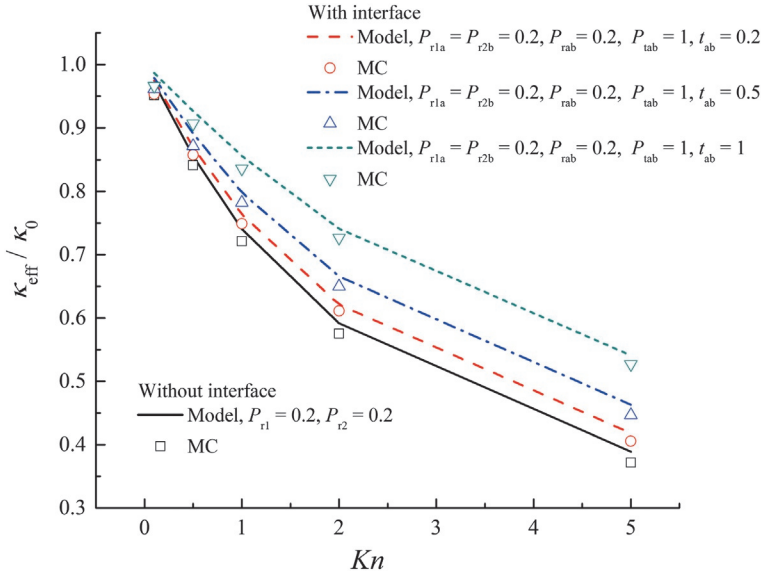


Fig. 17 The case of non-smooth interface: the transmission coefficient is 0.2, 0.5 and 1.

phonons pass through the interface ballistically without any scattering. In this case, the bilayer nanofilm is equivalent to a suspended monolayer nanofilm of double thickness. Increasing the thickness will lead to an increase in the effective thermal conductivity. Although it is difficult for the phonon transmission coefficient at the interface to reach 1 in practice, the coupling between the two layers can still increase the effective thermal conductivity to some degree. As shown in Fig. 18, the specular reflection coefficient is 0.5, the phonon transmission coefficient is 0.5, and the interface ballistic transmission coefficients range from 0 to 1. It is found that the interface will enhance the effective thermal conductivity when the ballistic transmission coefficient is higher than the specular reflection coefficient. On the contrary, the in-plane effective thermal conductivity of the bilayer nanofilm will be lower than that of the suspended monolayer nanofilm.

3.3.2 The case of disparate-material interface

Disparate-material interface refers to the case where the materials on the two sides are different, and there is mismatch in phonon properties. According to the derived model in Eq. (49), the mismatch in phonon properties at the interface is mainly reflected by the ratio of MFPs between the two materials, denoted by γ . In order to demonstrate the effect of MFP ratio on the

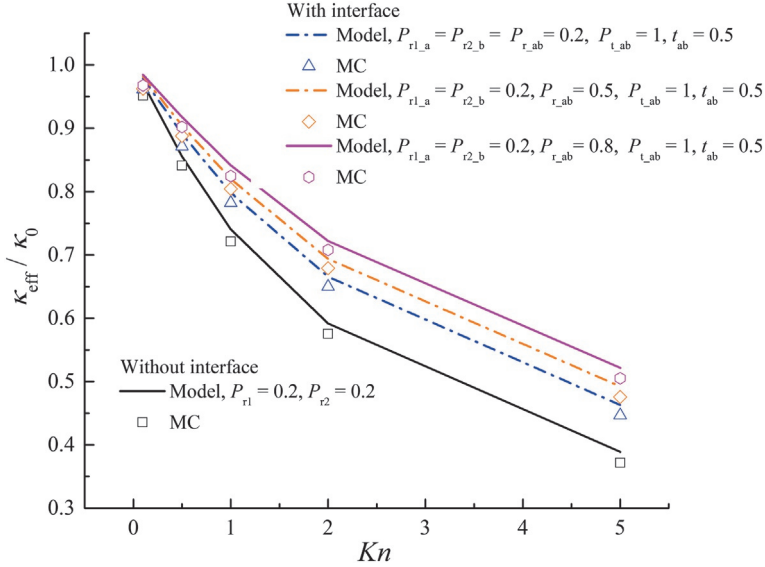


Fig. 18 The case of non-smooth interface: the specular reflection coefficient equal to 0.5.

effective thermal conductivity, by fixing the intrinsic MFP of Layer a and changing that of Layer b, the MFP ratio is varied to examine the influence of the interface on the in-plane effective thermal conductivity of Layer a. In Fig. 19A, with the Kn number of 1 and the phonon transmission coefficient of 0.5, the MFP ratios are set as 0.5, 1.0, and 1.5, respectively. In spite of varied MFP ratios, the in-plane effective thermal conductivity always increases with the increasing specular reflection coefficient at the interface. Fig. 19B shows that the in-plane effective thermal conductivity also increases with the increasing ballistic transmission coefficient. Therefore, it can be concluded that regardless of the presence of phonon property mismatch, increasing the smoothness of the interface can always enhance thermal conduction.

In addition, the interfacial phonon transmission is an important parameter for regulating effective thermal conductivity. Both Yang et al. [69] and Sun et al. [72] stated that the key to whether the interfacial effect can enhance the effective thermal conductivity lies in whether the interface phonon transmission is strong enough. Fig. 20 shows the variation of the nanofilm's in-plane effective thermal conductivity with the changed interfacial phonon transmission. According to Fig. 20A, the Kn number is equal to 1, the ballistic transmission coefficient is equal to 1, the specular reflection coefficient is equal to 0.5, and the MFP ratio is 0.5, 1.0, and 1.5, respectively.

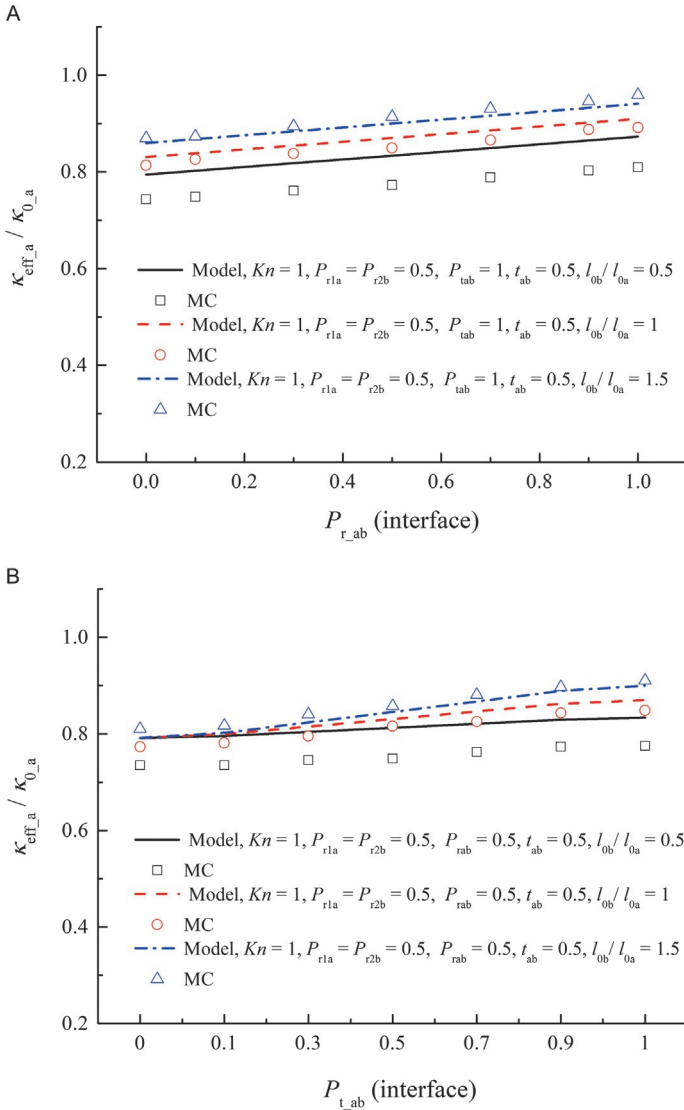


Fig. 19 (A) Effective thermal conductivity for partially smooth interface varying with interfacial specular reflection coefficient and (B) effective thermal conductivity for partially smooth interface varying with interfacial ballistic transmission coefficient.

When the MFP ratio is bigger than or equal to 1, the interface will enhance the effective thermal conductivity, and the enhancement effect will become more significant as the phonon transmission increases. However, when the MFP ratio is less than 1, the variation of effective thermal conductivity with the phonon transmission coefficient will become more complicated.

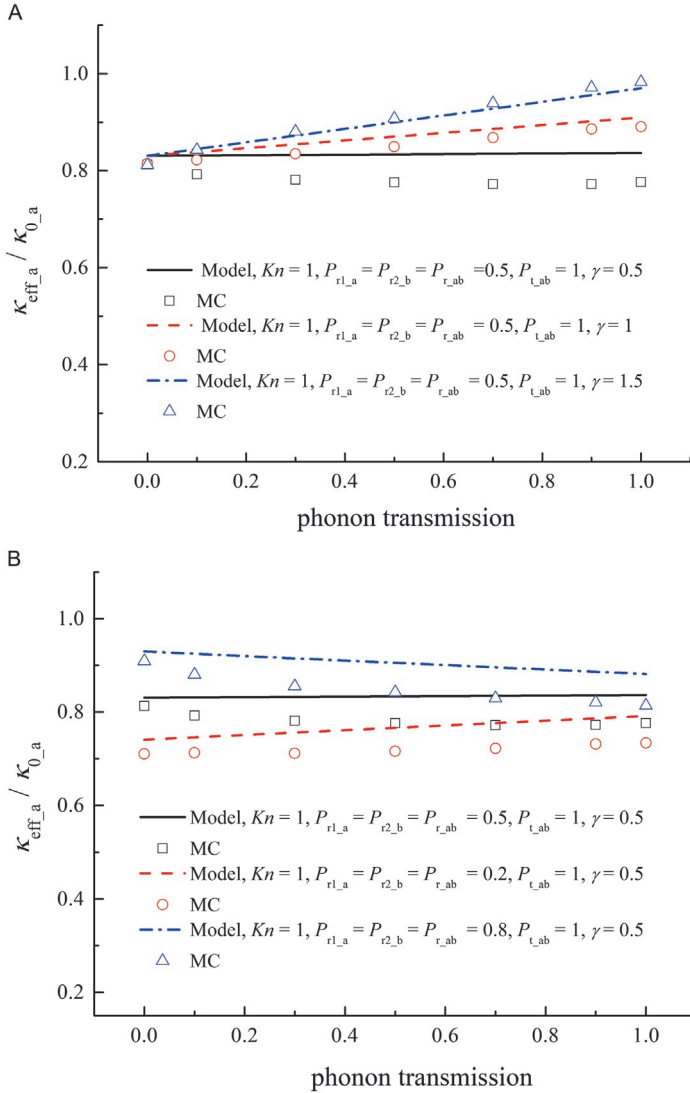


Fig. 20 Effective thermal conductivity for partially smooth interface varying with phonon transmission coefficient: (A) ballistic transmission coefficient = 1, specular reflection coefficient = 0.5, and MFP ratios are 0.5, 1.0, and 1.5, respectively and (B) ballistic transmission coefficient = 1, MFP ratio = 0.5, and specular reflection coefficients are 0.2, 0.5, and 0.8.

In Fig. 20B, the MFP ratio is set to 0.5, and the specular reflection coefficient is 0.2, 0.5, and 0.8, respectively. When the mirror reflection coefficient is small (i.e., 0.2), the effective thermal conductivity increases with the transmission coefficient, but when the specular reflection coefficient is large

(i.e., 0.8), it decreases with the increasing transmission rate. This is because there are two competitive factors that affect the effective thermal conductivity: phonons that pass through the interface ballistically will enhance thermal transport, while the mismatch in phonon properties due to the MFP ratio being less than 1 will hinder heat conduction. When the interfacial specular reflection coefficient is small, if phonons cannot pass through the interface, there is a high probability that they will undergo diffuse reflection at the interface. In this case, the first factor dominates, and the effective thermal conductivity increases as the number of phonons passing through the interface (i.e., the transmission coefficient) increases. Conversely, when the interfacial specular reflection coefficient is large, the second factor dominates, and the increasing phonon transmission coefficient results in the stronger interlayer coupling and the decrease in effective thermal conductivity. This explains the differences in simulation results between Ong and Pop [74] and Qiu and Ruan [75]: the different interfacial conditions between graphene and silicon dioxide substrate will cause different variations in the thermal conductivity of graphene with the interfacial bonding strength.

3.4 Effects of external fields

External fields, including the stress field and electric field, are typical factors affecting the thermal transport of semiconductors in electronics [78,79], and they are also common methods to tune phonon thermal transport in semiconductors such as GaN [80,81]. In this section, the effects of stress and electric fields on phonon thermal transport in GaN are comprehensively discussed.

3.4.1 Stress field

In particular, strain inevitably exists in practical GaN-based devices due to the mismatch of lattice structures and thermal expansion caused by heteroepitaxial growth and band engineering, and significantly influences the thermal properties of GaN [78]. Actually, from the perspective of property tuning, strain is also necessary in devices. Specific strain is required for designing electronic properties through band engineering. Besides, strain can be applied as a positive method to control the properties of electrons, photons, and phonons, since these properties are sensitive to strain [82].

With the aid of first-principles calculations and phonon Boltzmann transport theory, the lattice constants, phonon properties, and thermal conductivity of GaN under different strained states are systematically investigated [81]. The strain is applied by changing the lattice constants of the structure. Then the structure is relaxed, with the other lattice constant being settled.

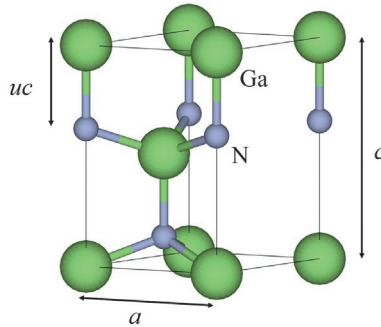


Fig. 21 The lattice structure of wurtzite GaN with lattice constants a and c , and internal parameter u .

The biaxial strain is expressed by the relative variation of the lattice constant $\sigma_a = (a - a_0)/a_0$, where the lattice constants can be referred to in Fig. 21. With biaxial strain, at a range of -5% to $+5\%$, changes in the lattice structure and crystal symmetry are not detected under strain states, i.e., GaN is still in wurtzite structure with space group $P6_3mc$. The lattice thermal conductivity changes monotonically and significantly under different strain states, as shown in Fig. 22A–C. The results show that the lattice thermal conductivity decreases under the tensile strain state and increases under the compressive strain state. In detail, under $+5\%$ tensile strain state, average thermal conductivity at room temperature decreases by 63% while it increases by 53% under -5% compressive strain. This is mostly attributed to changes in phonon relaxation time based on detailed phonon analyses [81]. The anisotropy of the lattice thermal conductivity is weak in the free state, but it becomes larger under strained states. Under a tensile strain state, the cross-plane lattice thermal conductivity is larger than the cross-plane thermal conductivity, while the opposite is true under a compressive strain state. This difference in anisotropy, corresponding to different changes of squared in-plane and cross-plane group velocity, is a consequence of the weakening effect from strain-induced polarization, which screens the strain effects partially. The dimensionless cumulative thermal conductivity with respect to phonon frequency in Fig. 22D–E shows that the cut-off phonon frequency decreases to 6.2 THz when the dimensionless cumulative thermal conductivity reaches 90% under the tensile strain state, while it increases to 7.1 THz under the compressive strain state. The size effect is promising to become stronger under a compressive strain state while it weakens under a tensile strain state. In detail, the phonon free path is $3.7 \mu\text{m}$ when the dimensionless cumulative thermal conductivity reaches 90%, and it mainly ranges from 150 to 4000 nm under a compressive strain state. Under the tensile

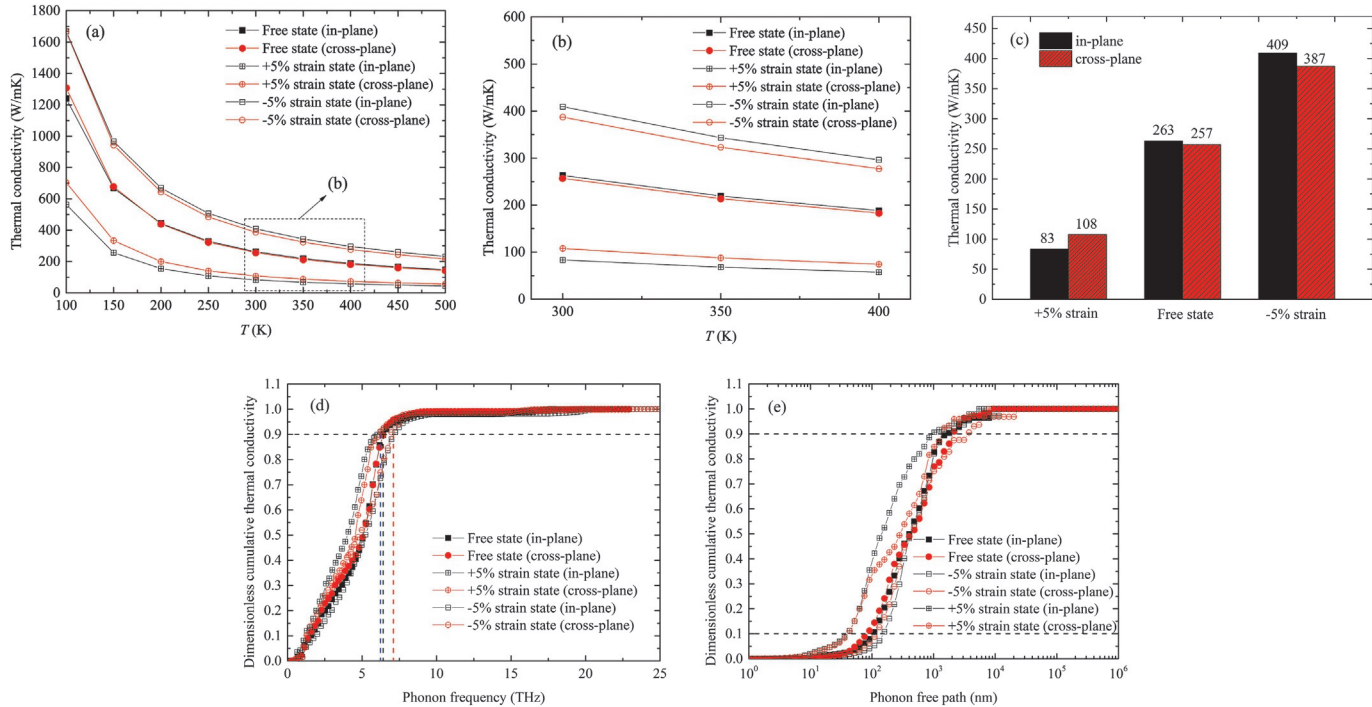


Fig. 22 Thermal conductivity of GaN concerning (A–C) temperature, (D) frequency, and (E) free path under different strain states. From D.-S. Tang, G.-Z. Qin, M. Hu, B.-Y. Cao, *Thermal transport properties of GaN with biaxial strain and electron-phonon coupling*, *J. Appl. Phys.* 127(3) (2020) 035102.

strain state, the phonon free path decreases to 1.2 μm for 90% dimensionless cumulative thermal conductivity and mainly ranges from 40 to 1500 nm.

3.4.2 Electric field

The electric field commonly exists in semiconductor structures in electronics since it plays a key role in manipulating electrons. Moreover, applying an external electric field is an effective way to adjust the electrical and thermal transport properties of dielectric materials [83]. Theoretically, the response of a lattice to a finite homogeneous electric field can be classified into three parts [84]: (i) the response of the electron wave function (density distribution), which can be represented by Born effective charges and the dielectric function, as well as interatomic force constants in phonon calculations; (ii) changes in atomic coordinates; and (iii) lattice strain, including an electronic part and a lattice part. Hence, for materials whose electronic or lattice response to an electric field is strong, their thermal conductivity can be tuned by an external electric field.

Compared to the calculations for strain fields, calculating the responses of three-dimensional periodic lattice structures to finite electric fields from first principles is not an easy task. The main difficulty is that the scalar potential “ $-\mathbf{E}\cdot\mathbf{r}$ ” (where \mathbf{E} is the electric field and \mathbf{r} is the position vector) is non-periodic and unbounded from below. Under the framework of the modern theory of polarization, Souza *et al.* developed an appropriate variance method based on the minimization of electric enthalpy functional [85]. Methods for calculating the total energy of periodic solids, as well as forces, stress, Born effective charges, dielectric function, and phonon properties from first principles, were then proposed. These advancements made it possible to perform first-principles calculations for three-dimensional solids at finite electric fields.

Recently, Tang and Cao performed an investigation on phonon and the phonon transport properties of wurtzite GaN in finite electric fields [80]. Considering the limit from bandgap (3.49 eV) of wurtzite GaN, reduced electric fields are selected to range from -0.02 and 0.02 in the atomic unit, corresponding to absolute electric fields -1.035×10^9 and 1.040×10^9 V/m, respectively. The electric fields are applied along the polar axis of the GaN lattice, and the lattice symmetry is conserved under this kind of electric field. It is noted here that the calculations are not stable when the electric field is perpendicular to the polar axis. In Fig. 23A, the thermal conductivity is presented for a temperature range of 300–500 K, with a specific focus on the thermal conductivity at 300 K, as shown in Fig. 23B. Both positive and

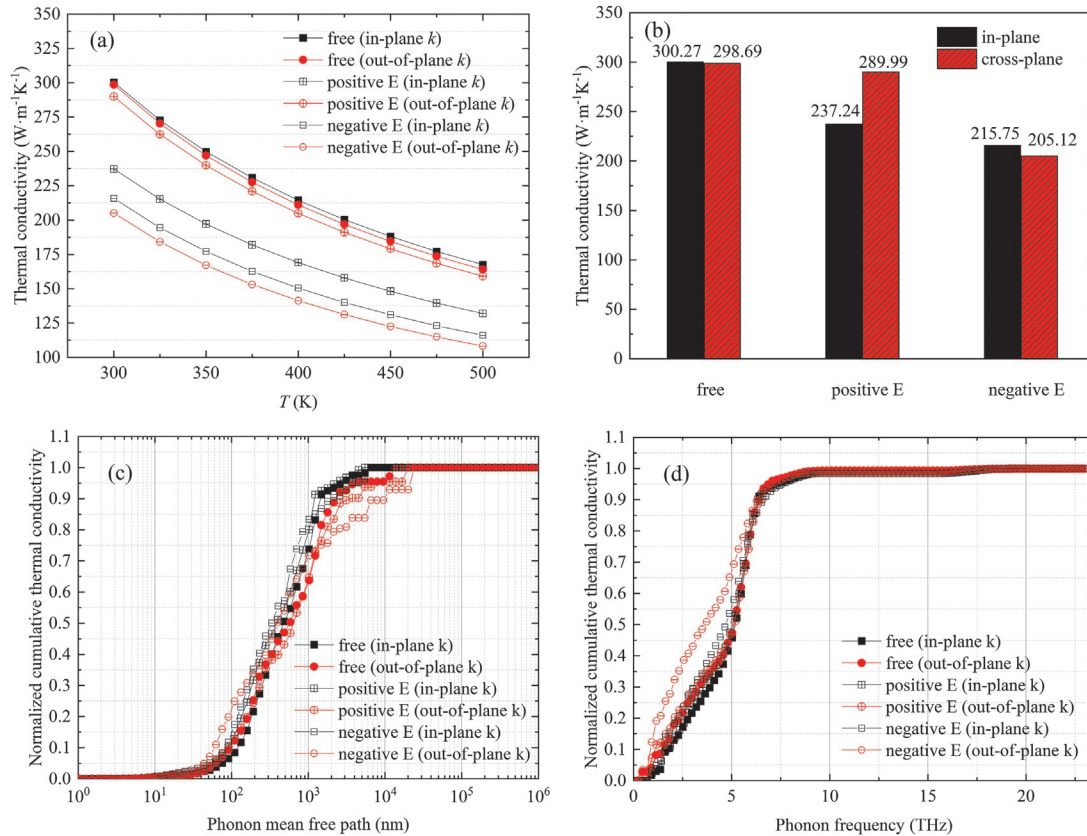
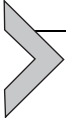


Fig. 23 Thermal conductivity of GaN concerning (A and B) temperature, (C) frequency, and (D) free path at electric fields. From D.-S. Tang, B.-Y. Cao, *Phonon thermal transport properties of GaN with symmetry-breaking and lattice deformation induced by the electric field*, *Int. J. Heat Mass Transf.* 179 (2021) 121659.

negative electric fields result in large decreases in thermal conductivity. In detail, the decrease in in-plane thermal conductivity at a positive electric field (positive direction along the z -axis) is relatively small, while the out-of-plane thermal conductivity decreases significantly. At negative electric field states, both the in-plane and out-of-plane thermal conductivities decrease significantly. Furthermore, anisotropy increases under a finite electric field, while thermal conductivity remains nearly isotropic under zero electric field. Here, the thermal conductivity along the polar axis is regarded as the out-of-plane thermal conductivity, and that in the direction perpendicular to the polar axis is the in-plane thermal conductivity. It is deduced that changes in the distribution of phonon mode properties are responsible for the decrease in thermal conductivity under electric fields, as no significant differences are found in phonon properties [81]. Further quantitative analyses confirm that the change in relaxation time is the main reason for changes in lattice thermal conductivity under electric fields. This change results from the increase in the anharmonicity of interatomic interactions. Fig. 23C and D show the normalized cumulative thermal conductivity with respect to phonon mean free path and frequency, respectively. The maximum mean free path at the free state, i.e., at zero electric fields, is around $10\ \mu\text{m}$. Corresponding to the variances in lattice thermal conductivity under finite electric fields, the changes in the maximum phonon mean free paths are, however, not significant. The maximum phonon free path remains nearly constant for the out-of-plane condition, while a slight increase occurs for the in-plane condition. Since electric fields do not significantly shift or reduce low-frequency phonon branches, the maximum cut-off frequencies are nearly kept constant under electric fields.

For wurtzite GaN, Quan *et al.* also performed a systematic first-principles study on the electric field effect on thermal conductivity [86]. While the phonon dispersion with the electric field remains nearly constant, the thermal conductivity undergoes significant changes. The thermal conductivity parallel to the electric field increases, with a more than 12% increase at 200 K and an 8% increase at higher temperatures, while the thermal conductivity perpendicular to the electric field decreases by 7%. This is attributed to differences in the stiffness of the Ga-N bond, ionicity, and scattering rates of phonons travelling in different directions. In their work, the researchers also investigated the condition where an electric field is applied along the in-plane direction. In this condition, the lattice structure becomes unstable and all crystal symmetries are lost. As a result, thermal conductivity decreases due to the accompanying increase in phonon-phonon scatterings.



4. Thermal spreading resistance in ballistic-diffusive regime

4.1 Thermal spreading resistance

Thermal spreading resistance is a common phenomenon in electronic devices, which occurs when heat is transferred from a small heat source region to a much larger area [36]. As shown in Fig. 1, in GaN HEMTs heat is generated in the 2DEG region at the top of the GaN layer, which has a small width ranging from a few hundred nanometers to several micrometers, depending on the bias voltage and channel length [33]. As heat spreads from the heat source to the substrate, there is a significant thermal spreading resistance that is much greater than the one-dimensional thermal resistance [19]. The one-dimensional thermal resistance in the GaN layer is defined by Eq. (51)

$$R_{1D0} = \frac{t}{w\kappa_0}, \quad (51)$$

where t , w , κ_0 are the thickness, width, and the intrinsic thermal conductivity of the device layer, respectively. To quantify the thermal spreading resistance, the total thermal resistance is defined by Eq. (52),

$$R_{\text{hs_tot}} = \frac{\bar{T}_s}{Q_{\text{hs}}} = R_{\text{sp0}} + R_{1D0}. \quad (52)$$

where Q_{hs} is the total heating power and \bar{T}_s is the mean heat source temperature. The thermal spreading resistance R_{sp0} can then be calculated as the difference between the total thermal resistance and the one-dimensional thermal resistance.

The researchers have conducted in-depth studies on the thermal spreading resistance. Despite extensive research on thermal spreading resistance, most analytical solutions or numerical simulations are based on Fourier's law of heat conduction. Muzychka et al. derived an analytical solution for the thermal spreading resistance of eccentric heat sources on rectangular flux channels [34], which was subsequently extended by Muzychka et al. and Gholami et al. to incorporate interfacial thermal resistance, anisotropic thermal conductivities, and arbitrary hot spot locations [87,88]. Darwish et al. considered a more realistic scenario and developed a thermal resistance model for HEMT devices, taking into account the temperature dependence of thermal conductivity [89].

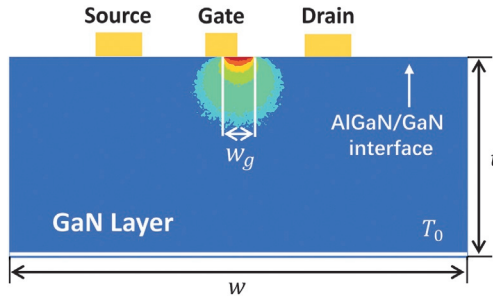


Fig. 24 Schematic of thermal spreading process of the GaN layer in GaN HEMT.

As an example, in the case of thermal spreading transport in the GaN layer, as depicted in Fig. 24, the total thermal resistance based on Fourier's law can be expressed by Eq. (53),

$$\frac{R_F}{R_{1d-0}} = 1 + \left(\frac{w}{w_g}\right)^2 \left(\frac{w}{t}\right) \sum_{n=1}^{\infty} \frac{8 \sin^2\left(\frac{w_g n \pi}{2w}\right) \cdot \cos^2\left(\frac{n \pi}{2}\right)}{(n \pi)^3 \coth\left(\frac{n \pi}{w}\right)}. \quad (53)$$

4.2 Influence of phonon ballistic transport

In electronic devices, the MFP of phonons is comparable to the thickness of the device layer and the width of the heat source, which can lead to significant ballistic effects that affect the thermal spreading resistance. For example, in GaN, Ziade et al. observed a significant size effect in the thermal conductivity of thin films ranging from 10 to 1000 nm in the temperature range of 300–600 K [90]. Using phonon MC simulation, Ma et al. found that when the thickness of GaN films is less than 10 μm, non-Fourier effects should be considered [91]. Therefore, it is essential to take into account ballistic effects in the modeling of thermal spreading resistance. This section presents a study of thermal spreading resistance in the ballistic-diffusive regime using phonon MC simulation [30]. The proposed model is compared with the results predicted by finite element method (FEM). Additionally, the model derived using Fourier's law is re-examined, and a new model that can consider ballistic effects is developed. Fig. 24 is the structure under investigation, which is a simplified model for the thermal spreading process in the GaN layer.

Fig. 25 depicts the dimensionless temperature distributions calculated using MC and FEM, respectively. The dimensionless temperature, denoted by θ_{hs} , is defined as

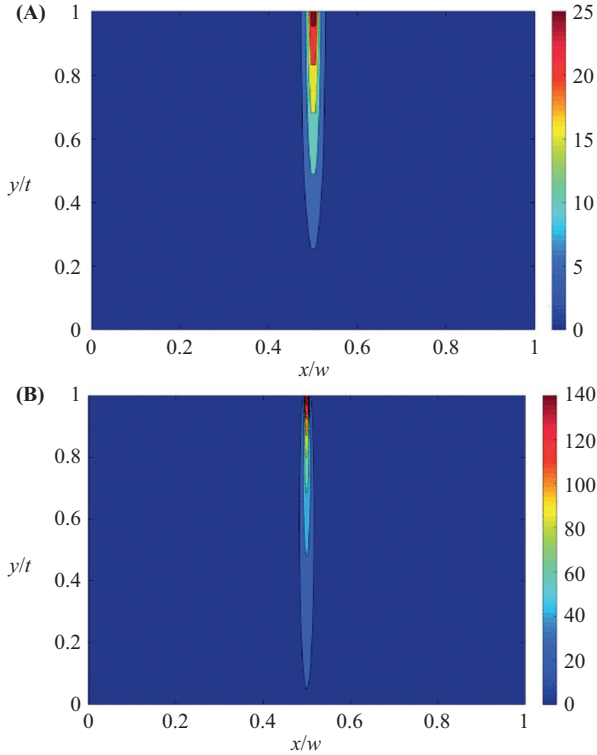


Fig. 25 Dimensionless temperature distributions with $w/t = 40$ and $w_g/w = 0.01$. (A) FEM and (B) MC, $Kn_t = 2$, $Kn_w = 5$.

$$\theta_{\text{hs}} = \frac{\Delta T}{Q_{\text{hs}} R_{1\text{D}0}}. \quad (54)$$

Two Knudsen numbers, Kn_t and Kn_w are defined to quantify the strength of the ballistic effects, where $Kn_t = l_0/t$ and $Kn_w = l_0/w_g$. l_0 is the intrinsic phonon MFP. The dimensionless temperatures obtained from FEM simulations reveal that the thermal spreading effect alone can lead to a significant increase in the peak value of the dimensionless temperature. For instance, as shown in Fig. 25A, when $w/t = 40$ and $w_g/w = 0.01$, the peak temperature is about 25 times higher than that predicted by one-dimensional heat conduction. In addition, as shown by the MC simulation results (Fig. 25B), the ballistic effect can further increase the peak value of the dimensionless temperature. Also, in phonon ballistic transport, internal phonon scattering is limited, resulting in a longer and narrower high-temperature region. As a result, due to the altered dimensionless temperature distribution in the

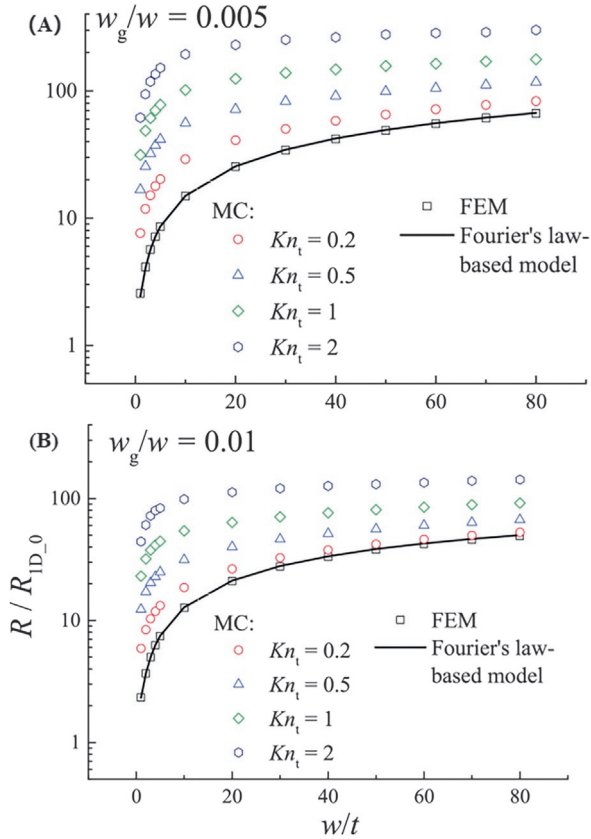


Fig. 26 Dimensionless total thermal resistance as a function of w/t , with (A) $w_g/w = 0.005$ and (B) 0.01.

ballistic-diffusive regime, the total thermal resistance of the structure increases significantly compared to predictions based on Fourier's law.

Fig. 26 compares the dimensionless total thermal resistance predicted by MC, FEM, and Fourier's law-based models (Eq. 53). It can be observed that when only the thermal spreading effect is considered, the dimensionless total thermal resistance depends solely on w_g/w and w/t . The dimensionless total thermal resistance increases with decreasing w_g/w and approaches a plateau value with increasing w/t . The model based on Fourier's law of heat conduction agrees well with the FEM simulations, indicating that the model describes the thermal spreading process accurately.

Moreover, the MC simulation results show that the variance law of the dimensionless total thermal resistance with w_g/w and w/t in the ballistic-diffusive regime is almost identical to that predicted by the model based on Fourier’s law. Therefore, it can be assumed that the thermal spreading effect can still be approximated by Fourier’s law even in the ballistic-diffusive regime. Fig. 25 only exhibits the Kn_t dependence of thermal resistance, Kn_w is not shown since it is not an independent variable,

$$Kn_w = Kn_t / [(w_g/w)(w/t)]. \tag{55}$$

The relationship between thermal resistance and Kn_w can be investigated by calculating the ratio of thermal resistance between MC and Fourier’s law-based models. Fig. 27 shows that the thermal resistance ratio is always

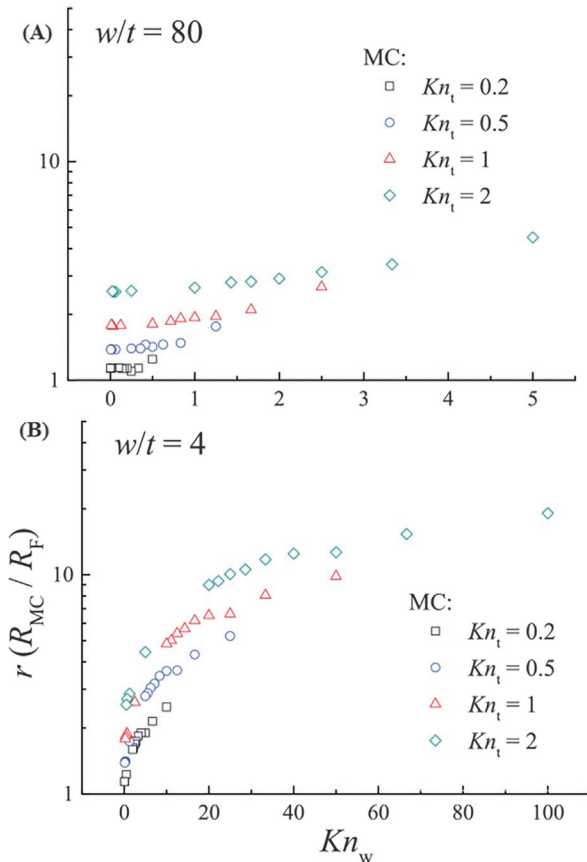


Fig. 27 Thermal resistance ratio as a function of Kn_w , with (A) $w/t = 40$ and (B) 4.

greater than 1 and increases with increasing Kn_w . This implies that the ballistic effect with the size of the heat source comparable to MFP significantly enhances the total thermal resistance.

To develop a more accurate thermal resistance prediction model that considers both thermal spreading and ballistic effects, the phonon BTE can be combined with fitting simulation results. The resulting model is expressed as Eq. (56),

$$\frac{R}{R_{1D_0}} = \frac{R_F}{R_{1D_0}} \left(1 + \frac{2}{3} Kn_t \right) r_w, \quad (56)$$

where R_F is the total thermal resistance calculated using Fourier's law, $1+2/3Kn_t$ is introduced to account for the cross-plane effect, and $r_w = (1+A_wKn_w)$ is used to characterize the ballistic effect with the size of the heat source comparable to phonon MFP, in which A_w is a fitting parameter.

4.3 Influence of phonon dispersion

The thermal resistance model developed in the previous section is based on the gray-medium approximation, which replaces the whole MFP spectrum with a representative MFP. However, the MFP spread of actual semiconductor materials is significantly wide [25]. Freedman et al. discovered that for GaN, AlN, and 4H-SiC, phonons with MFP greater than 1000 ± 230 , 2500 ± 800 , and 4200 ± 850 nm, respectively, contribute more than 50% to the bulk thermal conductivity at room temperature [92]. Therefore, it is essential to extend the gray model to include the phonon dispersion. This section presents a study of thermal spreading resistance with the dispersion of various typical wide-bandgap semiconductors, including GaN, SiC, AlN, and Ga₂O₃, in the ballistic-diffusion regime, using MC simulations [50]. Based on the gray model, a thermal resistance model that can consider the influence of phonon dispersion is developed.

The sine-shaped Born-von Karman dispersion is adopted for all materials. The relationship between the frequency ω and the wave vector k is $\omega(k) = \omega_{\max} \sin(\pi k/2k_m)$ [37]. The essential phonon scattering mechanisms for the considered materials include impurity scattering (I) and Umklapp phonon-phonon scattering (U). The corresponding relaxation time can be expressed as $\tau_I^{-1} = A\omega^4$ and $\tau_U^{-1} = B\omega^2 T \exp(-C/T)$, where A, B, and C are fitting constants [41]. The total relaxation time can be calculated using Matthiessen's rule, $\tau^{-1} = \tau_I^{-1} + \tau_U^{-1}$. Parameters of different materials

Table 1 Phonon dispersion and relaxation time.

Parameter (unit)	GaN	SiC	AlN	Beta-Ga ₂ O ₃
$k_0(1 \times 10^9 \text{ m}^{-1})$	10.94	8.94	11.94	6.74
$\omega_m(1 \times 10^{13} \text{ rad/s})$	3.50	7.12	5.18	1.60
$a_D(\text{\AA})$	2.87	3.51	2.81	4.66
$A(1 \times 10^{-45} \text{ s}^3)$	5.26	1.00	10.50	1.38E-6
$B(1 \times 10^9 \text{ s/K})$	1.10	0.60	0.74	9.31
$C(K)$	200.00	235.00	287.50	62.60

can be obtained by fitting the measured thermal conductivities. Table 1 shows the fitted parameters for the studied materials.

To account for the phonon dispersion from the gray model approximation, we can adopt a method similar to that used to calculate the size-dependent thermal conductivity by integrating the phonon spectrum [47],

$$\kappa_{\text{eff}} = \frac{1}{3} \sum_j \int_0^{\omega_j} \hbar \omega \frac{\partial f_0}{\partial T} v_{g\omega j} l_{j,m} \text{DOS}_j(\omega) d\omega. \quad (57)$$

The phonon branch-dependent effective MFP can be calculated using Eq. (58),

$$l_{m,j} = \frac{l_{0,j}}{\left(1 + A_w(w_g/w, w/t) Kn_{w-\omega,j}\right) \left(1 + \frac{2}{3} Kn_{t-\omega,j}\right)} l_{j,m}, \quad (58)$$

where $l_{0,j}$ is the intrinsic MFP of phonons with a given frequency and phonon branch.

$Kn_{w-\omega,j} = l_{0,j}/w_g$ and $Kn_{t-\omega,j} = l_{0,j}/t$ are the Knudsen number of phonon at the given mode. The effective thermal conductivity can be calculated using given phonon dispersion and then used in Fourier's law-based model to calculate the total thermal resistance of the system. This method is referred to as the gray model in the following sections. It should be noted that Eq. (57) is normally used to account for the contribution of phonons in different modes to the heat flow of the system. In thermal spreading problems, this treatment is only an approximation and may lead to inevitable deviations. However, it is a simple way to roughly consider the complex phonon dispersion in thermal modeling of electronic devices.

Fig. 28 presents the dimensionless total thermal resistance of GaN, calculated using MC simulation and the gray model. Although the gray model

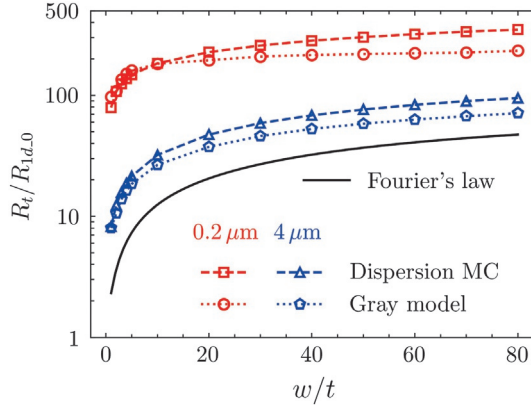


Fig. 28 Dimensionless total thermal resistance of GaN as a function of w/t predicted by the model and MC simulations, with $w_g/w = 0.01$, $t = 0.2$, and $4 \mu\text{m}$, respectively.

can approximately reflect the variation law of the total thermal resistance, the maximum deviation between the model-predicted results and the MC-simulated results exceeds 30%. To improve the accuracy of the model and clarify the source of deviations, it is necessary to analyze the two kinds of ballistic effects separately in the system, which include the cross-plane ballistic effect and the ballistic effect with the size of the heat source comparable to the phonon MFP.

To eliminate the deviations caused by the heat source-related ballistic effect, the r_w directly extracted from MC simulations are substituted for $(1 + A_w(w_g/w, w/t)Kn_{w-\omega, j})$ in Eq. (58), resulting in Eq. (59),

$$l_{m,j,1} = \frac{l_{0,j}}{\left(1 + \frac{2}{3}Kn_{t-\omega,j}\right)r_{w,\text{dispersion}}} \quad (59)$$

Fig. 29 illustrates the dimensionless total thermal spreading resistance calculated using MC simulation and the model based on Eq. (59). In this case, the MC-simulated total thermal resistance is always higher than the model-predicted values, and the deviation increases as t decreases. To eliminate the deviations caused by the cross-plane ballistic effect, we can define the ratio of MC-predicted thermal resistance to the model-predicted resistance as r_t . Then, by incorporating r_t in the gray model, the deviations caused by the cross-plane ballistic effect can be eliminated, and the new deviations will be solely caused by the heat source-related ballistic effect.

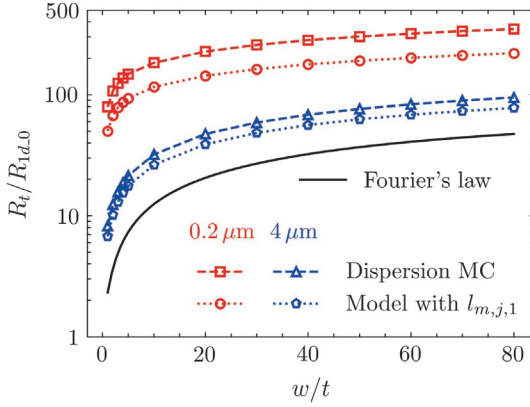


Fig. 29 Dimensionless total thermal resistance of GaN as a function of w/t predicted by the model based on $l_{m,j,1}$ and MC simulations, with $w_g/w = 0.01$, $t = 0.2$, and $4 \mu\text{m}$, respectively.

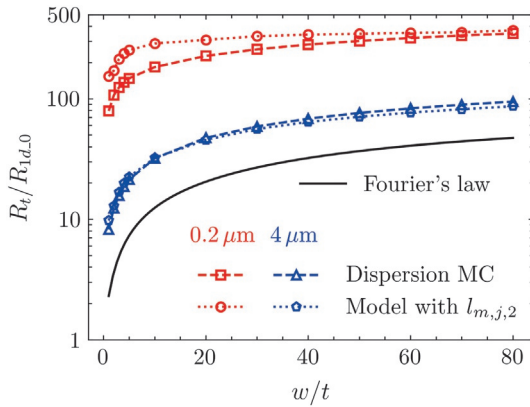


Fig. 30 Dimensionless total thermal resistance of GaN as a function of w/t predicted by the model based on $l_{m,j,2}$ and MC simulations, with $w_g/w = 0.01$, $t = 0.2$, and $4 \mu\text{m}$, respectively.

$$l_{m,j,2} = \frac{l_{0,j}}{\left(1 + A_w Kn_{w-\omega,j}\right)\left(1 + \frac{2}{3} Kn_{t-\omega,j}\right) r_t}, \quad (60)$$

Fig. 30 displays the dimensionless total thermal spreading resistance calculated using MC simulation and the model based on Eq. (60). In this case, the model-predicted values agree well with the MC-simulated results for larger t values. However, for smaller t values, the deviations increase as w/t decreases. We can define the ratio between the total thermal resistance

predicted by the MC simulation and the model as r_{wg} . By using the average MFP of different materials, r_t and r_{wg} can be well fitted with material-independent parameters. Then, the original gray model can be extended to the case involving phonon dispersion by adding two correction terms,

$$l_{m,j,r} = \frac{l_{0,j}}{\left(1 + A_w K n_{w-\omega,j}\right) \left(1 + \frac{2}{3} K n_{t-\omega,j}\right) r_t r_{wg}}. \quad (61)$$

Fig. 31 presents the dimensionless thermal resistance predicted by the MC simulation and the revised model. The results demonstrate that the thermal resistance value is considerably dependent on the material type, and the prediction results of the developed model are in good agreement with the MC simulation results. The model can be applied to different materials and accurately estimate the thermal resistance values for systems with various geometric parameters.

4.4 Influence of bias-dependent heat generation

Most studies on thermal spreading resistance assume that the heat source has the same length as the gate, which is modelled as either a surface heat flux or a uniform volumetric heat source on the top of the GaN layer [30,93]. However, in electronic devices, the primary heat source is Joule heating, which is highly bias-dependent and non-uniform [94]. The different heat source distributions in the channel can significantly impact the thermal spreading process and the strength of the phonon ballistic effects simultaneously [32]. In this section, we integrate technology computer-aided design (TCAD) and phonon MC simulations to conduct electrothermal

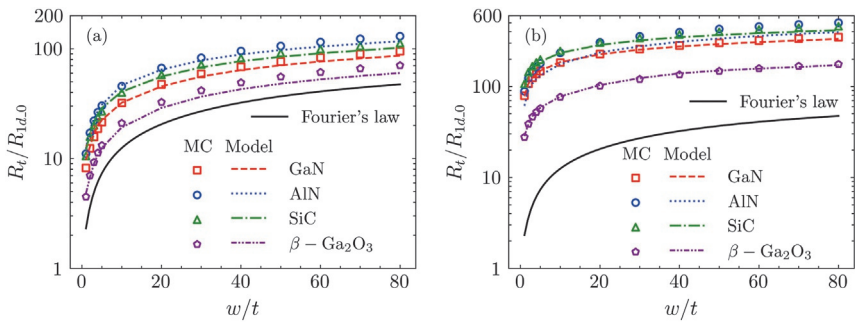


Fig. 31 Dimensionless total thermal resistance of different semiconductor materials as a function of w/t predicted by the newly-proposed model and MC simulations, with $w_g/w = 0.01$ and (A) $t = 4$ and (B) $t = 0.2 \mu\text{m}$.

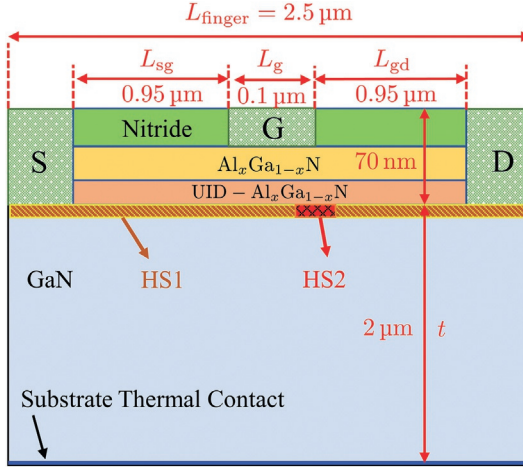


Fig. 32 Schematic of the GaN HEMT for TCAD simulations. S, G, D refer to the source, gate, and drain, respectively.

simulations and investigate the thermal spreading resistance in GaN HEMTs [38]. Based on the two-heat-source model, we propose a new two-thermal-conductivity model that reflects the bias-dependent non-Fourier thermal spreading resistance in GaN HEMTs.

The GaN HEMT used for TCAD simulations is depicted in Fig. 32, following the device structure presented in Ref. [95]. The device consists of layers arranged from top to bottom, which include a 50 nm silicon nitride passivation layer, an 18 nm $\text{Al}_{0.25}\text{Ga}_{0.75}\text{N}$ layer with a donor concentration of $N_D = 2 \times 10^{18} \text{ cm}^{-3}$, a 2 nm unintentionally doped (UID) $\text{Al}_{0.25}\text{Ga}_{0.75}\text{N}$ spacer layer with a donor concentration of $N_D = 1 \times 10^{15} \text{ cm}^{-3}$, a 2 μm GaN buffer layer, and a 10 nm SiC substrate layer. The gate length is $L_g = 0.1 \mu\text{m}$, and the source and drain access regions have a length of $L_{sg} = L_{gd} = 0.95 \mu\text{m}$. The total length of the active region is $L_{\text{finger}} = 2.5 \mu\text{m}$.

Electrothermal TCAD simulations are conducted to predict the heat generation profiles at different biases, which are then used to drive the phonon MC simulations. The drift-diffusion model (DDM) is utilized for electron transport. The simulated output characteristics of the HEMT, as shown in Fig. 33, exhibited good agreement with the experimental results.

Fig. 34 illustrates the heat generation profiles in the channel at two biases with an identical power dissipation $P_{\text{diss}} = 5 \text{ W/mm}$ extracted from the TCAD simulations. The heat generation is concentrated within a 2 nm region below the AlGaN/GaN interface and is highly dependent on the bias.

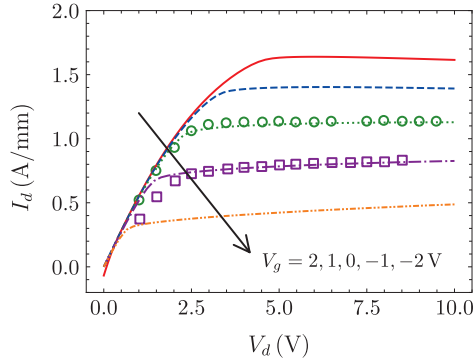


Fig. 33 Output characteristics of the HEMT from -2 to 2 V with an interval of 1 V extracted from TCAD simulations (lines) and experimental results (symbols) [95].

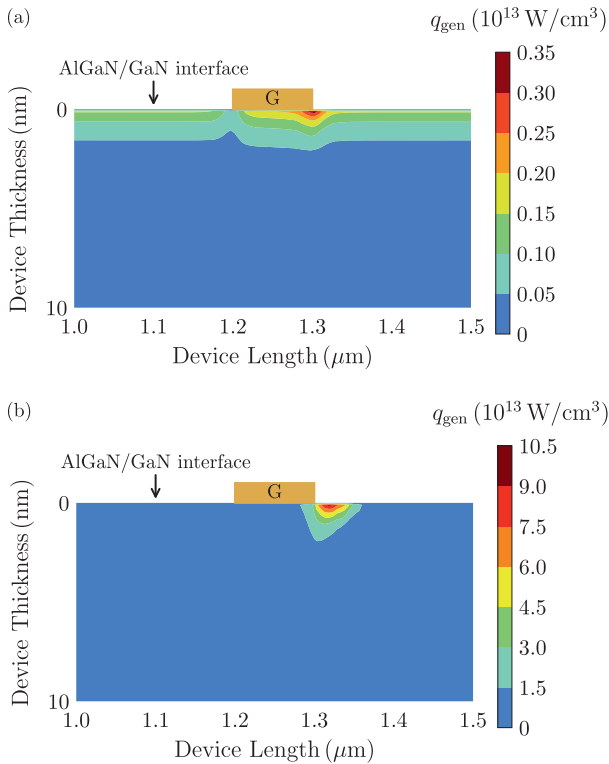


Fig. 34 Heat generation in the channel extracted from TCAD simulations at two biases (A) $V_g = 2$ V, $V_d = 3.8$ V and (B) $V_g = -1$ V, $V_d = 6.7$ V with an identical power dissipation $P_{\text{diss}} = 5$ W/mm.

At a bias of $V_g = 2$ V, the heat is relatively uniformly distributed throughout the channel. However, at a bias of $V_g = -1$ V, the heat is concentrated at the drain-side gate edge, resulting in a significantly larger heat density in that region.

To account for the non-uniform electric field in the channel and the resulting bias-dependent heat generation, Chen et al. proposed a two-heat-source model [19], as illustrated in Fig. 32. The total heat dissipation is divided into two parts: Heat Source 1 (HS1) represents the relatively low and uniform heat generation in the channel, spanning the entire finger length. Heat Source 2 (HS2) is centered at the drain-side gate edge and represents the concentrated heat generation under high electric field. The length of HS1 (L_{HS1}) is equal to the finger length, while the length of HS2 (L_{HS2}) is set to $0.16 \mu\text{m}$ to approximate the length of the high-field region. The width of the high-field region is nearly independent of the bias and device geometry. When the device operates in the linear regime, i.e., V_d is less than the drain saturation voltage V_{dsat} , all the heat is dissipated in HS1. As the channel is pinched off and the device enters the saturation regime, i.e., $V_d > V_{\text{dsat}}$, the heat dissipated in HS1 remains constant, and the excess heat is only dissipated in HS2. The two-heat-source model can be expressed as:

$$\begin{cases} P_1 = I_d V_d, P_2 = 0, & V_d \leq V_{\text{dsat}} \\ P_1 = I_d V_{\text{dsat}}, P_2 = I_d (V_d - V_{\text{dsat}}), & V_d > V_{\text{dsat}} \end{cases} \quad (62)$$

where P_1 and P_2 are the power dissipations in HS1 and HS2, respectively.

Fig. 35 presents the channel temperature profiles predicted by the MC simulations and FEM for the two biases. The heat generation profiles result

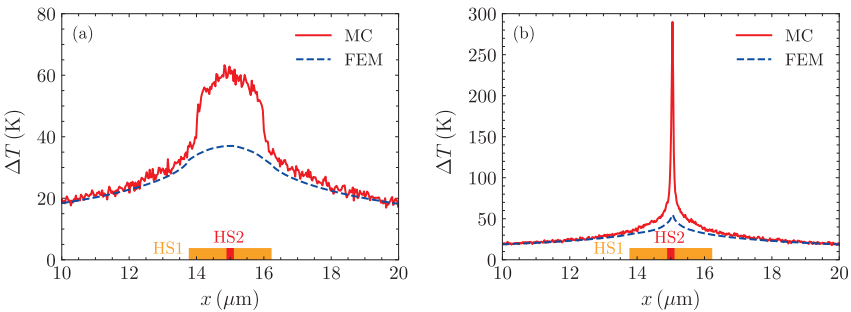


Fig. 35 Comparison of the channel temperature profiles at two biases (A) $V_g = 2$ V, $V_d = 3.8$ V and (B) $V_g = -1$ V, $V_d = 6.7$ V with an identical power dissipation $P_{\text{diss}} = 5$ W/mm computed by the MC simulations and FEM.

in distinct temperature distributions. At $V_g = 2$ V, the temperature distributions in the heat source region are smooth, and the difference between the MC simulations and FEM is not too significant, since the width of the heat source is relatively large and the phonon ballistic effect is weak. In contrast, at $V_g = -1$ V, the highly concentrated heat generation in HS2 leads to a small-sized hotspot and a strong phonon ballistic effect, causing a significant increase in the temperature. This observation is consistent with the experimental results [50].

Through the analysis conducted in the previous sections, two types of ballistic effects have been identified in the thermal spreading process of the GaN layer: cross-plane ballistic effect and ballistic effect associated with the heat source size. The former is influenced solely by the GaN layer thickness, while the latter is affected by the heat source dimensions. These two effects can be effectively modeled using the effective thermal conductivity approach. To this end, we calculate the effective thermal conductivities for HS1 and HS2, with widths $L_{\text{HS1}} = L_{\text{finger}}$ and $L_{\text{HS2}} = 0.16$ μm , respectively. For the phonon properties and geometric parameters adopted in this work, k_{eff} of HS1 and HS2 are $k_{\text{HS1}} = 94.47$ W/mK and $k_{\text{HS2}} = 47.38$ W/mK, respectively. By combining the two-heat-source model and the two-thermal-conductivity model, the junction temperature of the HEMT can be computed as,

$$T_m = T_0 + \frac{k_{\text{bulk}}}{k_{\text{HS1}}} P_1 R_1 + \frac{k_{\text{bulk}}}{k_{\text{HS2}}} P_2 R_2, \quad (63)$$

where T_0 is the highest temperature at the bottom of the GaN layer determined using the FEM, R_1 and R_2 are the thermal resistance values associated with HS1 and HS2, respectively. We note that since the heat transport in the HEMT is not a one-dimensional process, the thermal resistance model presented here is an approximation that reflects the impact of the ballistic effects on the GaN layer's thermal resistance. Fig. 36 shows the overall temperature rise of the HEMT at various biases computed using the MC simulations and the model based on the FEM results and demonstrates good agreement between the two at different biases and power dissipations.

It is worth noting that although the heat source-related phonon ballistic effect can significantly increase the temperature at the drain-side gate edge, it has a negligible impact on the electrical performance degradation of GaN HEMTs. This is because at the drain-side gate edge, the electric field is very high, and the electron velocity is saturated, which is almost immune to temperature variations, as shown in Fig. 37. The drain current degradation is

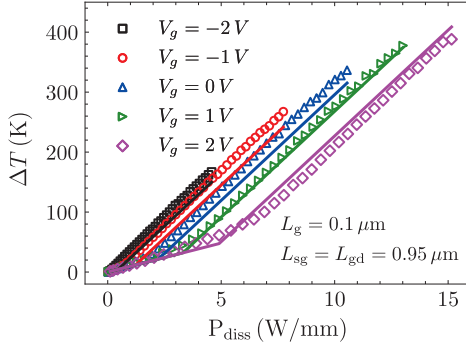


Fig. 36 Maximum temperature rises of the HEMT as a function of total power dissipation P_{diss} at different biases. The symbols are extracted from the MC simulations, and the lines are computed using the two-thermal-conductivity model based on the FEM results.

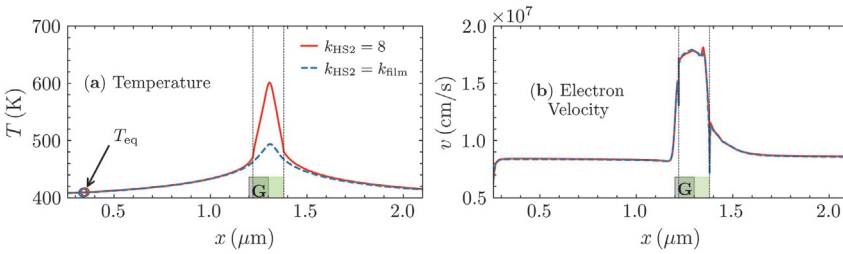


Fig. 37 (A) Channel temperature distribution and (B) electron velocity in the HEMT. In the case of $k_{\text{HS2}} = 8$, a low thermal conductivity of 8 W/m K is set in the HS2 region to account for the influence of the phonon ballistic effects on channel temperatures in TCAD simulations.

mainly dependent on the low-field source access region, which is away from the hotspot area. To estimate the self-heating-induced drain current degradation in GaN HEMTs, Chen et al. proposed an equivalent channel temperature [33]. The equivalent channel temperature is closer to the channel average temperature, instead of the maximum temperature.

4.5 Influence of full-band phonon properties

In the previous sections, empirical models were used to account for the phonon dispersion and relaxation time of different materials. However, the phonon properties of real materials can be quite complex. Taking GaN for example, there are total 12 phonon branches including three acoustic

branches and nine optical branches, each with different dispersion and scattering rates [96]. To address this, we conduct first-principles-based steady-state full-band phonon Monte Carlo (MC) simulations to investigate the thermal spreading resistance in GaN HEMTs and evaluate the accuracy of the empirical models and the proposed effective thermal conductivity model [97].

The full-band phonon properties and scattering times of wurtzite GaN are calculated using density functional theory (DFT) within the Vienna Ab initio Simulation Package (VASP) [98], while the phonon scattering rates are obtained using the ShengBTE package [99]. Fig. 38 shows the resulting phonon dispersion and scattering rates for GaN.

The results in Fig. 39 demonstrate the dimensionless total thermal resistance predicted by several methods, including full-band MC, isotropic MC with sine-shaped phonon dispersion, gray MC, and FEM with effective thermal conductivity predicted by the model proposed in the previous sections. It can be observed that the thermal resistance predicted by isotropic MC is significantly higher than that predicted by full-band MC for all geometric parameters, which can be attributed to the longer phonon MFP distributions calculated by the empirical phonon property model. However, despite the discrepancy in values, the thermal resistance predicted by isotropic MC has a similar curve shape to the full-band results, owing to the similar shape of the phonon MFP spectrum.

For gray MC, the predicted thermal resistance is very similar to the full-band predictions, indicating that the gray-medium approximation can effectively reflect the influence of phonon ballistic effects when an appropriate average phonon MFP is chosen. However, as shown in Fig. 39A, the

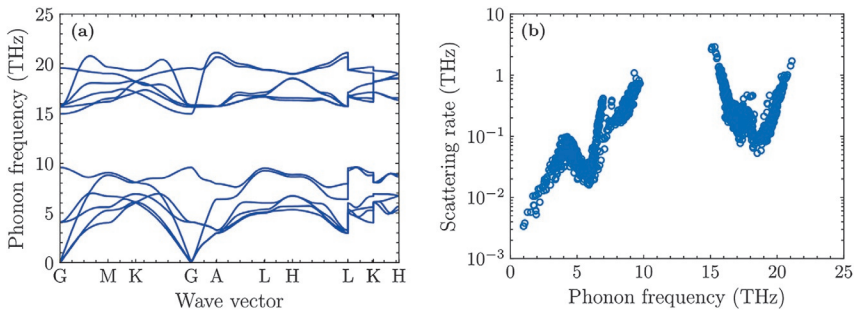


Fig. 38 First-principle-calculated phonon properties of GaN at 300 K. (A) Phonon dispersion along high symmetry points. (B) Phonon scattering rates.

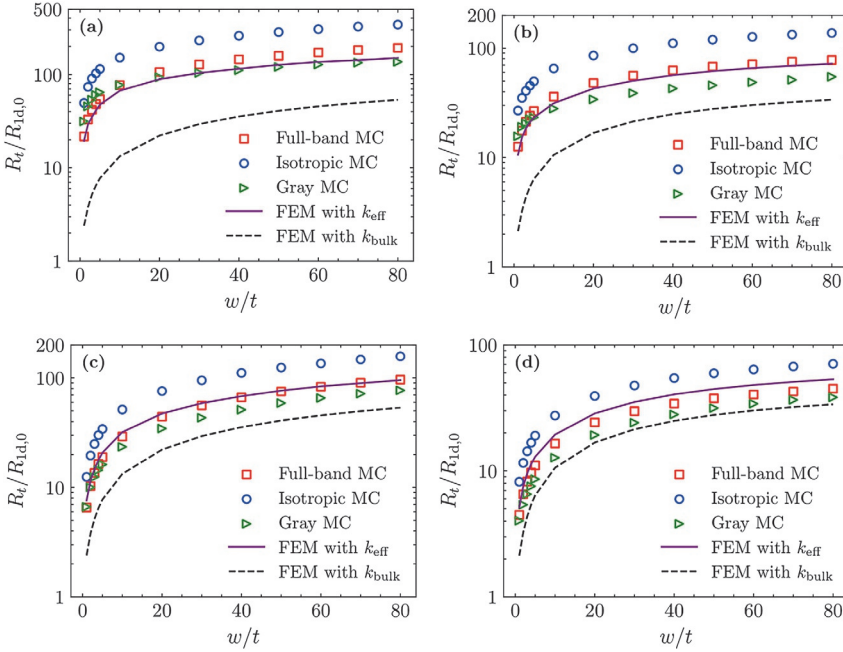
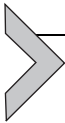


Fig. 39 Dimensionless total thermal resistance as a function of w/t with (A) $t = 0.5 \mu\text{m}$, $w_g/w = 0.005$, (B) $t = 0.5 \mu\text{m}$, $w_g/w = 0.02$, (C) $t = 3 \mu\text{m}$, $w_g/w = 0.005$, and (D) $t = 3 \mu\text{m}$, $w_g/w = 0.02$.

gray MC-predicted thermal resistance is higher when w/t is small, whereas when w/t is large, the gray MC predictions are lower. This discrepancy demonstrates the intrinsic limitation of the gray-medium approximation in reflecting the contributions of different phonon modes. The comparison between isotropic MC using empirical phonon dispersion and gray MC also suggests that combining isotropic MC with frequency-averaged first-principle-calculated phonon properties can result in more precise temperature predictions. This approach can take into account both accurate phonon properties and the influence of phonon MFP spread.

FEM with k_{eff} always predicts results in good agreement with the full-band results, indicating that the effective thermal conductivity model developed using isotropic phonon dispersion is still valid for first-principle-calculated phonon properties. This is because of the similar shape of the MFP spectrum and the weak anisotropy of GaN above room temperature.

The comparison between the different simulation methods highlights the importance of using first-principles-calculated phonon properties in device thermal simulations. Gray MC and FEM with k_{eff} both provide reasonable approximations to the full-band results, since they directly incorporate the first-principle-calculated phonon properties into the model. On the other hand, isotropic MC using empirical phonon dispersion has the lowest accuracy since the parameters are determined using the fitting of bulk thermal conductivities, rather than directly obtained from the first-principles-calculated phonon properties. Therefore, it is crucial to use first-principles calculations to obtain accurate phonon properties in device thermal simulations, regardless of the simulation technique used.



5. Self-heating effect

5.1 Self-heating effects in electronic devices

With the proliferation of electronic devices and the increasing complexity of computing tasks, the performance requirements for modern chips are growing higher and higher, leading to a gradual increase in power density. The maximum power of chips is constantly setting new benchmarks. For instance, the latest Intel Core i9 processor has a maximum thermal design power of 125 W, which is 20 W higher than the previous generation [100]. This trend can be attributed to the development of highly integrated and miniaturized technology, as well as the increasing demand for high-performance computing in diverse application scenarios. However, high power density leads to a rise in temperature, which is an inevitable problem that can reduce the reliability, performance, and life of chips. One of the major contributors to temperature rise in electronic devices is the self-heating effect, which refers to the phenomenon where the heat generated by the current flowing through the device leads to an increase in its temperature. The self-heating effect is particularly pronounced in devices with a high current density, such as power amplifiers and high-speed transistors. The characteristics of the self-heating effect vary with different devices and operating conditions. For example, in high-electron-mobility transistors (HEMTs), the heat generation mainly occurs in a small area about 100 nm width below the gate, while the total thickness of the channel and substrate layers is within hundreds of microns [19]. The transfer of heat from a small hotspot to a much larger area can cause significant near-junction spreading

resistance, which further affects chip performance and life [36]. Therefore, a correct understanding of the self-heating effect inside devices is of great significance for the near-junction heat management technology of electronic devices.

Under the action of an external electric field, electrons in the channel region inside the chip gain energy and accelerate in the channel region to form a current. This process disrupts the original equilibrium state, causing the temperature of the charge carriers to gradually increase. As the temperature rises, the electrons interact with the lattice to excite phonons and dissipate heat. Due to the higher collision frequency between electrons and optical phonons, most of the energy is transferred to high-frequency optical phonons, resulting in an accumulation of optical phonons in localized areas with significantly higher temperatures than the surrounding regions. However, the collision frequency between electrons and acoustic phonons is relatively low, so only a small amount of energy is transferred to low-frequency acoustic phonons. The contributions of optical and acoustic phonons to heat transfer differ significantly. Compared to acoustic phonons, optical phonons have a smaller group velocity and therefore contribute less to heat transfer. The main contribution to heat transfer is acoustic phonons, which receive most of the thermal energy from optical phonons and dissipate it through phonon scattering within the device and thermal conduction. Having a thorough understanding of self-heating effects is crucial for the development of effective thermal management strategies and chip design optimization. By gaining insight into the mechanisms that contribute to temperature rise inside electronic devices, researchers can develop innovative solutions that minimize heat generation and maximize heat dissipation. This can help to improve the overall performance and reliability of electronic devices, while also extending their operational life.

5.2 Impact of self-heating effects on electronic devices

Self-heating effects in electronic devices can have a detrimental impact on their reliability, performance, and lifespan. At high temperatures, the scattering between charge carriers and the lattice, impurities, and defects intensifies, resulting in a reduction in mobility. Mobility is a critical parameter that directly affects the electrical performance of the device and its decline typically leads to a decrease in the output current density [2]. Additionally, the increase in temperature leads to an increase in resistivity, which reduces the

conductivity of device [101]. With further scattering of charge carriers, more heat is generated, which may ultimately result in current collapse [102]. High-temperature hotspots generated by self-heating effects can cause material failure, leading to a reduction in the reliability of device. The failure time shortens as the temperature increases, and the Arrhenius law provides a mathematical description of this phenomenon [103]. The law states that for every 10K increase in temperature, the time to failure (TTF) is halved. Eq. (64) represents the mathematical relationship of the Arrhenius law:

$$TTF = Ce^{\frac{E_a}{k} \left[\frac{1}{T} - \frac{1}{T_0} \right]} \quad (64)$$

where E_a is the activation energy, T_0 is the room temperature, k is the Boltzmann constant, C is a constant, and T is the temperature at the time of device failure. Fitting Arrhenius' law through experimental measurements can provide a more accurate reliability calculation formula for the device. For instance, when the HEMTs working temperature increases to 250K, its lifespan sharply reduces to only about 1% of the original [104].

5.3 Simulating and modeling self-heating effects

There are three primary methods for simulating self-heating effects in electronic devices: thermal simulation, electro-thermal simulation, and electro-thermal-mechanical simulation [105]. Thermal simulation provides the most straightforward solution by solving for the temperature distribution of the device given a heat source. Electro-thermal simulation, on the other hand, takes into account the real electrical-thermal coupling in the device, providing a more accurate temperature calculation that considers the electrical performance and power dissipation of the device. Electro-thermal-mechanical simulation goes one step further by also accounting for the stress distribution inside the device, taking into consideration the effect of thermal stress. However, in most cases, electro-thermal-mechanical simulation is unnecessary and computationally expensive. Therefore, this discussion will primarily focus on the fundamental equations and heat generation models of electro-thermal simulation for electronic devices.

5.3.1 Fundamental equations

In order to accurately simulate the self-heating effect, it is necessary to first calculate the electrical properties of the device. The basic governing

equation for simulating electronic devices is the basic semiconductor equations [106] as shown in Eq. (65):

$$\begin{aligned}
 \nabla \cdot (\varepsilon \cdot \nabla \phi) &= -q \cdot (p - n + N_D - N_A) - q_{PE} - \rho_{trap} \\
 \frac{1}{q} \nabla \cdot \vec{J}_n - \frac{\partial n}{\partial t} &= R \\
 \frac{1}{q} \nabla \cdot \vec{J}_p + \frac{\partial p}{\partial t} &= -R \\
 \vec{J}_n &= q \cdot n \cdot \mu_n \cdot \vec{E} + q \cdot D_n \cdot \nabla n \\
 \vec{J}_p &= q \cdot p \cdot \mu_p \cdot \vec{E} - q \cdot D_p \cdot \nabla p
 \end{aligned} \tag{65}$$

where ε is the dielectric constant, ϕ is the electrostatic potential, q is the elementary charge, N_D and N_A are the donor and acceptor concentrations inside the semiconductor, q_{PE} is the net polarization charge, ρ_{trap} is the bulk charge density due to traps, J_n and J_p are the current densities caused by electrons and holes, n and p are the concentrations of electrons and holes, t is the time, R is the net recombination rates of electrons and holes, μ_n and μ_p are the electron and hole mobility, E is the electric field intensity, D_n and D_p are determined by the Einstein relation, as shown in Eq. (66):

$$\begin{aligned}
 D_n &= \mu_n \cdot \frac{k \cdot T}{q} \\
 D_p &= \mu_p \cdot \frac{k \cdot T}{q}
 \end{aligned} \tag{66}$$

where T is the temperature. After solving the equations of the electrical properties, we can use models to calculate the heat generation distribution inside the device.

Despite the fact that electronic devices have already entered the micro-nanoscale, in most current electro-thermal simulations, the thermal calculation part is still based on the macroscopic Fourier's law of heat conduction. Fourier's law assumes that the heat flux is proportional to the temperature gradient, as shown in Eq. (67):

$$q = -\kappa \nabla T \tag{67}$$

where q is the heat flux, κ is the thermal conductivity, and negative sign represents the direction of heat flow from high temperature to low temperature. At the macroscopic scale, thermal conductivity is a material property that is only dependent on the type of material, but at the micro- and nanoscale,

thermal conductivity exhibits size-dependent effects [28,29,107]. Solving the energy conservation equation inside the device, as shown in Eq. (68), allows for obtaining the temperature distribution inside the device:

$$\nabla \cdot (\kappa \cdot \nabla T) = -H \quad (68)$$

where H is the heat source. The calculation of H will be given in the next section. Although this thermal simulation does not take into account the true scattering process of phonons at the micro- and nanoscale, it is computationally convenient, and many simulations have shown that the results obtained from such calculations are in good agreement with experimental results [31,108]. In addition to using the heat conduction differential equation based on the Fourier law directly, many researchers have considered the effects of non-Fourier heat conduction process by using improved heat conduction differential equations such as the dual-phase-lag model [109], the Cattaneo-Christov heat conduction model [110], and the phonon hydrodynamic equation [111], etc.

The main heat carriers inside the device are phonons, and by considering the scattering process of phonons, the heat transfer process inside the device can be studied from a microscopic level. The motion of phonons follows the phonon Boltzmann transport equation (BTE), and the phonon Boltzmann transport equation under the relaxation time approximation is shown in Eq. (69):

$$\frac{\partial f}{\partial t} + v_g \cdot \nabla f = \frac{f - f_0}{\tau} + q' \quad (69)$$

where f is the phonon distribution function, v_g is the phonon group velocity, f_0 is the phonon distribution function at equilibrium, τ is the relaxation time, q' is the phonon generation term, which represents the heat generation in the device. There are several methods to solve the BTE, such as the discrete ordinate method (DOM) [112] and the Monte-Carlo (MC) method [113]. Numerous studies indicate that solving the Boltzmann equation for hot-spot temperature results in a significantly higher temperature than solving the heat conduction differential equation based on Fourier's law of heat conduction. This difference in temperature calculation can have varying effects on device performance and reliability [114,115]. To perform a comprehensive electro-thermal simulation, at least six coupled differential equations need to be solved. Therefore, electro-thermal coupling calculations are generally carried out in a two-dimensional model, supplemented by three-dimensional thermal simulations to correct the results [116].

5.3.2 Heat generation models

During the directed motion of electrons, lattice vibrations are generated by the scattering process with the lattice, which is the main process for heat generation within the device. There are many models for heat generation within the device, and the simplest one was proposed by Gaur and Navon in 1976, as shown in Eq. (70) [117]:

$$H = \left(\vec{J}_n + \vec{J}_p \right) \vec{E} \quad (70)$$

This expression is not a strict Joule heating model because it can potentially result in a negative heat source, which is because the driving force of the charge carriers in the device is not only the electric field. A more general heat generation model [118] is given as shown in Eq. (71):

$$H = \left[\frac{|\vec{J}_n|^2}{q\mu_{nn}} + \frac{|\vec{J}_p|^2}{q\mu_{pp}} \right] + qR \left[\phi_p - \phi_n + T_L(P_p - P_n) \right] - T_L \left(\vec{J}_n \nabla P_n + \vec{J}_p \nabla P_p \right) \quad (71)$$

where T_L is the lattice temperature, ϕ_n and ϕ_p are the quasi-Fermi potentials of electrons and holes, P_p and P_n are the absolute thermoelectric powers of electrons and holes, respectively. The first term $\left[\frac{|\vec{J}_n|^2}{q\mu_{nn}} + \frac{|\vec{J}_p|^2}{q\mu_{pp}} \right]$ on the right-hand side of the equation is the Joule heating, the second term $qR [\phi_p - \phi_n + T_L(P_p - P_n)]$ is the net heat generated by carrier recombination and generation process, and the third term $-T_L (\vec{J}_n \nabla P_n + \vec{J}_p \nabla P_p)$ is the heat generated by the Peltier and Joule-Thomson effects. Joule heat and recombination-generation heat basically include the main heat generation inside the device, and usually considering the first two terms can obtain good results. The heat generation process inside the device is very complex, therefore, many models have been developed, which need to be carefully considered in different situations. For the solution of the phonon Boltzmann equation, it is rewritten in energy form [119] under steady-state conditions as shown in Eq. (72):

$$\nabla \cdot (v_g \vec{s} e) = \frac{e - e_0}{\tau} + H' \quad (72)$$

where \vec{s} is the direction cosine, e is the energy density of a particular phonon, e_0 is linked to lattice temperature (T_L) through the relation $e_0 = CT_L$, where C is the phonon specific heat, H' is the heat generated inside the device. By introducing different thermal generation models, the BTE can be solved, and some articles have calculated the phonon generation term directly [120].

5.4 Typical devices and self-heating effects

5.4.1 Metal-oxide-semiconductor field-effect transistor

MOSFET is an acronym for metal-oxide-semiconductor field-effect transistor, which was invented in the early 1960s. It is one of the most important devices in modern electronics, widely used in integrated circuits, power amplifiers, switches, and other circuits. Fig. 40 shows a schematic structure of the simplest NMOS device, consisting of a gate, source, and drain, where the gate controls the conductivity of the device.

The dimensions of the MOSFET are shown in Fig. 40, with a doping concentration of the source and drain being denoted as $N_D = 1 \times 10^{20} \text{ cm}^{-3}$, and the doping concentration of the bulk material as $N_A = 1 \times 10^{16} \text{ cm}^{-3}$. Fig. 41 shows the temperature distribution at $V_{GS} = 8$ and $V_{DS} = 8$ V. The device is constructed and simulated using Silvaco TCAD. It can be observed that during MOSFET operation, the maximum temperature ($T_{max} = 392$ K) occurs in the region beneath the gate near the drain, where the current density is the highest. Due to the relatively larger conductive region beneath the MOSFET, the heat source is distributed widely, resulting in a significant increase in temperature beneath the gate.

Fig. 42 illustrates the output characteristic curves of an NMOS device at different gate voltages. It is evident that, upon considering the self-heating

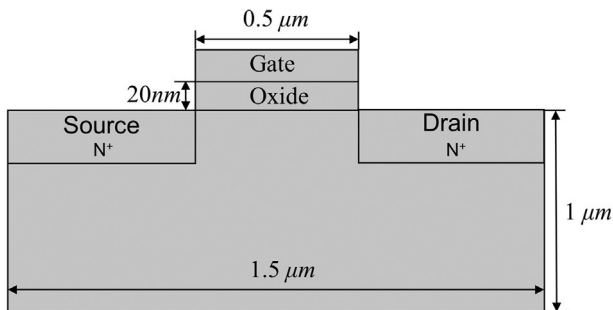


Fig. 40 Schematic diagram of the structure of an NMOS device.

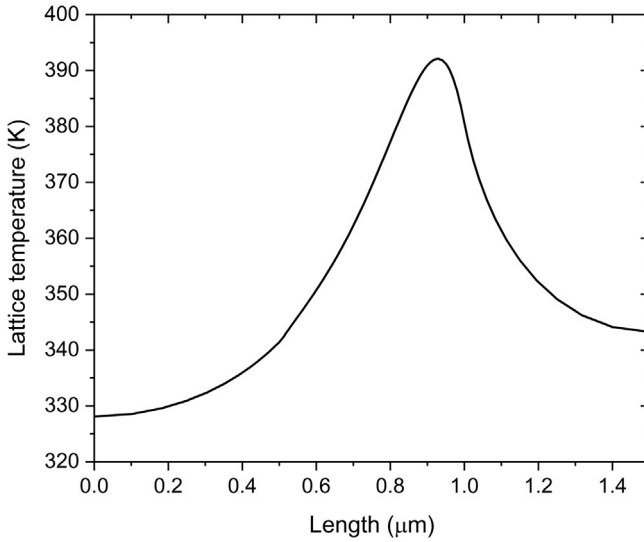


Fig. 41 The temperature distribution of an NMOS at $V_{GS} = 8$ and $V_{DS} = 8$ V.

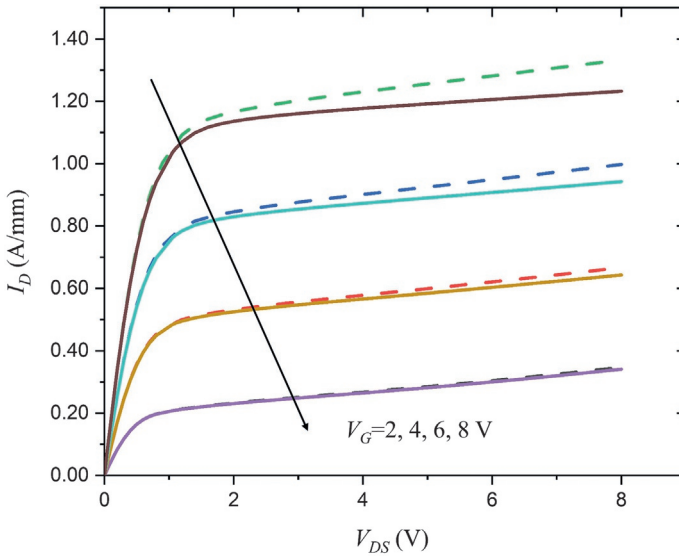


Fig. 42 The output characteristic curves of NMOS device at different gate voltages. The dotted line depicts the result without considering the self-heating effect, and the solid line depicts the result with considering the self-heating effect.

effect, the current density of the NMOS device reduces, and the effect becomes more pronounced with an increase in the gate voltage. This is because at high temperatures, carrier scattering becomes stronger, leading to a reduction in carrier mobility. Carrier mobility directly affects the conductivity of the device, and hence, the current density at high temperatures reduces. With the increase in the gate voltage, the electron concentration in the depletion layer under the gate rises, enhancing the conductivity. However, the increase in current density further strengthens the self-heating effect, leading to a higher temperature in the region and a greater reduction in carrier mobility. For accurate device simulation, it is essential to comprehensively consider the electro-thermal coupling process inside the device. While NMOS is the simplest MOSFET, more commonly used MOSFETs include CMOS, VDMOS, and SOI-MOS, and their electro-thermal simulations have been extensively reported in the literature [111,121,122].

5.4.2 High electron mobility transistors

High electron mobility transistors (HEMTs) are widely used in low noise amplifiers and high-frequency power amplifiers in radio frequency (RF) and microwave circuits due to their excellent properties such as high mobility and low power consumption. HEMTs are a multi-layer thin film structure, as shown in Fig. 32 [38]. Unlike MOSFETs, the strong spontaneous and piezoelectric polarization of GaN and AlGaIn leads to the formation of a two-dimensional electron gas (2DEG) at the heterojunction interface. The 2DEG is very thin, typically in the range of 1–2 nm, and has a high mobility, making HEMTs suitable for important applications in wireless communications, radar, and wireless television.

Fig. 34 shows the heat generation distribution of GaN HEMTs under different biases [38]. Unlike MOSFETs, HEMTs have a 2D electron gas as conductive channel, which leads to a more concentrated heat generation. The majority of the heat is distributed near the conductive channel at the top of GaN layer, which is located under the gate and near the drain region. In addition, the heat generation in HEMTs is bias-dependent [31,94]. At low biases, the electric field is relatively uniform, resulting in lower and more evenly distributed heat generation. However, at high biases, the local electric field is stronger, causing the heat generation to be more concentrated near the 2D electron gas under the gate near the drain.

Fig. 43 shows the output characteristic curves of HEMT under different gate voltages [38]. As the gate voltage increases, the device performance deteriorates more significantly due to the self-heating effect in HEMT,

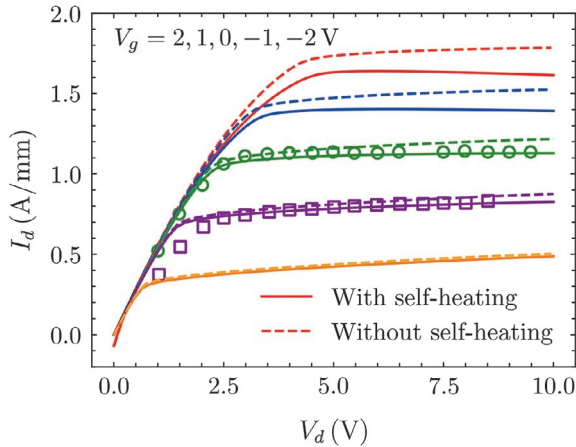


Fig. 43 The output characteristic curves of HEMT device at different gate voltages. The dotted line shows the result without considering the self-heating effect, and the solid line depicts the result with considering the self-heating effect.

which is also caused by the increase in current density and hence the increase in heat generation. Furthermore, at the same gate voltage, the device performance changes more drastically at high drain–source voltages, indicating the influence of electric field on heat generation in the model. While the drift velocity of carriers may saturate under high electric fields, the strengthening of the electric field can still increase carrier and lattice scattering, which in turn enhances the self-heating effect in the device [123].

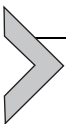
5.5 Measurement methods for self-heating effect

During the design process of electronic devices, simulation and theoretical calculations can provide predictions for the self-heating effect and performance of device. However, experimental measurements are necessary to determine the actual self-heating effect of the device. The most common method is to use a thermocouple to measure the surface temperature of the device. However, contact measurement methods may damage the device surface and have low accuracy, limiting their capability to measure only the surface temperature field [124]. Infrared thermography is a non-contact method that enables real-time monitoring of temperature changes on the device’s surface and is suitable for large-scale device detection. However, it has limited resolution and cannot measure the internal temperature distribution of the device [125]. Micro-Raman thermometry, on the other hand, measures the temperature distribution by analyzing the Raman spectra on the

device's surface. It is more accurate than infrared thermometry and can operate in high-temperature environments. However, it can also only measure surface temperature [126]. To measure the internal temperature distribution of the device, the time-domain thermoreflectance imaging (TDTR) method is widely used. It generates a thermal pulse on the device's surface using a femtosecond laser and obtains the device thermal performance through the propagation of thermal waves within the device. TDTR provides high accuracy and resolution but requires expensive equipment and is only suitable for devices with uniform thermal diffusivity and heat capacity [127–129].

5.6 Management methods for self-heating effect

The self-heating effect can reduce the performance of a device and affect its reliability and lifespan. Managing and reducing the self-heating effect inside a device is crucial for the development of chips. The control of the self-heating effect can be achieved from two directions: inside and outside the device. Several methods can be employed for internal control of the device to minimize self-heating effects. These include using high thermal conductivity substrate materials such as SiC [130] and diamond [131], utilizing high thermal conductivity top heat dissipation materials like monocrystalline diamond [132] and few-layer graphene [133], reducing the thermal boundary resistance between different materials inside the device [134,135], and optimizing the device design to change electric field and current distribution [108,136,137]. These approaches can help to improve device performance and reliability by reducing local hotspots and extending operational lifespan. On the other hand, the external control of the device can be improved through better packaging and different cooling methods. Improved packaging can reduce the self-heating effect by providing better isolation and reducing heat accumulation inside the device [138–140]. Different cooling methods, such as microchannel cooling [141–143], can enhance heat dissipation outside the device, thereby reducing the self-heating effect. In summary, managing and reducing the self-heating effect of a device is critical for improving its performance, reliability, and lifespan. It can be achieved by implementing various techniques from both inside and outside the device.



6. Conclusion

The present chapter gives a comprehensive introduction and description of the progress in the near-junction thermal management of electronic

devices, by reviewing the study on ballistic heat conduction in nanostructures, thermal conductivity of nanostructures, thermal spreading resistance and self-heating effect in electronic devices. For the study on ballistic heat conduction in nanostructures, the boundary temperature jump (BTJ) and boundary heat flux slip (BHFS) of ballistic heat conduction based on the BTE are mainly discussed. The BTJ arises at the boundary where phonons and heat sinks cannot reach temperature equilibrium due to the ballistic effect. And the BHFS occurs when the phonon-boundary scattering is significant due to the greatly increased boundary/interface density in nanostructures, which will alter the traveling direction of phonons. A set of predictive models for the BTJs and the BHFS are developed in various cases. Besides, the phonon property mismatch at the interface alone can lead to the changes in the heat flux distribution for a nanofilm on a substrate.

For the thermal conductivity of nanostructures, multiple factors are found to have significant effects on the lattice thermal conductivity of GaN, including characteristic size and geometry, heating conditions, interfacial effects, stress, and electric fields. Characteristic size and geometry of a nanostructure can be the leading factors that affect the effective thermal conductivity. A BTE-based thermal conductivity model, able to consider multiple constraints, is introduced. Then, the effect of heating conditions on the effective thermal conductivity is discussed based on both the BTE-based models and phonon MC simulations. Moreover, the two-way manipulation of effective thermal conductivity through interfacial effect is presented. Lastly, the influence of external fields is examined. Both stress and electric fields have a significant effect on the lattice thermal conductivity of GaN.

Thermal spreading resistance in electronic devices regarding ballistic-diffusive transport is particularly discussed in GaN HEMTs, using phonon MC simulation accounting for gray model, phonon dispersion, bias-dependent heat source and full-band phonon properties successively. It is revealed that the phonon ballistic effects can substantially augment thermal spreading resistance. And the bias-dependent heat generation can markedly impact both thermal spreading resistance and phonon ballistic effects. One thermal resistance model considering phonon dispersion and one two-thermal-conductivity model considering the bias-dependent non-Fourier thermal spreading resistance in GaN HEMTs are proposed. With the use of first-principle-calculated phonon properties, the importance of incorporating first-principles-calculated phonon properties in device thermal simulations is confirmed.

For the self-heating effect in electronic devices, the electro-thermal simulation is usually taken to model the self-heating effects and predict the temperature field in the devices and reveal the impact of self-heating on electronics devices. The self-heating effect is found to vary with electronics and operation condition. The main heat generation, the Joule heat, is dependent on the current density and electric field distribution. Generally, there are two approaches to control self-heating, i.e., internal and external methods. Furthermore, the self-heating effect can be explored thoroughly through combining simulation and experiment.

Acknowledgments

The present work acknowledges the figures from the Journals, including International Journal of Heat and Mass Transfer, International Journal of Thermal Sciences, IEEE Transactions on Electron Devices, Journal of Applied Physics, and Nanoscale and Microscale Thermophysical Engineering. This work was supported by the National Natural Science Foundation of China (NNSFC) (Nos. 51825601 and U20A20301).

References

- [1] E.A. Jones, F. Wang, B. Ozpineci, Application-based review of GaN HFETs, in: 2014 IEEE Workshop on Wide Bandgap Power Devices and Applications, IEEE, 2014, pp. 24–29.
- [2] U.K. Mishra, P. Parikh, Y.-F. Wu, AlGaIn/GaN HEMTs—an overview of device operation and applications, *Proc. IEEE* 90 (6) (2002) 1022–1031.
- [3] F. Roccaforte, P. Fiorenza, G. Greco, R.L. Nigro, F. Giannazzo, F. Iucolano, M. Saggio, Emerging trends in wide band gap semiconductors (SiC and GaN) technology for power devices, *Microelectron. Eng.* 187 (2018) 66–77.
- [4] J.B. Varley, B. Shen, M. Higashiwaki, *Wide Bandgap Semiconductor Materials and Devices*, AIP Publishing LLC, 2022, p. 230401.
- [5] M. Haziq, S. Falina, A.A. Manaf, H. Kawarada, M. Syamsul, Challenges and opportunities for high-power and high-frequency AlGaIn/GaN high-electron-mobility transistor (HEMT) applications: a review, *Micromachines* 13 (12) (2022) 2133.
- [6] M. Meneghini, C. De Santi, I. Abid, M. Buffolo, M. Cioni, R.A. Khadar, L. Nela, N. Zagni, A. Chini, F. Medjdoub, GaN-based power devices: physics, reliability, and perspectives, *J. Appl. Phys.* 130 (18) (2021) 181101.
- [7] B. Wang, M. Xiao, Z. Zhang, Y. Wang, Y. Qin, Q. Song, G.-Q. Lu, K. Ngo, Y. Zhang, Chip size minimization for wide and ultrawide bandgap power devices, *IEEE Trans. Electron Devices* 70 (2) (2023) 633–639.
- [8] Q. Hao, H. Zhao, Y. Xiao, M.B. Kronenfeld, Electrothermal studies of GaN-based high electron mobility transistors with improved thermal designs, *Int. J. Heat Mass Transf.* 116 (2018) 496–506.
- [9] M. Rosker, C. Bozada, H. Dietrich, A. Hung, D. Via, S. Binari, E. Vivierios, E. Cohen, J. Hodiak, The DARPA wide band gap semiconductors for RF applications (WBGs-RF) program: phase II results, in: International Conference on Compound Semiconductor Manufacturing Technology, 2009, pp. 1–4.
- [10] H. Chen, N. Tang, Z. Zuo, Improvement and reduction of self-heating effect in AlGaIn/GaN HEMT devices, *J. Sensors* 2022 (2022) 1–10.

- [11] V. Lakshminarayanan, N. Sriraam, The effect of temperature on the reliability of electronic components, in: 2014 IEEE International Conference On Electronics, Computing And Communication Technologies (CONECCT), 2014, IEEE, 2014, pp. 1–6.
- [12] Z. Zhang, X. Wang, Y. Yan, A review of the state-of-the-art in electronic cooling, *e-Prime—Adv. Electr. Eng. Electron. Energy* 1 (2021) 100009.
- [13] Y. Qin, B. Albano, J. Spencer, J.S. Lundh, B. Wang, C. Buttay, M.J. Tadjer, C. DiMarino, Y. Zhang, Thermal management and packaging of wide and ultra-wide bandgap power devices: a review and perspective, *J. Phys. D Appl. Phys.* (2023).
- [14] C. Chan, E. Siqueiros, J. Ling-Chin, M. Royapoor, A. Roskilly, Heat utilisation technologies: a critical review of heat pipes, *Renew. Sust. Energy. Rev.* 50 (2015) 615–627.
- [15] Y. Li, L. Gong, B. Ding, M. Xu, Y. Joshi, Thermal management of power electronics with liquid cooled metal foam heat sink, *Int. J. Therm. Sci.* 163 (2021) 106796.
- [16] Y. Won, J. Cho, D. Agonafer, M. Asheghi, K.E. Goodson, Cooling limits for GaN HEMT technology, in: 2013 IEEE Compound Semiconductor Integrated Circuit Symposium (CSICS), 2013, IEEE, 2013, pp. 1–5.
- [17] C. Zhang, J.W. Palko, M.T. Barako, M. Asheghi, K.E. Goodson, Design and optimization of well-ordered microporous copper structure for high heat flux cooling applications, *Int. J. Heat Mass Transf.* 173 (2021) 121241.
- [18] A.C. Kheirabadi, D. Groulx, Cooling of server electronics: a design review of existing technology, *Appl. Therm. Eng.* 105 (2016) 622–638.
- [19] J. Cho, Z. Li, M. Asheghi, K.E. Goodson, Near-junction thermal management: thermal conduction in gallium nitride composite substrates, *Annu. Rev. Heat Transf.* 18 (2015).
- [20] D.-S. Tang, B.-Y. Cao, Phonon thermal transport and its tunability in GaN for near-junction thermal management of electronics: a review, *Int. J. Heat Mass Transf.* 200 (2023) 123497.
- [21] B. Chatterjee, D. Ji, A. Agarwal, S.H. Chan, S. Chowdhury, S. Choi, Electro-thermal investigation of GaN vertical trench MOSFETs, *IEEE Electr. Device Lett.* 42 (5) (2021) 723–726.
- [22] B. Chatterjee, K. Zeng, C.D. Nordquist, U. Singiseti, S. Choi, Device-level thermal management of gallium oxide field-effect transistors, *IEEE Trans. Compon. Packag. Manuf. Technol.* 9 (12) (2019) 2352–2365.
- [23] S. Choi, S. Graham, S. Chowdhury, E.R. Heller, M.J. Tadjer, G. Moreno, S. Narumanchi, A perspective on the electro-thermal co-design of ultra-wide bandgap lateral devices, *Appl. Phys. Lett.* 119 (17) (2021) 170501.
- [24] R.J. Warzoha, A.A. Wilson, B.F. Donovan, N. Donmezer, A. Giri, P.E. Hopkins, S. Choi, D. Pahinkar, J. Shi, S. Graham, Applications and impacts of nanoscale thermal transport in electronics packaging, *J. Electron. Packag.* 143 (2) (2021).
- [25] H. Bao, J. Chen, X. Gu, B. Cao, A review of simulation methods in micro/nanoscale heat conduction, *ES Energy Environ.* 1 (39) (2018) 16–55.
- [26] G. Chen, Non-Fourier phonon heat conduction at the microscale and nanoscale, *Nat. Rev. Phys.* 3 (8) (2021) 555–569.
- [27] Y.-C. Hua, B.-Y. Cao, Slip boundary conditions in ballistic-diffusive heat transport in nanostructures, *Nanoscale Microscale Thermophys. Eng.* 21 (3) (2017) 159–176.
- [28] Y.-C. Hua, B.-Y. Cao, Phonon ballistic-diffusive heat conduction in silicon nanofilms by Monte Carlo simulations, *Int. J. Heat Mass Transf.* 78 (2014) 755–759.
- [29] Y.-C. Hua, B.-Y. Cao, The effective thermal conductivity of ballistic-diffusive heat conduction in nanostructures with internal heat source, *Int. J. Heat Mass Transf.* 92 (2016) 995–1003.
- [30] Y.-C. Hua, H.-L. Li, B.-Y. Cao, Thermal spreading resistance in ballistic-diffusive regime for GaN HEMTs, *IEEE Trans. Electron Devices* 66 (8) (2019) 3296–3301.

- [31] X. Chen, S. Boumaiza, L. Wei, Self-heating and equivalent channel temperature in short gate length GaN HEMTs, *IEEE Trans. Electron Devices* 66 (9) (2019) 3748–3755.
- [32] X. Chen, S. Boumaiza, L. Wei, Modeling bias dependence of self-heating in GaN HEMTs using two heat sources, *IEEE Trans. Electron Devices* 67 (8) (2020) 3082–3087.
- [33] X. Chen, S. Boumaiza, L. Wei, Self-heating in short-channel GaN HEMTs: maximum channel temperature and equivalent channel temperature, in: *2022 6th IEEE Electron Devices Technology & Manufacturing Conference (EDTM)*, IEEE, 2022, pp. 351–353.
- [34] Y. Muzychka, J. Culham, M. Yovanovich, Thermal spreading resistance of eccentric heat sources on rectangular flux channels, *J. Electron. Packag.* 125 (2) (2003) 178–185.
- [35] Y.S. Muzychka, Thermal spreading resistance in compound orthotropic circular disks and rectangular channels with interfacial resistance, in: *44th AIAA Thermophysics Conference*, 2013, p. 2641.
- [36] M. Razavi, Y. Muzychka, S. Kocabiyik, Review of advances in thermal spreading resistance problems, *J. Thermophys. Heat Transf.* 30 (4) (2016) 863–879.
- [37] Q. Hao, H. Zhao, Y. Xiao, A hybrid simulation technique for electrothermal studies of two-dimensional GaN-on-SiC high electron mobility transistors, *J. Appl. Phys.* 121 (20) (2017) 204501.
- [38] Y. Shen, X.-S. Chen, Y.-C. Hua, H.-L. Li, L. Wei, B.-Y. Cao, Bias dependence of non-Fourier heat spreading in GaN HEMTs, *IEEE Trans. Electron Devices* 70 (2) (2022) 409–417.
- [39] B. Vermeersch, R. Rodriguez, A. Sibaja-Hernandez, A. Vais, S. Yadav, B. Parvais, N. Collaert, Thermal modelling of GaN & InP RF devices with intrinsic account for nanoscale transport effects, in: *2022 International Electron Devices Meeting (IEDM)*, IEEE, 2022, pp. 15.13.11–15.13.14.
- [40] J.M. Ziman, *Electrons and Phonons*, Oxford University Press, London, 1960.
- [41] G. Chen, *Nanoscale Energy Transport and Conversion: A Parallel Treatment of Electrons, Molecules, Phonons, and Photons*, Oxford University Press, New York, 2005.
- [42] J. Maassen, M. Lundstrom, Steady-state heat transport: ballistic-to-diffusive with Fourier's law, *J. Appl. Phys.* 117 (3) (2015) 035104.
- [43] R. Wilson, D.G. Cahill, Anisotropic failure of Fourier theory in time-domain thermoreflectance experiments, *Nat. Commun.* 5 (1) (2014) 5075.
- [44] J. Kaiser, T. Feng, J. Maassen, X. Wang, X. Ruan, M. Lundstrom, Thermal transport at the nanoscale: a Fourier's law vs. phonon Boltzmann equation study, *J. Appl. Phys.* 121 (4) (2017) 044302.
- [45] D.P. Sellan, J.E. Turney, A.J.H. McGaughey, C.H. Amon, Cross-plane phonon transport in thin films, *J. Appl. Phys.* 108 (11) (2010) 113524.
- [46] J.E. Turney, A.J.H. McGaughey, C.H. Amon, In-plane phonon transport in thin films, *J. Appl. Phys.* 107 (2) (2010) 024317.
- [47] Y.-C. Hua, B.-Y. Cao, Ballistic-diffusive heat conduction in multiply-constrained nanostructures, *Int. J. Therm. Sci.* 101 (2016) 126–132.
- [48] H.-L. Li, Y.-C. Hua, B.-Y. Cao, A hybrid phonon Monte Carlo-diffusion method for ballistic-diffusive heat conduction in nano-and micro-structures, *Int. J. Heat Mass Transf.* 127 (2018) 1014–1022.
- [49] H.-L. Li, J. Shiomi, B.-Y. Cao, Ballistic-diffusive heat conduction in thin films by phonon Monte Carlo method: gray medium approximation versus phonon dispersion, *J. Heat Transf.* 142 (11) (2020).
- [50] Y. Shen, Y.-C. Hua, H.-L. Li, S. Sobolev, B.-Y. Cao, Spectral thermal spreading resistance of wide-bandgap semiconductors in ballistic-diffusive regime, *IEEE Trans. Electron Devices* 69 (6) (2022) 3047–3054.

- [51] A. Majumdar, Microscale heat conduction in dielectric thin films, *J. Heat Transf.* 115 (1) (1993) 7–16.
- [52] Z. Rieder, J. Lebowitz, E. Lieb, Properties of a harmonic crystal in a stationary non-equilibrium state, in: *Statistical Mechanics: Selecta of Elliott H. Lieb*, Springer-Verlag, Berlin Heidelberg, New York, 2004, pp. 373–378.
- [53] F. Alvarez, D. Jou, Boundary conditions and evolution of ballistic heat transport, *J. Heat Transf.* 132 (1) (2010) 012404.
- [54] Y.-C. Hua, B.-Y. Cao, An efficient two-step Monte Carlo method for heat conduction in nanostructures, *J. Comput. Phys.* 342 (2017) 253–266.
- [55] G. Chen, Thermal conductivity and ballistic-phonon transport in the cross-plane direction of superlattices, *Phys. Rev. B* 57 (23) (1998) 14958.
- [56] A. Sellitto, F. Alvarez, D. Jou, Temperature dependence of boundary conditions in phonon hydrodynamics of smooth and rough nanowires, *J. Appl. Phys.* 107 (11) (2010) 114312.
- [57] Z.-X. Guo, D. Zhang, X.-G. Gong, Manipulating thermal conductivity through substrate coupling, *Phys. Rev. B* 84 (7) (2011) 075470.
- [58] J.H. Seol, I. Jo, A.L. Moore, L. Lindsay, Z.H. Aitken, M.T. Pettes, X. Li, Z. Yao, R. Huang, D. Broido, Two-dimensional phonon transport in supported graphene, *Science* 328 (5975) (2010) 213–216.
- [59] R. Peterson, Direct simulation of phonon-mediated heat transfer in a Debye crystal, *J. Heat Transf.* 116 (1994) 815–822.
- [60] R. Prasher, Acoustic mismatch model for thermal contact resistance of van der Waals contacts, *Appl. Phys. Lett.* 94 (4) (2009) 041905.
- [61] D. Li, Y. Wu, P. Kim, L. Shi, P. Yang, A. Majumdar, Thermal conductivity of individual silicon nanowires, *Appl. Phys. Lett.* 83 (14) (2003) 2934–2936.
- [62] A.I. Hochbaum, R. Chen, R.D. Delgado, W. Liang, E.C. Garnett, M. Najarian, A. Majumdar, P. Yang, Enhanced thermoelectric performance of rough silicon nanowires, *Nature* 451 (7175) (2008) 163–167.
- [63] L. Liu, M. Asheghi, Phonon-boundary scattering in ultrathin single-crystal silicon layers, *Appl. Phys. Lett.* 84 (19) (2004) 3819–3821.
- [64] R. Chen, A.I. Hochbaum, P. Murphy, J. Moore, P. Yang, A. Majumdar, Thermal conductance of thin silicon nanowires, *Phys. Rev. Lett.* 101 (10) (2008) 105501.
- [65] T.-K. Hsiao, H.-K. Chang, S.-C. Liou, M.-W. Chu, S.-C. Lee, C.-W. Chang, Observation of room-temperature ballistic thermal conduction persisting over 8.3 μm in SiGe nanowires, *Nat. Nanotechnol.* 8 (7) (2013) 534–538.
- [66] J.A. Johnson, A. Maznev, J. Cuffe, J.K. Eliason, A.J. Minnich, T. Kehoe, C.M.S. Torres, G. Chen, K.A. Nelson, Direct measurement of room-temperature non-diffusive thermal transport over micron distances in a silicon membrane, *Phys. Rev. Lett.* 110 (2) (2013) 025901.
- [67] X. Lü, W. Shen, J. Chu, Size effect on the thermal conductivity of nanowires, *J. Appl. Phys.* 91 (3) (2002) 1542–1552.
- [68] Y. Dong, B. Cao, Z. Guo, Thermomass Theory: A Mechanical Pathway to Analyze Anomalous Heat Conduction in Nanomaterials, in: *Nanomechanics*, IntechOpen, London, 2017, pp. 69–87.
- [69] J. Yang, Y. Yang, S.W. Waltermire, X. Wu, H. Zhang, T. Gutu, Y. Jiang, Y. Chen, A.A. Zinn, R. Prasher, Enhanced and switchable nanoscale thermal conduction due to van der Waals interfaces, *Nat. Nanotechnol.* 7 (2) (2012) 91–95.
- [70] W. Chen, J. Yang, Z. Wei, C. Liu, K. Bi, D. Xu, D. Li, Y. Chen, Effects of interfacial roughness on phonon transport in bilayer silicon thin films, *Phys. Rev. B* 92 (13) (2015) 134113.
- [71] R. Su, Z. Yuan, J. Wang, Z. Zheng, Enhanced energy transport owing to nonlinear interface interaction, *Sci. Rep.* 6 (1) (2016) 1–12.

- [72] T. Sun, J. Wang, W. Kang, Van der Waals interaction-tuned heat transfer in nanostructures, *Nanoscale* 5 (1) (2013) 128–133.
- [73] X. Zhang, H. Bao, M. Hu, Bilateral substrate effect on the thermal conductivity of two-dimensional silicon, *Nanoscale* 7 (14) (2015) 6014–6022.
- [74] Z.-Y. Ong, E. Pop, Effect of substrate modes on thermal transport in supported graphene, *Phys. Rev. B* 84 (7) (2011) 075471.
- [75] B. Qiu, X. Ruan, Reduction of spectral phonon relaxation times from suspended to supported graphene, *Appl. Phys. Lett.* 100 (19) (2012) 193101.
- [76] Y.-C. Hua, B.-Y. Cao, Interface-based two-way tuning of the in-plane thermal transport in nanofilms, *J. Appl. Phys.* 123 (11) (2018) 114304.
- [77] D. Li, A.J. McGaughey, Phonon dynamics at surfaces and interfaces and its implications in energy transport in nanostructured materials—an opinion paper, *Nanoscale Microscale Thermophys. Eng.* 19 (2) (2015) 166–182.
- [78] J.P. Ibbetson, P.T. Fini, K.D. Ness, S.P. DenBaars, J.S. Speck, U.K. Mishra, Polarization effects, surface states, and the source of electrons in AlGaIn/GaN heterostructure field effect transistors, *Appl. Phys. Lett.* 77 (2) (2000) 250–252.
- [79] M.K. Öztürk, H. Altuntaş, S. Çörekçi, Y. Hongbo, S. Özçelik, E. Özbay, Strain–stress analysis of AlGaIn/GaN heterostructures with and without an AlN buffer and interlayer, *Strain* 47 (s2) (2011) 19–27.
- [80] D.-S. Tang, B.-Y. Cao, Phonon thermal transport properties of GaN with symmetry-breaking and lattice deformation induced by the electric field, *Int. J. Heat Mass Transf.* 179 (2021) 121659.
- [81] D.-S. Tang, G.-Z. Qin, M. Hu, B.-Y. Cao, Thermal transport properties of GaN with biaxial strain and electron-phonon coupling, *J. Appl. Phys.* 127 (3) (2020) 035102.
- [82] N.A. Mahadik, S.B. Qadri, M.V. Rao, Surface strain and its impact on the electrical resistivity of GaN channel in AlGaIn/GaN high electron mobility transistor, *Appl. Phys. Lett.* 93 (22) (2008) 222106.
- [83] C. Liu, Y. Chen, C. Dames, Electric-field-controlled thermal switch in ferroelectric materials using first-principles calculations and domain-wall engineering, *Phys. Rev. Appl.* 11 (4) (2019) 044002.
- [84] X. Wang, D. Vanderbilt, First-principles perturbative computation of phonon properties of insulators in finite electric fields, *Phys. Rev. B* 74 (5) (2006) 054304.
- [85] I. Souza, J. Íñiguez, D. Vanderbilt, First-principles approach to insulators in finite electric fields, *Phys. Rev. Lett.* 89 (11) (2002) 117602.
- [86] Y. Quan, S.-Y. Yue, B. Liao, Electric field effect on the thermal conductivity of wurtzite GaN, *Appl. Phys. Lett.* 118 (16) (2021) 162110.
- [87] A. Gholami, M. Bahrami, Thermal spreading resistance inside anisotropic plates with arbitrarily located hotspots, *J. Thermophys. Heat Transf.* 28 (4) (2014) 679–686.
- [88] Y.S. Muzychka, K.R. Bagnall, E.N. Wang, Thermal spreading resistance and heat source temperature in compound orthotropic systems with interfacial resistance, *IEEE Trans. Compon. Packag. Manuf. Technol.* 3 (11) (2013) 1826–1841.
- [89] A. Darwish, A.J. Bayba, H.A. Hung, Channel temperature analysis of GaN HEMTs with nonlinear thermal conductivity, *IEEE Trans. Electron Devices* 62 (3) (2015) 840–846.
- [90] E. Ziade, J. Yang, G. Brummer, D. Nothorn, T. Moustakas, A.J. Schmidt, Thickness dependent thermal conductivity of gallium nitride, *Appl. Phys. Lett.* 110 (3) (2017) 031903.
- [91] J. Ma, X. Wang, B. Huang, X. Luo, Effects of point defects and dislocations on spectral phonon transport properties of wurtzite GaN, *J. Appl. Phys.* 114 (7) (2013) 074311.
- [92] J.P. Freedman, J.H. Leach, E.A. Preble, Z. Sitar, R.F. Davis, J.A. Malen, Universal phonon mean free path spectra in crystalline semiconductors at high temperature, *Sci. Rep.* 3 (1) (2013) 2963.

- [93] H.-L. Li, Y. Shen, Y.-C. Hua, S. Sobolev, B.-Y. Cao, Hybrid Monte Carlo-diffusion studies of modeling self-heating in ballistic-diffusive regime for gallium nitride HEMTs, *J. Electron. Packag.* 145 (1) (2023) 011203.
- [94] O. Odabaşı, M.Ö. Akar, B. Bütün, E. Özbay, Improved T MAX estimation in GaN HEMTs using an equivalent hot point approximation, *IEEE Trans. Electron Devices* 67 (4) (2020) 1553–1559.
- [95] W. Jatal, U. Baumann, K. Tonisch, F. Schwierz, J. Pezoldt, High-frequency performance of GaN high-electron mobility transistors on 3C-SiC/Si substrates with Au-free ohmic contacts, *IEEE Electr. Device Lett.* 36 (2) (2014) 123–125.
- [96] R. Wu, R. Hu, X. Luo, First-principle-based full-dispersion Monte Carlo simulation of the anisotropic phonon transport in the wurtzite GaN thin film, *J. Appl. Phys.* 119 (14) (2016) 145706.
- [97] Y. Shen, H.-A. Yang, B.-Y. Cao, Near-junction phonon thermal spreading in GaN HEMTs: a comparative study of simulation techniques by full-band phonon Monte Carlo method, *Int. J. Heat Mass Transf.* 211 (2023) 124284.
- [98] J. Hafner, Ab-initio simulations of materials using VASP: density-functional theory and beyond, *J. Comput. Chem.* 29 (13) (2008) 2044–2078.
- [99] W. Li, J. Carrete, N.A. Katcho, N. Mingo, ShengBTE: a solver of the Boltzmann transport equation for phonons, *Comput. Phys. Commun.* 185 (6) (2014) 1747–1758.
- [100] W.-Y. Chen, X.-L. Shi, J. Zou, Z.-G. Chen, Thermoelectric coolers for on-chip thermal management: materials, design, and optimization, *Mater. Sci. Eng. R-Rep.* 151 (2022) 100700.
- [101] G. Mahan, B. Sales, Thermoelectric materials: new approaches to an old problem, *Phys. Today* 50 (3) (1997) 42–47.
- [102] T. Mizutani, Y. Ohno, M. Akita, S. Kishimoto, K. Maezawa, A study on current collapse in AlGaIn/GaN HEMTs induced by bias stress, *IEEE Trans. Electron Devices* 50 (10) (2003) 2015–2020.
- [103] S.R. Bahl, F. Baltazar, Y. Xie, A generalized approach to determine the switching lifetime of a GaN FET, in: 2020 IEEE International Reliability Physics Symposium (IRPS), IEEE, 2020, pp. 1–6.
- [104] R. Lossy, H. Blanck, J. Würfl, Reliability studies on GaN HEMTs with sputtered Iridium gate module, *Microelectron. Reliab.* 52 (9–10) (2012) 2144–2148.
- [105] M. Ancona, Modeling of thermal phenomena in GaN devices, in: *Thermal Management of Gallium Nitride Electronics*, Woodhead Publishing, Massachusetts, Oxford, 2022, pp. 165–184.
- [106] S. Selberherr, *Analysis and Simulation of Semiconductor Devices*, Springer Science & Business Media, New York, 1984.
- [107] Y. Dong, B.-Y. Cao, Z.-Y. Guo, Size dependent thermal conductivity of Si nanosystems based on phonon gas dynamics, *Phys. E* 56 (2014) 256–262.
- [108] Y. Zhang, M. Sun, Z. Liu, D. Piedra, H.-S. Lee, F. Gao, T. Fujishima, T. Palacios, Electrothermal simulation and thermal performance study of GaN vertical and lateral power transistors, *IEEE Trans. Electron Devices* 60 (7) (2013) 2224–2230.
- [109] J. Ghazanfarian, Z. Shomali, Investigation of dual-phase-lag heat conduction model in a nanoscale metal-oxide-semiconductor field-effect transistor, *Int. J. Heat Mass Transf.* 55 (21–22) (2012) 6231–6237.
- [110] B. Vermeersch, G. De Mey, Non-Fourier thermal conduction in nano-scaled electronic structures, *Analog Integr. Circuits Process.* 55 (2008) 197–204.
- [111] H. Rezgüi, F. Nasri, A.B.H. Ali, A.A. Guizani, Analysis of the ultrafast transient heat transport in sub 7-nm SOI FinFETs technology nodes using phonon hydrodynamic equation, *IEEE Trans. Electron Devices* 68 (1) (2020) 10–16.
- [112] J. Murthy, S. Mathur, Computation of sub-micron thermal transport using an unstructured finite volume method, *J. Heat Transf.* 124 (6) (2002) 1176–1181.

- [113] J.-P.M. Péraud, C.D. Landon, N.G. Hadjiconstantinou, Monte Carlo methods for solving the Boltzmann transport equation, *Annu. Rev. Heat Transf.* 17 (2014).
- [114] B. Chatterjee, C. Dundar, T.E. Beechem, E. Heller, D. Kendig, H. Kim, N. Donmezer, S. Choi, Nanoscale electro-thermal interactions in AlGaIn/GaN high electron mobility transistors, *J. Appl. Phys.* 127 (4) (2020) 044502.
- [115] J. Hattori, T. Ikegami, K. Fukuda, Technology computer-aided design simulation of phonon heat transport in semiconductor devices, *Jpn. J. Appl. Phys.* 60 (SB) (2021) SBBA03.
- [116] B. Chatterjee, D. Shoemaker, H.-Y. Wong, S. Choi, AlGaIn/GaN HEMT device physics and electrothermal modeling, in: *Thermal Management of Gallium Nitride Electronics*, Woodhead Publishing, Massachusetts, Oxford, 2022, pp. 103–163.
- [117] S.P. Gaur, D. Navon, Two-dimensional carrier flow in a transistor structure under nonisothermal conditions, *IEEE Trans. Electron Devices* 23 (1) (1976) 50–57.
- [118] T. Chowdhury, *Study of Self-Heating Effects in GaN HEMTs*, Arizona State University, Phoenix, 2013.
- [119] N. Donmezer, S. Graham, The impact of noncontinuum thermal transport on the temperature of AlGaIn/GaN HFETs, *IEEE Trans. Electron Device Lett.* 61 (6) (2014) 2041–2048.
- [120] E. Pop, S. Sinha, K.E. Goodson, Heat generation and transport in nanometer-scale transistors, *Proc. IEEE* 94 (8) (2006) 1587–1601.
- [121] Y.-K. Cheng, C.-C. Teng, A. Dharchoudhury, E. Rosenbaum, S.-M. Kang, A chip-level electrothermal simulator for temperature profile estimation of CMOS VLSI chips, in: 1996 IEEE International Symposium on Circuits and Systems (ISCAS), IEEE, 1996, pp. 580–583.
- [122] P. Mawby, J. Zeng, K. Board, Electrothermal simulation of power VDMOS transistors, *Int. J. Numer. Methods Heat Fluid Flow* 5 (2) (1995) 185–192.
- [123] O.S. Soboleva, V.V. Zolotarev, V.S. Golovin, S.O. Slipchenko, N.A. Pikhin, The effect of the carrier drift velocity saturation in high-power semiconductor lasers at ultrahigh drive currents, *IEEE Trans. Electron Devices* 67 (11) (2020) 4977–4982.
- [124] M. Stewart, M.G. Cain, Measurement and modelling of self-heating in piezoelectric materials and devices, in: *Characterisation of Ferroelectric Bulk Materials and Thin Films*, Springer, New York, 2014, pp. 147–189.
- [125] A. Sarua, H. Ji, M. Kuball, M.J. Uren, T. Martin, K.P. Hilton, R.S. Balmer, Integrated micro-Raman/infrared thermography probe for monitoring of self-heating in AlGaIn/GaN transistor structures, *IEEE Trans. Electron Devices* 53 (10) (2006) 2438–2447.
- [126] G. Brocero, Y. Guhel, P. Eudeline, J. Sipma, C. Gaquière, B. Boudart, Measurement of self-heating temperature in AlGaIn/GaN HEMTs by using cerium oxide micro-Raman thermometers, *IEEE Trans. Electron Devices* 66 (10) (2019) 4156–4163.
- [127] A. Aiyiti, X. Bai, J. Wu, X. Xu, B. Li, Measuring the thermal conductivity and interfacial thermal resistance of suspended MoS₂ using electron beam self-heating technique, *Sci. Bull.* 63 (7) (2018) 452–458.
- [128] J. Cho, Y. Won, D. Francis, M. Asheghi, K.E. Goodson, Thermal interface resistance measurements for GaN-on-diamond composite substrates, in: 2014 IEEE Compound Semiconductor Integrated Circuit Symposium (CSICS), IEEE, 2014, pp. 1–4.
- [129] P. Jiang, X. Qian, R. Yang, Time-domain thermoreflectance (TDTR) measurements of anisotropic thermal conductivity using a variable spot size approach, *Rev. Sci. Instrum.* 88 (7) (2017) 074901.
- [130] R. Gaska, Q. Chen, J. Yang, A. Osinsky, M.A. Khan, M.S. Shur, High-temperature performance of AlGaIn/GaN HFETs on SiC substrates, *IEEE Electr. Device Lett.* 18 (10) (1997) 492–494.

- [131] J.G. Felbinger, M. Chandra, Y. Sun, L.F. Eastman, J. Wasserbauer, F. Faily, D. Babic, D. Francis, F. Ejeckam, Comparison of GaN HEMTs on diamond and SiC substrates, *IEEE Electr. Device Lett.* 28 (11) (2007) 948–950.
- [132] M.J. Tadjer, T.J. Anderson, K.D. Hobart, T.I. Feygelson, J.D. Caldwell, C.R. Eddy, F.J. Kub, J.E. Butler, B. Pate, J. Melngailis, Reduced self-heating in AlGaIn/GaN HEMTs using nanocrystalline diamond heat-spreading films, *IEEE Electr. Device Lett.* 33 (1) (2011) 23–25.
- [133] V. Volcheck, V. Stempitsky, Suppression of the self-heating effect in GaN HEMT by few-layer graphene heat spreading elements, in: *Journal of Physics: Conference Series*, IOP Publishing, 2017, p. 082015.
- [134] J.W. Pomeroy, M. Bernardoni, D. Dumka, D. Fanning, M. Kuball, Low thermal resistance GaN-on-diamond transistors characterized by three-dimensional Raman thermography mapping, *Appl. Phys. Lett.* 104 (8) (2014) 083513.
- [135] A. Sarua, H. Ji, K. Hilton, D. Wallis, M.J. Uren, T. Martin, M. Kuball, Thermal boundary resistance between GaN and substrate in AlGaIn/GaN electronic devices, *IEEE Trans. Electron Devices* 54 (12) (2007) 3152–3158.
- [136] S. Rathore, R.K. Jaisawal, P.N. Kondekar, N. Bagga, Design optimization of three-stacked nanosheet FET from self-heating effects perspective, *IEEE Trans. Device Mater. Reliab.* 22 (3) (2022) 396–402.
- [137] S. Martin-Horcajo, A. Wang, M. Romero, M. Tadjer, A. Koehler, T. Anderson, F. Calle, Impact of device geometry at different ambient temperatures on the self-heating of GaN-based HEMTs, *Semicond. Sci. Technol.* 29 (11) (2014) 115013.
- [138] C. Yoo, J. Chang, Y. Seon, H. Kim, J. Jeon, Analysis of self-heating effects in multi-nanosheet FET considering bottom isolation and package options, *IEEE Trans. Electron Devices* 69 (3) (2022) 1524–1531.
- [139] A. Akturk, N. Goldsman, Z. Dilli, M. Peckerar, Device performance and package induced self heating effects at cryogenic temperatures, in: *2006 International Conference on Simulation of Semiconductor Processes and Devices*, IEEE, 2006, pp. 240–243.
- [140] M. Xiao, B. Wang, J. Liu, R. Zhang, Z. Zhang, C. Ding, S. Lu, K. Sasaki, G.-Q. Lu, C. Buttay, Packaged Ga₂O₃ Schottky rectifiers with over 60-A surge current capability, *IEEE Trans. Power Electron.* 36 (8) (2021) 8565–8569.
- [141] R. van Erp, G. Kampitsis, L. Nela, R.S. Ardebili, E. Matioli, Embedded microchannel cooling for high power-density GaN-on-Si power integrated circuits, in: *2020 19th IEEE Intersociety Conference on Thermal and Thermomechanical Phenomena in Electronic Systems (ITherm)*, IEEE, 2020, pp. 53–59.
- [142] C. Creamer, K. Chu, P. Chao, B. Schmanski, T. Yurovchak, S. Sweetland, G. Campbell, H. Eppich, M. Ohadi, P. McCluskey, S2-T6: microchannel cooled, high power GaN-on-diamond MMIC, in: *2014 Lester Eastman Conference on High Performance Devices (LEC)*, IEEE, 2014, pp. 1–5.
- [143] Y. Mizuno, I. Soga, S. Hirose, O. Tsuboi, T. Iwai, Si microchannel cooler integrated with high power amplifiers for base station of mobile communication systems, in: *2011 IEEE 61st Electronic Components and Technology Conference (ECTC)*, IEEE, 2011, pp. 1541–1546.